Genetic Dissections of Active Zone Proteins

Inaugural-Dissertation
to obtain the academic degree
Doctor rerum naturalium (Dr. rer. nat.)
submitted to the Department of Biology, Chemistry and Pharmacy
of Freie Universität Berlin

by

Karen Suk Yin Liu

from Hong Kong

July 2012

1st Reviewer: Prof. Dr. Stephan J. Sigrist
2nd Reviewer: Prof. Dr. Hans-Joachim Pflüger

Date of Defense: 29th October, 2012

Acknowledgements

I would like to thank my instructor, Prof. Dr. Stephan Sigrist for giving me the opportunity to conduct exciting cutting-edge scientific studies in his research group, shared his expertise in scientific aspect and guided me through this PhD thesis.

I would also like to thank Prof. Dr. med. Michael Sendtner and Prof. Dr. Erich Buchner from Universität Würzburg for sharing their experience in discussions and supporting me on my project. This work was funded by DFG (http://www.dfg.de/) grant to MS (GK1156) for the first two years.

I wish to thank Prof. Dr. Dietmar Schmitz, Prof. Dr. Stefan W. Hell and Graeme W. Davis for successful collaborations on the RIM and RIM-binding protein projects. I acknowledge our RIM-binding protein team members from the Sigrist lab, Matthias Siebert, Elena Knoche, Dr. Carolin Wichmann, Karzan Muhammad, Sara Mertel, Harald Depner, Tanja Matkovic and Christoph Mettke for their productive contributions in this project. Also thanks to Stephanie Wegener (Schmitz's lab), Dr. Johanna Bücker (Hell's lab) and Dr. Martin Müller (Davis's lab) for their excellent collaborations. I would like to extend my thanks to Dr. Annemarie Hofmann for her involvement and professional support in the deletion screen of the RIM protein project.

I am grateful to Matthias Siebert and Till Andlauer for their critical comments on my dissertation. I would like to thank Karzan Muhammad, Dr. Christina Zube, Dr. Wernher Fouquet, Omid Khorramshahi, Dr. Rui Tian, Frauke Christiansen, Dr. Martin Stroedicke, Dr. Tobias Schwarz along with all further present or past members of the Sigrist lab for their inspirations, fruitful discussions and support. Likewise, I would like to thank Christine Quentin, Anastasia Stawrakakis and Madeleine Brünner for their indispensable and excellent technical assistance. I acknowledge members of the Rudolf-Virchow-Center in Würzburg; Institute for Biology/Genetics, Free University Berlin and the NeuroCure in Berlin for great discussions and a great working atmosphere.

I deeply thank all my friends in Hong Kong and Germany for their encouragement. Special thanks to my parents Patrick and Jenny, my brothers Ho-Chun and Anderson for their unconditional support and understanding. Finally, I am grateful to Detlef for his constant inspiration, support and companion in my doctoral journey.

Contents

1. Summary

Active zones are highly-specialized sites in the presynaptic bouton that are essential for neurotransmitters release. The molecular machinery mediating the fusion of synaptic vesicles (SVs) at presynaptic active zone membranes has been studied in detail, and several essential components have been identified. Active zone associated protein scaffolds were so far viewed as rather modulatory for transmission. Bruchpilot (BRP), a large coiled-coil domain protein of the mammalian CAST/ELKS family, was previously shown to be essential for both the structural and functional integrity of the presynaptic active zone cytomatrix (CAZ) at *Drosophila* synapses. To identify further components forming the active zone cytomatrix, additional candidate active zone scaffold proteins were characterized by combining genetic with physiological analysis at NMJ model synapses.

Rab3 Interacting Molecules (RIMs) are evolutionary conserved scaffolding proteins that are localized at AZs and studies in mammals have shown important synaptic roles for RIMs in SV docking and priming. To thoroughly examine the function of RIM at the *Drosophila* NMJ, we subjected the *rim* locus to genetic analysis. Several intragenic mutants of *rim* could be identified by means of deletion screenings. Surprisingly, adult vitality and locomotive behavior were only partially affected in these mutants. Next, the *Drosophila* ortholog of mammalian RIM-Binding Protein (DRBP) was subjected to genetic analysis. Intragenic null alleles were created by chemical mutagenesis. Adult vitality and locomotive behavior of larval *drbp* mutants were significantly impaired. All phenotypes of the mutants could be rescued by introducing one copy of a *drbp* genomic construct. Further characterizations of the *drbp* null allele revealed that DRBP is a direct building block of the active zone cytomatrix, and critical for efficient neurotransmitter release. The discovery of DRBP calls for the identification of additional molecular components in the BRP/DRBP matrix and the detailed analysis of how DRBP functions in active zone assembly.

Finally, immuno-stainings showed that BRP and DRBP are not equally distributed over CNS synapses. Instead, DRBP rich and poor active zone populations were easily retrieved. To assign these different classes to particular neuronal populations, subtype specific expression using GAL4 lines was combined with previously designed transgenic tools (e.g. GFP-labeled acetylcholine receptor and BRP-derived constructs). DRBP-rich synapses were found to be preferentially enriched at presynaptic terminals of mushroom body Kenyon cells. In the

antennal lobes, a much lower endogenous DRBP level was detected at olfactory receptor neuron presynapses, while DRBP-rich synapses were found at the inhibitory local interneuron active zones. This data might help in the anatomical description of synapse identities throughout the *Drosophila* circuits. Moreover, active zone protein composition diversity might be an important means of functional diversification.

Zusammenfassung

Aktive Zonen sind für die Neurotransmitterfreisetzung spezialisierte Bereiche im präsynaptischen Bouton, wo synaptische Vesikel (SV) akkumulieren und andocken. Die molekulare Maschinerie, die die Fusion synaptischer Vesikel mit der Plasmamembran der präsynaptischen aktiven Zone vermittelt, war in der Vergangenheit bereits Gegenstand detaillierter Studien, welche zur Identifikation mehrerer essentieller Komponenten geführt haben. Bisher galten Gerüstproteine der aktiven Zone vor allem als Modulatoren der Signalübertragung. Es wurde bereits gezeigt, dass Bruchpilot (BRP), ein Protein mit ausgedehnten coiled-coil Regionen und Homologie zur CAST/ELKS Familie, essentiell für sowohl die strukturelle wie die funktionelle Integrität der Cytomatrix der präsynaptischen aktiven Zone (CAZ) in *Drosophila* Synapsen ist. In dieser Studie wurden in NMJ Modellsynapsen weitere Gerüstproteine mit genetischen und physiologischen Methoden identifiziert und charakterisiert.

Rab3 Interacting Molecules (RIM) sind evolutionär konservierte Gerüstproteine, für die in Säugern eine wichtige Rolle bei Neurotransmitterfreisetzung nachgewiesen wurde. Zunächst wurde die Rolle von RIM in NMJ Modellsynapsen durch genetische Analyse des *rim* Lokus untersucht. *Deletionsscreening* führte zur Identifikation mehrerer *rim*-Mutanten, doch Vitalität und lokomotives Verhalten adulter Fliegen waren überraschenderweise nur partiell beeinträchtigt. Weiterhin wurde das *Drosophila*-Orthologe des *RIM-Binding Protein* (DRBP) einer genetischen Analyse unterzogen und es wurden durch chemische Mutagenese intragenische Nullallele erzeugt. *drbp* mutante Larven wiesen ein erheblich gestörtes lokomotives Verhalten auf, und auch die Vitalität adulter Fliegen war stark beeinträchtigt. Die Einführung eines genomischen Rettungskonstrukts stellte die normale Transmission und Vitalität wieder her. Durch weitere Charakterisierung des *drbp* Nullallels konnte gezeigt werden, dass es sich bei DRBP um einen integralen Baustein der Zytomatrix der aktiven Zone

handelt, der bei der Freisetzung von Neurotransmittern eine kritische Rolle spielt. Die Entdeckung dieses essentiellen Faktors unterstreicht, dass es für das Verständnis der präsynaptischen aktiven Zone entscheidend sein wird, in Zukunft ein vollständigeres Bild jener Komponenten zu gewinnen, welche mit der BRP/DRBP-Matrix interagieren.

Mittels Immunfärbung konnte schließlich gezeigt werden, dass BRP und DRBP nicht gleichmäßig über ZNS-Synapsen verteilt sind. Stattdessen konnten DRBP-reiche und -arme Synapsenpopulationen identifiziert werden. Um diese verschiedenen Synapsen bestimmten Neuronen-Subtypen zuzuordnen, wurden subtypenspezifische GAL4 Treiberlinien mit bereits zuvor erstellten transgenen Werkzeugen (z.B. GFP-markierte Acetylcholin-Rezeptoren und fluoreszent-markierte BRP Konstrukte) kombiniert. Synapsen mit hohem DRBP Level waren hauptsächlich in den Präsynapsen von Kenyon Zellen im Pilzkörper zu finden. In den Antennalloben wurde ein niedriger endogener DRBP-Level in Präsynapsen olfaktorischer Rezeptorneuronen gefunden, während DRBP-reiche Synapsen in den lokalen inhibitorischen Interneuronen vorhanden waren. Diese Daten erlauben nicht nur eine bessere anatomische Zuschreibung von Synapsen-Identitäten in den neuronalen Netzwerken von *Drosophila*, es besteht auch die Möglichkeit, dass die Diversität in der Zusammensetzung der aktiven Zone mit einer funktionalen Diversifizierung korrespondiert.

2. Introduction

2.1 Synapses

Synapses are specialized cell-cell contacts where signals are transduced from the axonal terminus of a neuron to a target cell in a regulated manner. The pre-synaptic terminal and the post-synaptic target site are the two distinctive elements forming this contact zone, separated by a synaptic cleft (Bennett, 1999). Synaptic transmission is achieved by either electrical or chemical communication, the latter using so-called neurotransmitters. Action potentials in the pre-synaptic neuron trigger current flow into the post-synaptic cell at electrical synapses. Chemical synapses upon the arrival of an action potential release of neurotransmitters from the pre-synaptic site, which interact with receptors on the post-synaptic cell to finally propagate the stimulus.

2.1.1 Relevance of synapses in neuronal communication

Synaptic transmission is predominantly chemical in the vertebrate brain and at neuromuscular junctions. Electrical and chemical synapses differ in both morphological organization and molecular mechanisms of signal transduction (see Fig. 2.1). Electrical synapses are specified by an area of very close apposition, ranging from 2–4 nm between the pre- and post-synaptic membranes. Electrical coupling of neurons is mediated via tight gap junctions, ensuring extremely fast signal transduction but less possibility for modulation. In contrast, there is no continuity between the cytoplasm of the two cells at chemical synapses. Once an action potential propagating along the presynaptic axon reaches the chemical synapse, opening of voltage gated Ca^{2+}-channels induces Ca^{2+} influx to the presynaptic terminal. The elevated Ca^{2+} concentration triggers synaptic vesicles (SVs) fusion with the presynaptic membrane and the release of neurotransmitter molecules from the vesicles into the synaptic cleft. Chemical synapses depend on the proper interplay of several modules for functionality: active zones (AZ) at the presynaptic site, SVs and their exo/endo-cycle machinery, transsynaptic pairs of cell adhesion molecules and the postsynaptic density (PSD). Morphological features of chemical synapses in various species are conserved, regardless of their size, location or types of neurons and their targets. SV release takes place in a spatially defined manner from specialized release sites at the plasma membrane called AZ. The intracellular side of AZs is associated with electron-dense multi-protein scaffolds, comprising sets of large multi-domain proteins, which apparently play both structural and functional roles. Neurotransmitter receptors accumulate within another electron dense compartment, the PSD at the postsynaptic

site, where the stability and dynamic regulation of neurotransmitter receptor populations takes place (Renner et al., 2008).

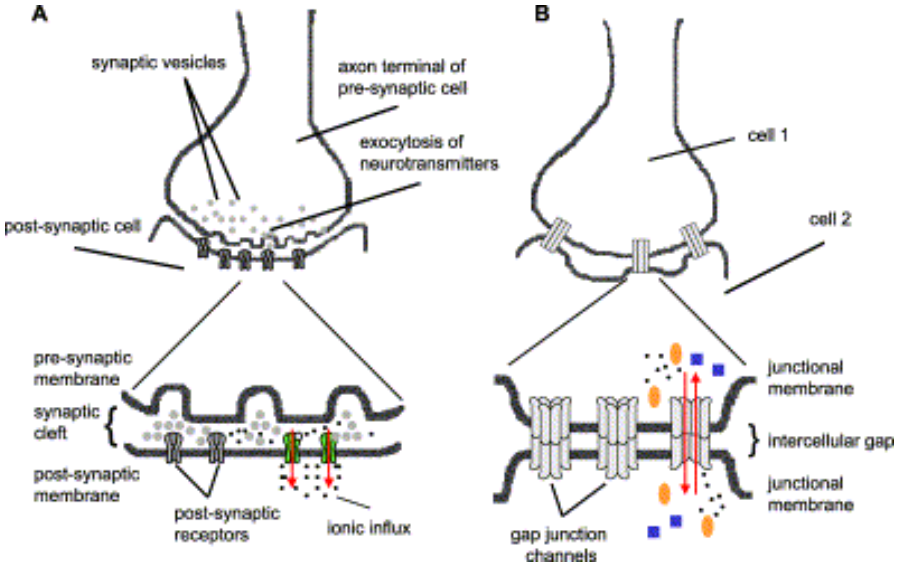

Fig. 2.1 Chemical and electrical synaptic transmission.

(A) Principal features of chemical synapses. An action potential arrived at the pre-synaptic terminal triggers the exocytosis of vesicles filled with neurotransmitters (gray). Vesicles are then released into the synaptic cleft; neurotransmitters diffuse and bind to specific receptors on the post-synaptic membrane. Transmitters binding alter the conformation of the receptor and enable subsequent ion influx into the postsynaptic cell. (B) Gap junction channels at electrical synapses allow a direct communication between the cytoplasm of the two coupled cells. Ions (black circle), metabolites (blue) and small second messenger molecules (orange) diffuse through gap junction channels. Chemical transmission is unidirectional, whereas electrical synapses transmit signals in both directions equally (taken from Hormuzdi et al., 2004).

The nature of synaptic transmission (excitatory and inhibitory) in chemical synapses is also critical in signal transduction and biological computation. Neurotransmitters glutamate and acetylcholine (ACh) mediate excitatory transmission, whereas gamma-aminobutyric acid (GABA) or glycine is responsible for inhibitory transmission. The nature of synaptic transmission is one of the relevant factors for synaptic modulation.

2.1.2 Molecular characterization of the presynaptic compartment in glutamatergic synapses

Biogenesis and transport, trapping and stabilization, as well as maturation and growth of synaptic components are three continuous and interrelated cellular processes in presynaptic differentiation; they begin after axon formation and culminate with the assembly of synapses (Jin and Garner, 2008). The presynaptic terminal can be found either along the axon shaft or at the termini of the axon and comprises an aggregation of several specialized proteins (Jin and Garner, 2008). Each presynaptic protein performs a unique role in certain processes of chemical transmission such as initiating the synapse assembly, SV priming/docking/release, or endocytosis and SV recycling. This presynaptic specialization contains sites called AZs,

where SVs cluster, presynaptic protein scaffolds assemble, rapid SVs fusion and neurotransmitter release takes place after Ca^{2+} influx. The perisynaptic zone, where fused SVs are retrieved by clathrin-mediated endocytosis (Gundelfinger et al., 2003), surrounds the AZ. Importantly, membranes of AZ are covered by an electron dense cytomatrix, referred to as cytomatrix at the active zone (CAZ) (see Fig. 1 in Zhai and Bellen 2004) describes an organized network of microfilaments and an associated proteinacious cytomatrix. The CAZs likely participates in achieving and controlling efficient SVs release, which consists of translocation of SVs to the AZ, docking and priming, membrane fusion as well as vesicle endocytosis.

Protein scaffolds at AZs provide interaction platforms to organize protein-protein interactions spatiotemporally or enzymatic activities that are pivotal to assure tight regulation of the SV exo-/endocytic cycle. Several AZ scaffold components have been identified in mammals and they engage in complex interaction schemes (Fig. 2.2). AZs are now known to be composed of an evolutionarily conserved complex containing as primary constituents Rab3-interacting molecules (RIMs), mammalian homologue of *C. elegans* Unc13 protein (Munc13), RIM-binding protein (RIM-BP), Liprin-α and ELKS proteins (Südhof and Rizo, 2011). RIMs and Munc13 are the well-characterized CAZ components involved in SV fusion regulation.

Another class of proteins includes Bassoon, Piccolo, CAZ-associated structural protein (ELKS/CAST), which are all mainly structural components of the presynaptic specialization and its associated cytoskeleton (reviewed in Schoch and Gundelfinger, 2006; Jin and Garner, 2008). Piccolo and Bassoon are giant proteins (530 and 420 kDa) and contain large amounts of putative interaction domains (PDZ, zinc fingers, coiled-coil, proline-rich, C2 and SH3 domains). This indicates a possible scaffolding function as many interactions with other synaptic proteins could be supported (Garner et al., 2000). Similar scaffolding functions have been implicated for CAST/ERC and RIM1 (Wang et al., 2002; Ziv and Garner, 2004; Schoch and Gundelfinger, 2006). CAST family proteins are enriched in AZs and interacts with other prominent CAZ proteins, including Bassoon (tom Dieck et al., 1998; Khimich et al., 2005), Piccolo (Fenster et al., 2000), Munc 13-1, an essential factor for the priming of SVs (Augustin et al., 1999; Ohtsuka et al., 2002) and RIM1, which bridges between SVs and the AZ (Ohtsuka et al., 2002). Fundamental aspects of the AZ organization are still largely unknown: which proteins are essential for scaffold formation and stabilization or which factors bind transiently to the scaffold as well as the degree of contribution to its formation or stability. Hence, understanding the molecular architectures of AZ scaffolds is of particular interest.

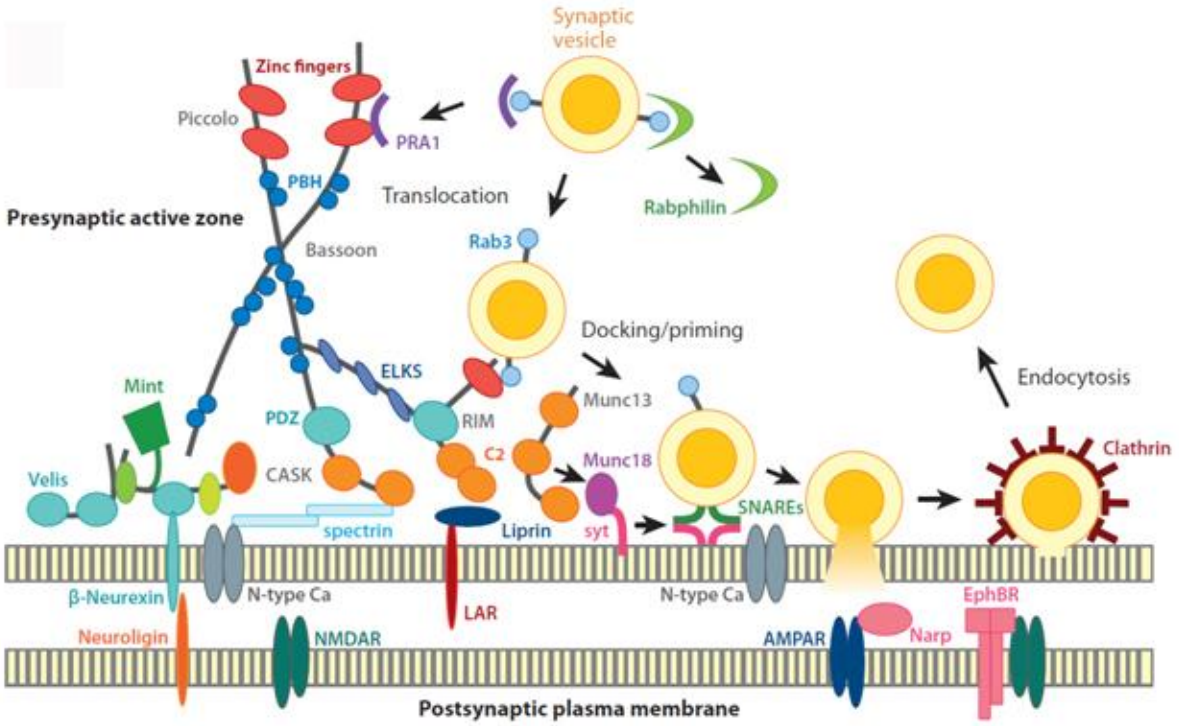

Fig. 2.2 Molecular components of the presynaptic cytomatrix at the vertebrate active zone (CAZ).

Schematic diagram of presynaptic AZ proteins at vertebrate synapses. The cycle begins with the SVs translocation from the reserve pool to the readily releasable pool located at the plasma membrane. Docking of SV proteins via interaction with proteins such as Rab3a and RIM. SVs are primed by RIM, Munc13, and Munc18 to enter into the SNARE fusion complex that ready for calcium-triggered SV fusion. SV proteins are captured and recycled by the clathrin endocytic machinery after fusion. Other examples of structural molecules that define the AZ are highlighted: Piccolo, Bassoon, RIM, CASK, Velis, Mints, ELKS, and Liprins. They are suitable for the putative scaffolding functions since they are composed of modular domain structures (taken from Jin and Garner, 2008).

2.1.2.1 Structural and molecular organization of the AZ

The CAZ appears electron dense in electron micrographs, in contrast to the cytoplasm, the presynaptic membrane and SVs. Shape and size of these electron dense bodies vary between different synapse types, ranging from 50 nm high pyramidally shaped structures in mammalian central nervous system (CNS) synapses (Phillips et al., 2001) to about 0.5-1 µm ribbon-like or spherical shape at mammalian sensory ribbon synapses (von Gersdorff, 2001). Studies on Ribeye, Piccolo, Munc13, ELKS and Bassoon at rodent photoreceptor ribbon synapses provided us with an idea about the spatial organization of AZ scaffolds (tom Dieck et al., 2005) using immuno-electron microscopic (EM) labeling. The large structural protein Bassoon in vertebrates is associated with ribbon synapses and it is proposed to be essential for ribbon anchorage since floating ribbons are detected in Bassoon mutants (reviewed in Wichmann and Sigrist, 2010). At the *Drosophila* larval neuromuscular junction (NMJ), T-shaped protrusions (T bars, 70 nm) (Atwood et al., 1993) resemble a distinct morphology (comprising a platform sitting on a pedestal) in AZ scaffolds (Fig. 2.3). Filamentous AZ-

resident electron dense filaments (T bars, Fig. 2.3) are often observed to be in direct contact with SVs. They probably provide a platform for SV tethering and molecular interactions of CAZ proteins (Atwood et al., 1993; Kittel et al., 2006; Fouquet et al., 2009; Hallermann et al., 2010). These large varieties of structural differences of CAZs are reflecting the physiological demands regarding the synaptic contact in various species (Zhai and Bellen, 2004; Siksou et al., 2007).

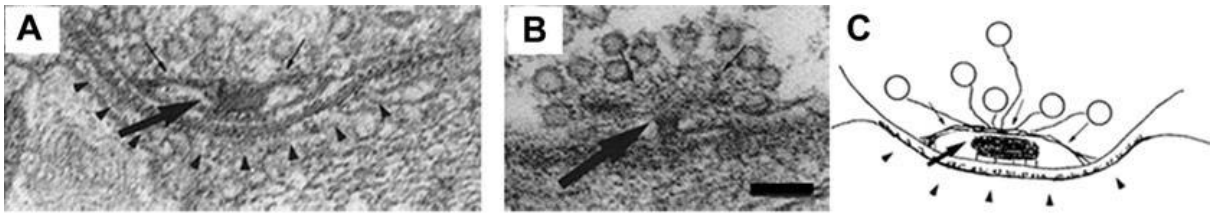

Fig. 2.3 T bar appearance at the *Drosophila* NMJ.

High-pressure freezing and freeze-substitution of the *Drosophila* NMJ T bars structure under transmission electron microscopy. Conventionally embedded (A) cross-sectioned T bar (B) T bar sectioned tangentially are shown. Population of vesicles (small arrows) tethered to the filamentous platform residing on T bar pedestal (arrows) and arrowheads indicate specialized postsynaptic membrane. Scale bar in B, 100 nm. (C) Diagrammatic representation of cross section of T bar (taken from Wichmann and Sigrist, 2010).

2.1.2.2 ELKS/CAST/ERC/BRP proteins

ERC (ELKS/Rab6-interacting protein/CAST) in vertebrates was first isolated as an interacting partner of the RIM PDZ domain (Wang et al., 2002). CAST-family members localize to AZs of various synapses and interact with other AZ proteins such as RIM and Liprin-α (Ohtsuka et al., 2002; Wang et al., 2002; Ko et al., 2003; Deguchi-Tawarada et al., 2004). Bruchpilot (BRP) in *Drosophila*, a member of the mammalian ELKS/CAST-family, is the master organizer of the presynaptic AZ scaffold (Kittel et al., 2006). Before, there was no information to which proteins would contribute to the T bar formation in *Drosophila* since there were no homologues of Bassoons or Piccolo. BRP shapes the AZ scaffold by adopting an elongated conformation as revealed by EM analysis. Stimulated emission depletion microscopy (STED) (Hell, 2007) revealed donut-shaped structures recognized by Brp^{Nc82}, supporting the idea that BRP is the structural component of the T bar that centred at the AZ (Kittel et al., 2006). In *brp* null mutants this distinct feature of AZ scaffolds is completely lost and no electron dense material is left (Kittel et al., 2006). BRP is also suggested to perform subsets of functions including recruitment and physical tethering of SVs to the AZ scaffold (Hallermann et al., 2010) and Ca^{2+}-channel clustering (Kittel et al., 2006; Fouquet et al., 2009). Severely reduced amplitudes of excitatory junctional currents, delayed nerve-evoked responses, a decreased initial release probability of SVs (Kittel et al., 2006), together with a

drastic decrease in Ca^{2+}-channels at the NMJ are characteristics of the *brp* mutant. BRP is therefore central to the AZ in establishing the proper organization of the cytomatrix architecture structurally (T bar assembly) and molecularly (SVs tethering, Ca^{2+}-channels clustering for proper SVs release).

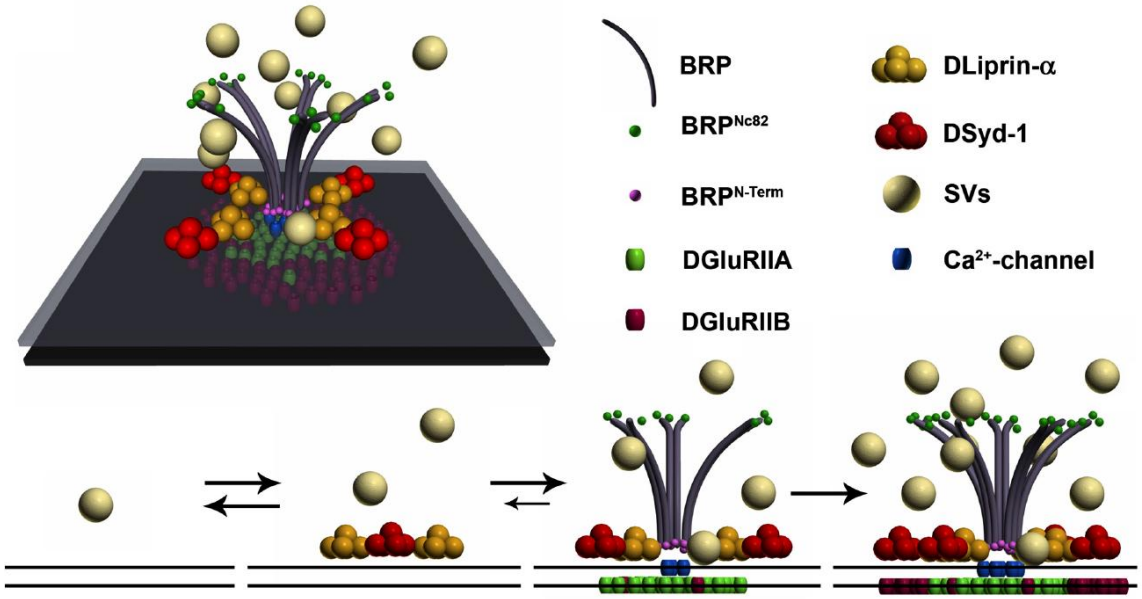

Fig. 2.4 Spatiotemporal model of AZ assembly and organization at *Drosophila* NMJs.
(taken from Fouquet et al., 2009)

The N-terminus of BRP is found to interact directly with the C-terminus of Ca^{2+}-channels and is closer to the AZ membrane (membrane-proximal) than the C-terminus (see model in Fig. 2.4). It covers an area very similar to the area covered by Ca^{2+}-channels (Fouquet et al., 2009). BRP resembles the functionality of mammalian ELKS in Ca^{2+}-channel clustering by possessing a homology in its N-terminus, whereas no direct homology is present for its large coiled-coil-rich structure along the protein (Kittel et al, 2006; Wagh et al., 2006). This coiled-coil stretches are predicted to dominate the entire structure, except the N-terminus, thus one speculation is that BRP plays a key role in maintaining a high density of Ca^{2+}-channels at the AZ membrane. Hence, understanding the possible interaction of the N-terminal BRP domain and Ca^{2+}-channel α1 subunit may help us to unravel BRP's role in the AZ scaffold in deeper detail. The Ca^{2+}-channel α1 subunit Cacophony (Cac) in *Drosophila* clusters within AZ membranes and dominates the SV release at NMJ synapses (Kawasaki et al., 2000; Kawasaki et al., 2004). In *brp* mutants Cac is largely de-clustered and a reduced neurotransmitter release is observed, whereas SVs remained docked at the AZ membrane.

A hypomorphic allele *brp*^{nude} lacking 17 aa of the C-terminal of BRP was identified in a chemical mutagenesis (ethane methyl sulfonate, EMS) screen (Hallermann et al., 2010). The AZ scaffolds (T bars) were properly shaped in *brp*^{nude} mutants but SVs that are normally associated with it were completely absent. Neurotransmitter release was depressed upon higher frequency stimulation while basal transmission was unaltered. This suggests that the C-terminal (membrane-distal) end of BRP mediates an essential function for SV binding, possibly by directly interacting with one or several SV proteins or the direct tethering of SVs to the AZ scaffold by BRP to sustain SV release. Coiled-coil stretches of BRP might participate in pre-organizing SNAP/SNARE (soluble N-ethylmaleimidesensitive factor attachment protein /SNAP receptor proteins) at SVs, serving as an interaction platform for other AZ scaffold components essential for AZ assembly as well as for the functional maturation of *Drosophila* AZs.

The AZ proteins Liprin-α and DSyd-1 are tightly associated with BRP and localize to discrete clusters around the edge of the AZ scaffold (Fouquet et al., 2009; Owald et al., 2010). Disruption of AZ scaffold morphology without affecting the scaffold stability is observed in mutants of both these components (Fouquet et al., 2009; Owald et al., 2010). Since relatively few AZ components are known, uncovering other AZ proteins taking part in forming the cytomatrix architecture will be of high relevance.

2.1.3 Mechanisms of synaptic vesicle (SV) exo- and endocytosis

2.1.3.1 SVs and SV pools at the AZ

During larval development neuromuscular boutons become increasingly filled with vesicles (Kuromi and Kidokoro, 1998) that are clear and round in shape. As mentioned above already, SVs often appear physically attached to the presynaptic component T bar ribbons at the *Drosophila* NMJ. The vesicles contain subpopulations of pleiomorphic and dense-core vesicles and vesicle exocytosis occurs at the presynaptic plasma membrane surrounding the entire T bar. Immuno-electron-microscopy of hippocampal cultures showed multi-vesicular aggregates, putative precursors of AZ assembly, densely accumulated in the mammalian AZ (see Fig. 2 in Owald and Sigrist, 2009). There are three distinct SVs pools (Zucker and Regehr, 2002; Schneggenburger and Neher, 2005; Rizzoli and Betz, 2005): the readily releasable pool (RRP) where the vesicles are docked and primed to the AZ membrane for prompt release; the recycling pool where the vesicles maintain transmitter release during moderate physiological stimulation; and the reserve pool where the vesicles act as a storage

depot that participates in release only upon strong stimulation or when the recycling pool has been used up (see model in Fig. 2.5B). The number of release-ready SVs and the probability of exocytosis of the individual vesicle determine the number of SVs released at a synapse. High release probability synapses tend to exhibit paired-pulse and frequency-dependent depression, whereas low release probability of vesicles results in facilitation and augmentation (Zucker and Regehr, 2002). SVs must be both release competent and have a very close proximity to presynaptic Ca^{2+}-channels in order to release neurotransmitter synchronously in response to a presynaptic action potential. The recruitment of SVs to sites where Ca^{2+}-channels cluster is more decisive than fusion competence for rapid neurotransmitter release in response to presynaptic action potentials (Wadel et al., 2007).

2.1.3.2 The SV cycle

SVs undergo a cycle of exocytosis at the AZ and endocytosis at the adjacent periactive zone enabling their rapid reuse. Clathrin-mediated recovery of SVs takes place parasynaptically (adjacent to the synapse) with some vesicles travelling through the endosomal compartment at NMJs (Wucherpfennig et al., 2003). Immediate vesicle retrieval from kiss-and-run release has been suggested to take place below the T bar in motor neuronal terminals (Koenig and Ikeda, 1996; Verstreken et al., 2002). Two parallel pathways of SV endocytosis are also being suggested: fast recycling via local refilling of neurotransmitters without undocking ("kiss-and-stay") and slow, full recycling of vesicles with passage through an endosomal intermediate (reviewed in Südhof and Rizo, 2011, Fig. 2.5A). Numerous proteins and factors are essential in regulating the SV endocytosis and recycling processes, e.g. Endophilin and Intersectin (Verstreken et al., 2002; Koh et al., 2004).

The divalent cation calcium (Ca^{2+}) is essential for transmission of nerve impulses and elevations of the Ca^{2+} concentration in the presynaptic terminal trigger the release of neurotransmitter from SVs. SV release requires a molecular coupling of Ca^{2+} influx with vesicle fusion at the protein level (Rosenmund, 2003). Similar to the observations in vertebrate ribbons (Zhen and Jin, 2004), synaptic release depends on local induction of high Ca^{2+} microdomains and T bars are clustered with Ca^{2+}-channels (Prokop, 1999; Kawasaki et al., 2004). Ca^{2+} binding to the vesicle protein Synaptotagmin initiates vesicle fusion with the AZ membrane (Geppert, 1994; Koh and Bellen, 2003), which is mediated by the SNARE complex. The SNARE complex consists of the SV protein Synaptobrevin and the plasma membrane proteins SNAP-25 and Syntaxin (Jahn, 2004; Südhof, 2004). Propagating action

potentials lead to the formation of Ca^{2+}-microdomains at AZ membranes from localized clusters of voltage-operated Ca^{2+}-channels that strategically trigger SV exocytosis. Close proximity between SVs and Ca^{2+}-channels at AZ membranes established by AZ scaffolds (Neher and Sakaba, 2008) is critical for efficient SV release.

Dynamic changes in the presynaptic AZ organization result in the alternation of the density, coupling, juxtaposition of Ca^{2+}-channels and SVs (Atwood and Karunanithi, 2002). Variable distances between Ca^{2+}-channels and vesicles resulting in heterogeneous fusion kinetics upon Ca^{2+} influx were also observed (Neher, 1998). Hence, the distance between the Ca^{2+}-channel and the SV is important for the release properties of a synapse.

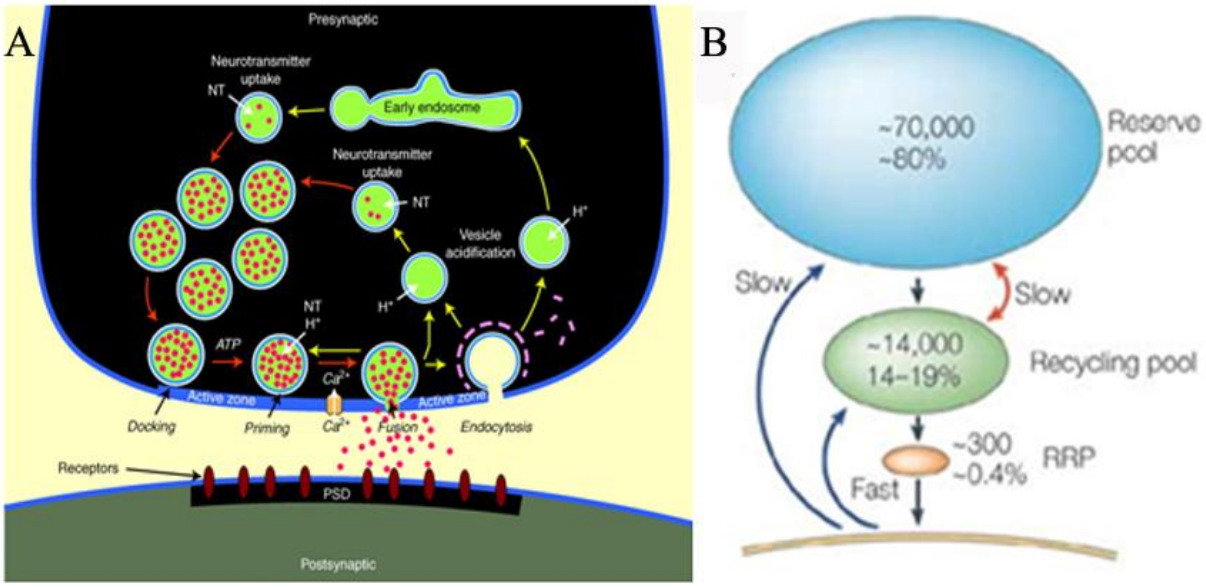

Fig. 2.5 The SV Cycle and features of SV pools.

(A) The SV cycle is highly regulated and comprises of two key steps: exocytosis (red arrows) followed by endocytosis and recycling (yellow arrows). SVs (green circles) are filled with neurotransmitters (NT; red dots) are docked at the AZ and later ATP-dependent priming of SVs, making them competent to respond to a Ca^{2+}-signal. SV fusion reaction is completed by elevated intracellular Ca^{2+} level locally at the AZ after depolarization of the presynaptic membrane. Exocytosis takes place and subsequent binding of released neurotransmitters to receptors associated with the PSD. SVs undergo Clathrin-mediated endocytosis and recycling via several pathways; the SV cycle restart again upon next arrival of the action potential. (B) The readily releasable pool (RRP) is depleted and release upon Ca^{2+} influx; the balance can be maintained almost indefinitely by repeated recycling of the recycling pool at this frequency. Blue arrows indicate endocytosis and red arrows indicate mixing between pools (taken from Südhof and Rizo, 2011; Rizzoli and Betz, 2005).

2.1.4 Molecular characterization of the postsynaptic compartment in glutamatergic synapses

Many Excitatory synapses in the vertebrate CNS as well as the synapses at the *Drosophila* NMJ use glutamate as transmitter ("glutamatergic"). Upon SV release, binding of the neurotransmitter glutamate to glutamate-sensitive receptors on the postsynaptic membrane

takes place, followed by subsequent opening of receptor-coupled ion channels to permit cation influx and postsynaptic depolarization (Kim and Sheng, 2004). Glutamate receptors are categorized into two major groups: metabotropic and ionotropic. The tetrameric ionotropic glutamate receptor complexes can be further subdivided into AMPA (alpha-amino-3-hydroxy-5-methyl-4-isoxazole-propionic-acid), NMDA (N-methyl–D-aspartate) and kainate receptors. The ionotropic glutamate receptor subunits expressed at the *Drosophila* NMJ are similar to mammalian non-NMDA-type glutamate receptors (Petersen et al., 1997). NMDARs are distributed throughout the entire postsynaptic density (PSD) membrane, whereas AMPARs appear to localize to small subsynaptic domains within the PSD (Masugi-Tokita et al., 2007). Hence, ionotropic receptors with differing conductivity or ion specificity define the precise characteristics of a synapse. In addition, metabotropic transmembrane receptors activate G-proteins upon ligand-binding, which can then either directly regulate ionotropic receptors or trigger second messenger pathways (Woehler and Ponimaskin, 2009).

A specialized postsynaptic subcellular organization, the PSD, serves essential roles to guide the glutamatergic transmission. The PSD at excitatory synapses is thicker and more complex than that at inhibitory synapses; it clusters and anchors postsynaptic receptors and ion channels and comprises a specialized sub-membraneous cytoskeleton. Postsynaptic scaffolds and adhesion proteins, kinases, phosphatases as well as cytoskeletal elements are recruited to the PSD (Sheng and Hoogenraad, 2007), serving as an important mechanism for synaptic plasticity. Receptors for neurotransmitters in neuronal synapses are transiently stabilized at the postsynaptic membrane by interactions with a highly dynamic meshwork of postsynaptic scaffolding proteins. This dynamic suggests a view of the synapse as a steady-state structure with different local equilibrium states; modifying the exchange rates rapidly shifts this equilibrium. In addition, most neurotransmitter receptors cycle between the membrane and the intracellular stores, such that the extrasynaptic membrane acts as a reserve pool for synaptic receptors. This dynamic exchange of receptors between synaptic and extrasynaptic membranes is dependent on the interaction with synaptic scaffold proteins in the PSD. Numerous proteins are responsible for the proper PSD organization, of which a small selection is highlighted in Fig. 2.6 (Kim and Sheng, 2004; Renner et al., 2008). Scaffolding proteins harboring one or more PDZ domain are a common characteristic within the PSD, e.g. the membrane-associated PSD95 (postsynaptic density protein 95) and SAP47 (synapse associated protein 47); guanylate kinases (MAGUKs), GRIP (glutamate receptor interacting

protein), ABP (AMPA receptor binding protein) and PICK1 (protein interacting with C kinase) (McGee and Bredt, 2003; Kim and Sheng, 2004).

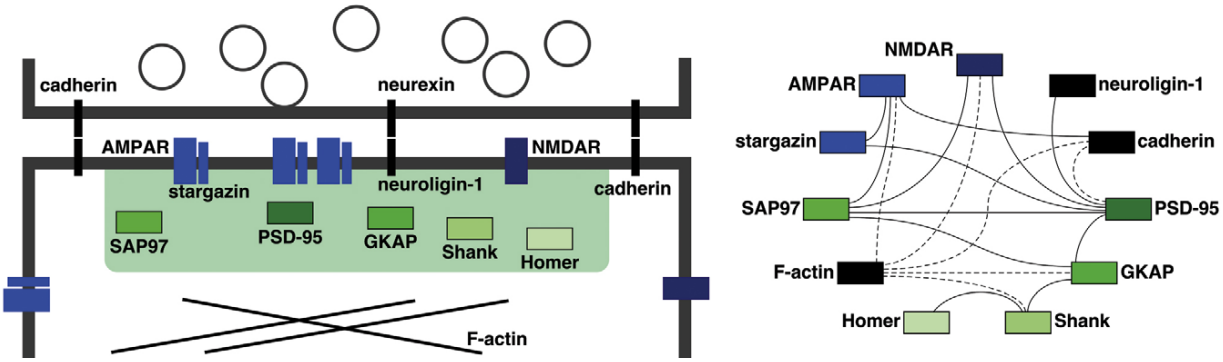

Fig. 2.6 The postsynaptic scaffold at excitatory synapses.

The model (left) shows a limited number of synaptic scaffold or adaptor proteins (green shades) characterize the highly complex postsynaptic scaffold at excitatory synapses. Postsynaptic membrane provides sites for binding of excitatory receptor types (AMPARs and NMDARs, blue), cytoskeletal, adhesion and adaptor proteins. PSD (green area) at excitatory synapses displays a subsynaptic organization, where possible interactions of synaptic components take place. (Right) Direct and indirect interactions are represented in solid and dashed lines, respectively (taken from Renner et al., 2008).

At the *Drosophila* NMJ, levels of postsynaptic glutamate receptors regulate the number of synapses formed (Sigrist et al., 2000; 2003) and they are modulated by diverse subsynaptic compartments: adaptor proteins, kinases and scaffolding molecules (DiAntonio, 2006). Thereby, the formation and growth of individual synapses at the NMJ is directly correlated with the entry of glutamate receptors from diffuse extrasynaptic pools and glutamate receptors stably integrate into immature PSDs (Rasse et al., 2005). Glutamate receptors that are recruited and incorporated into the postsynaptic membrane are critical for enlarging PSDs by organizing cell adhesion to bring presynaptic and postsynaptic membranes in apposition during synapse formation (Schmid et al., 2006).

2.2 The *Drosophila* NMJ as a model for genetic analysis of glutamatergic synapses

The *Drosophila* larval neuromuscular junction (NMJ) model is a well-characterized, highly traceable and widely used model system in developmental and neurobiological studies. It has been used as a model for various aspects of synapse development, plasticity and physiology, including synaptogenesis and its underlying molecular mechanisms (Ruiz-Cañada and Budnik, 2006). Larval NMJs are easily accessible, located at large and easily identifiable muscles with well-defined synapses (Ruiz-Cañada and Budnik, 2006).

2.2.1 Structural organization of the *Drosophila* larval NMJ

Motoneurons originate from the ventral ganglion of the CNS and extend axons in segmentally repeated bilateral nerves and transverse nerves. Larval body wall muscles of each abdominal segment are innervated by thirty motoneurons per hemisegment. Each abdominal hemisegment contains thirty skeletal, contractile muscle fibers (sixty muscles per segment), identifiable by their insertion sites and positions. Single motor neurons can specifically innervate a single muscle or distribute their terminals over several different muscles, branching their release sites onto different targets in tightly genetically regulated manners (Keshishian and Chiba, 1993; Keshishian et al., 1993; Keshishian et al., 1996). The whole muscle structure is innervated by distinct and specific branches of the motoneuron axons. A particular muscle could be innervated exclusively by a single or by multiple motor neurons. This is tightly regulated by genetic programs during development. Most muscle fibers are innervated by at least two motoneurons, whereas muscle 4 is one of the muscles that is innervated by one motoneuron. Precise quantities of synapses and the types of pre- and postsynaptic structures are assigned by both muscles and neurons to their various contacts, determining the extent to which each individual neuromuscular contact contributes to the activation of any particular muscle (Keshishian et al., 1996; Prokop and Meinertzhagen, 2006).

Three different types of NMJs, type-I (big type-Ib and small type-Is), type-II, and type-III exist in larvae (Jan and Jan, 1976). Type-Ib and Is synapses release primarily excitatory transmitter glutamate. The most abundant class of type-Is and Ib motoneurons innervate muscles 6 and 7. Each larval segment consists of a characteristic and repeated muscle pattern which provides an easy orientation within the larval body. Selected regions of motoneuron terminals in abdominal segments A2 to A4 are easily recognizable and can be identified reliably within a single larva or between individuals (Keshishian et al., 1996). Each NMJ exhibits distinctive substructures which are termed boutons; single boutons are made up of 5-20 single smaller spot like sites (=synapses) consisting of both pre- and postsynaptic proteins (Aberle et al., 2002; Gorczyca and Budnik, 2006) (Fig. 2.7). AZs of single synapses are easily identifiable using fluorescent labeling of synaptic proteins (e.g. presynaptic *Bruchpilot* and postsynaptic glutamate receptors GluRII, see Fig. 3 in Qin et al., 2005). Features of synaptic ultrastructure of the *Drosophila* NMJ include close apposition of the pre- and postsynaptic membranes over several hundred nanometers (synaptic cleft: 10-20 nm) and distinct electron dense specializations (T bars) associated with presynaptic AZs (Zhai and Bellen, 2004).

Glutamatergic synapses at the *Drosophila* synapses are remarkably similar to those of excitatory vertebrate CNS synapses in terms of ultrastructure, molecular composition of the presynaptic release machinery and the postsynaptic PSD organization (Fernandez-Chacon and Südhof, 1999). Synaptotagmin, Syntaxin, Synaptobrevin and Wnt/Wingless are a few of the examples that are homologous to previously identified vertebrate presynaptic proteins (Broadie and Bate 1993; Salinas, 2005). The adhesion protein Fasciclin II (FasII), which is involved in synaptic growth and stabilization (Schuster et al., 1996; Sone et al., 2000), surrounds individual synapses. In the PSD, which is juxtaposed to the AZ, glutamate receptors (DGluRs) are clustered, as well as voltage-gated ion channels, scaffolding and regulatory molecules as PAK (p21-activated kinase) (Albin and Davis, 2004; Qin et al., 2005; Prokop and Meinertzhagen, 2006). The muscle membrane is highly convoluted beneath the PSD to form the subsynaptic reticulum (SSR) and diverse scaffolding and adhesion proteins, which might be involved in the structural organization and signaling mechanisms, like Dlg (Discs large), are present at the SSR membrane (Thomas et al., 1997).

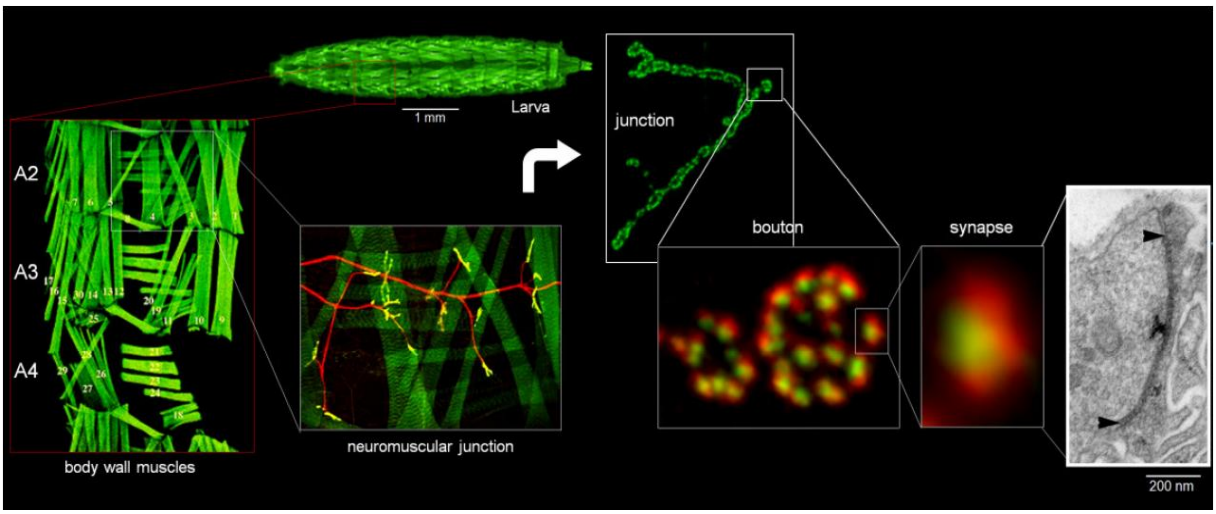

Fig. 2.7 Schematic overview of the *Drosophila* larval NMJ.

Representation of the *Drosophila* NMJ from larva to the synapse and the main structural features of this model system are depicted (taken from doctoral thesis of Wernher Fouquet, Fig. 11).

The main goal of our group is to understand and define the molecular architecture of the AZ scaffold by anatomical, genetic and functional analysis of BRP and related presynaptic proteins. Each of these techniques allows its own special view on the presynaptic AZ organization. Apart from using the larval NMJ as the model system, our group is also interested in studying AZ architecture and understanding specific roles of AZ proteins in adult CNS synapses. In the following section (Introduction section 2.3), we provide information

about neural circuitry of the adult brain and our approach to understand CAZ composition in the adult CNS synapses.

2.3 *Drosophila* as a model for structural and functional studies of olfactory information processing

Drosophila is a very well suited model system for the structural and functional study of olfactory circuitry. Rapid growing variety of genetic tools enables the visualization, perturbation and functional manipulation of specific neuron types (reviewed in Oslen and Wilson, 2008b). The recent advances in electrophysiological (recording neural activity) and in optical imaging techniques enable us to understand how olfactory information in *Drosophila* is processed and transformed. Additionally, the manageable size of the fly brain (containing approximately 100,000 neurons) makes *Drosophila* a powerful system for understanding sensory processing and perception and analyzing the neural circuit basis of memory and behavior (reviewed in Masse et al., 2009).

2.3.1 The antennal lobe is the primary olfactory center

The insect antennal lobe (AL) is the primary olfactory center, analogous to the olfactory bulb of vertebrates (reviewed in Vosshall and Stocker, 2007). The basic building unit of the AL is called a glomerulus, which comprises a complex network of several types of neurons: olfactory receptor neurons (ORNs), local interneurons (LNs) and projection neurons (PNs) (Stocker et al, 1990; Stocker, 1994; Strausfeld and Hildebrand, 1999). Each neuronal type performs distinct roles and functions in *Drosophila* olfactory coding. Glomeruli are morphologically distinguishable areas in the AL containing the presynaptic terminals of ORNs that express the same olfactory receptors (OR) and contain dendrites of postsynaptic PNs. ORN termini release ACh onto PN dendrites and LN neurites. LNs interlink glomeruli via inhibitory and excitatory signals in the AL. Dendrites of PNs convey odors information in the glomeruli and carry output signals to downstream olfactory areas via PN axons (see Fig. 2.8). PNs and LNs form excitatory/ inhibitory reciprocal synapses that are thought to coordinate the transient oscillatory synchronization of spikes in groups of PNs in insects upon odor stimulation (reviewed in Okada et al., 2009; Tanaka et al., 2009). The insect olfactory system is presumably a discrete feedforward circuit since there is currently no evidence that the AL receives feedback from higher olfactory centers. This aspect represents a main difference from vertebrates in which the olfactory bulb receives extensive feedback (Masse et al., 2009).

The traditional view was that predominant signals between principal neurons (LNs) within different glomeruli were inhibitory signals or no spread of excitation. However, recent evidence suggested that the existence of excitatory connections between second-order neurons (PNs) in different glomeruli were mediated by LNs (Olsen et al., 2007; Root et al., 2007; Shang et al., 2007). The mechanism of lateral excitation is glomerulus-specific; as different PNs can receive either strong or weak lateral excitation depending on the glomerulus they innervate (Olsen et al., 2007). This heterogeneity reflects stronger electrical coupling with the excitatory LN (eLN) network in some glomeruli and weaker coupling in the others (Kazama and Wilson, 2008).

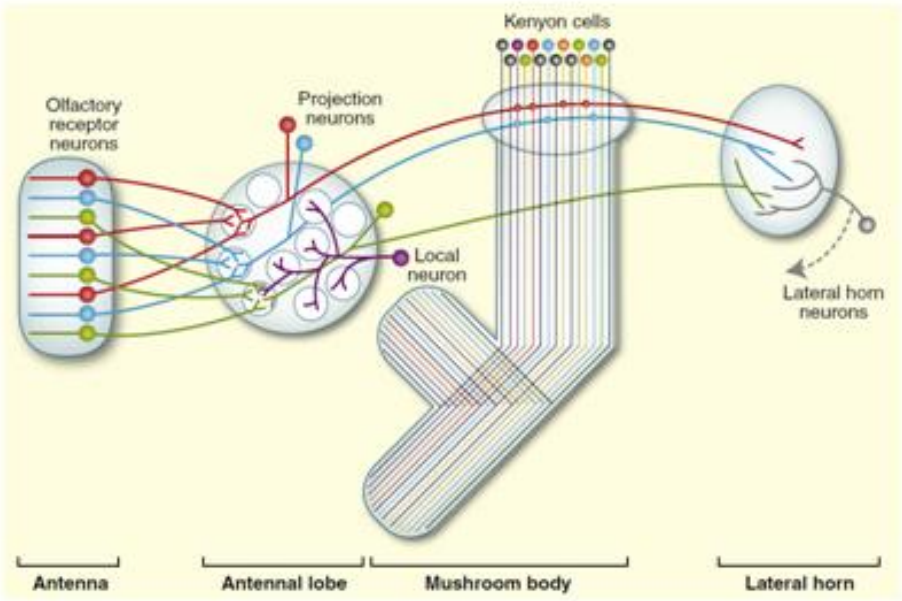

Fig. 2.8 Anatomy of the *Drosophila* olfactory system.

Olfactory receptor neurons in the antennae and maxillary palps are responsible to sense odors. These neurons project axons to specific glomeruli in the antennal lobe. They form synaptic contacts with projection neurons and local neurons (purple) in the glomeruli. The information is relayed by PNs and form synapses with Kenyon cells of the higher brain centers: the mushroom body (red and blue projection neurons) and the lateral horn (green projection neuron) (taken from Masse et al., 2009).

2.3.2 Olfactory receptors and olfactory receptor neurons

The vertebrate G protein-coupled receptor superfamily encodes olfactory receptors (ORs), which have inverted membrane topology when compared to insect-specific transmembrane ORs (Benton et al., 2006). They are expressed on the dendritic surface of ORNs, sitting in small sensory bristles or sensilla (antennae and maxillary palps) and each sensillum may contain several receptor neurons of different specificities (Fig. 2.8). Most antennal and all palp receptors belong to the OR family (Vosshall et al., 1999; Vosshall et al., 2000) which includes 62 receptors expressed in adult ORNs (Hansson et al., 2010). Expression of ORs in individual ORNs is not random, instead, each ORN expresses one very specific set of OR

(usually OR83b together with one receptor, but occasionally two or three) (Couto et al., 2005). Or83b represents a major class of ORs expressed in most ORNs (Larsson et al., 2004). They often heterodimerize with other ORs for trafficking to the dendrites and act as a co-receptor (Benton et al., 2006; Neuhaus et al., 2005). Or83b is the most conserved OR among insects and is proposed to contribute to an odorant-gated cation channel; whether this is achieved directly or relies on an intermediate cAMP second messenger remains uncertain (Hansson et al., 2009). Another receptor family that is expressed in most of the remaining antennal ORNs is probably related to ionotropic glutamate receptors (reviewed in Masse et al., 2009). It is likely that the binding of an odorant to a receptor can directly depolarize ORNs to generate action potentials (Benton et al., 2009).

In general, ORNs exhibit an odor-response profile that is characterized by the presence of a single class of ORs; these odor responses are temporally complex and a single type of OR can be excited by some odors and inhibited by others. ORNs expressing the same OR type converge at the same glomerulus and synapse with an average of three PNs (Vosshall et al., 2000). There are about 50 classes (25 per antenna) of ORNs identified and a complete projection map has been generated for 37 ORN classes with almost full coverage of the OR family. A total of 1300 ORN axons from each antenna project bilaterally to this primary processing area (AL) and each ORN forms synapses with all the PNs dendrites innervating a single glomerulus (Kazama and Wilson, 2009). Since each glomerulus receives input information exclusively from one class of ORNs, there are 52 glomeruli in total (reviewed in Masse et al., 2009).

2.3.3 Projection neurons

Around 150 uniglomerular PNs in each hemisphere convey odor input received from 1300 ORNs in the AL to the higher olfactory centers: the lateral horn (LH) and the mushroom bodies (MBs); PNs also provide local output within a glomerulus by forming synapses with diverse multiglomerular LNs. An important feature of the ORN-PN connection is the convergence of many ORN axons on a much lower number of PNs (reviewed in Masse et al., 2009). This connectivity is completely convergent, with each PN receiving input from all ORNs and each ORN synapsing onto all PNs (Kazama and Wilson, 2008). Each ORN–PN synapse consists of many release sites and distributes across many dendritic branches in each PN to ensure effective quantal summation (Gouwens and Wilson, 2009).

The response spectra of PNs are considerably broader when compared to their synaptic input counterparts from ORN. A particular odor evoking a strong activity in an ORN may not necessarily be the most efficient odor to activate its corresponding PN (Bhandawat et al., 2007). Electrophysiological studies have indicated a more complex transformation of odor information in PNs (Wilson et al., 2004; Kazama and Wilson, 2009). In the fly AL, PNs are reciprocally coupled to other PNs via mixed electrical/chemical synapses in the same glomerulus (Kazama and Wilson, 2009). This is similar as in the mouse olfactory bulb, where electrical synapses between sister mitral cells are required for the proper development of chemical synapses between these cells (Yaksi and Wilson, 2010). Recently the discovery of excitatory cholinergic LNs (eLNs) also broadened the response spectra of individual PNs, since resultant PN responses were conventionally thought to be shaped solely by inhibitory actions mediated by GABAergic LN (iLNs) (Fiala, 2007).

2.3.4 Local interneurons

The AL contains ~200 LNs, which form widespread connections of many glomeruli and build up a complex network transferring information. Unlike PNs, LNs do not project outside the AL, only forming synaptic connections extensively throughout the AL between and within glomeruli. Multiglomerular LNs interconnect glomeruli, where they extend dendrites and form dendrodendritic synapses onto PNs. They also receive input from both ORNs and PNs (reviewed in Masse et al., 2009). Multiglomerular LNs, which are diverse with respect to their transmitters, project throughout large parts of the AL. LNs can be inhibitory or excitatory, releasing GABA or ACh, respectively. LNs have been shown to inhibit the output of ORNs in *Drosophila*, suggesting their involvement in controlling the gain of olfactory responses (Olsen and Wilson, 2008a).

2.3.4.1 Inhibitory local interneurons

Synthesis of GABA transmitter and expression of both ionotropic and metabotropic GABA receptors are detected in LNs (Okada et al., 2009). The enhancer-trap line (Introduction section 2.6) Gad1-GAL4 (Glutamic acid decarboxylase 1) marks all GABAergic cells by mirroring the expression pattern of a gene involved in the GABA production. LNs are the dominant providers of GABAergic signals in the AL because the Gad1-expressing PNs of the middle antennocerebral tract have few presynaptic sites (Okada et al., 2009). The GABA transmitter is likely to be the sole mediator of inhibitory signals and is perceived by most of the neurons in the AL neural circuitry. GABAergic LNs in the AL are a subpopulation of

GABAergic neurons which are suggested to play cruical roles in odor coding and processing (Okada et al., 2009). GABAergic inhibition from LNs may mediate the oscillatory synchronization of AL neurons upon odor stimulation (Tanaka et al., 2009).

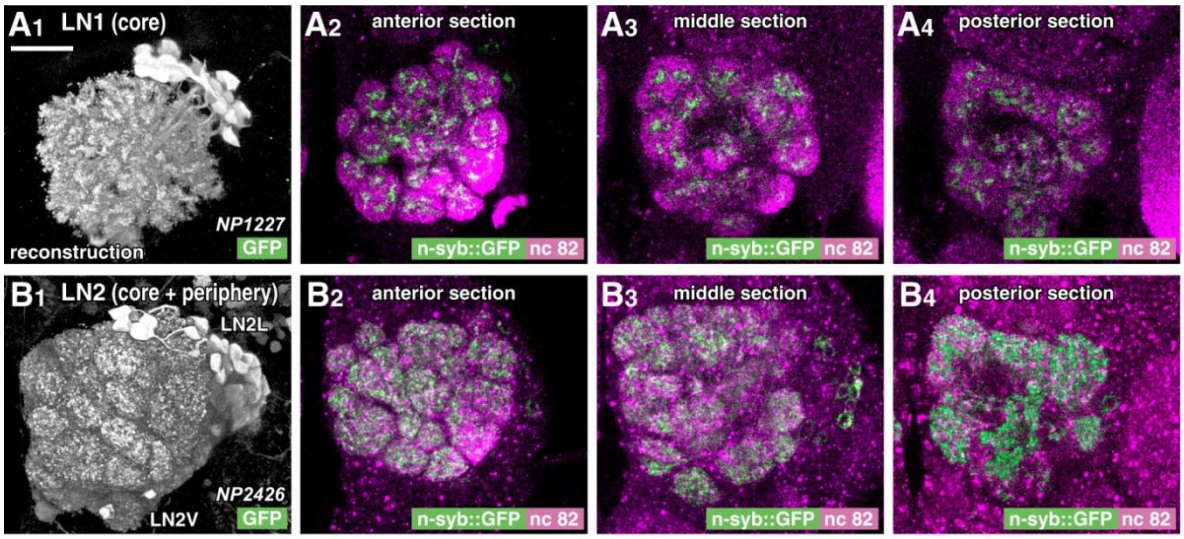

Fig. 2.9 Putative presynaptic sites of the *np1227*-GAL4 and *np2426*-GAL4 lines.
(A) Morphology of the entire cell population of LN1 (A1) and visualization of the presynaptic sites by driving n-syb::GFP expression in the anterior, middle, and posterior regions of the AL (A2–A4) (green). Neuropiles of the AL glomeruli were labeled with BRP^{Nc82} antibodies (magenta). (B) Morphology of the entire cell population of LN2 (B1) and distribution of presynaptic sites (B2–B4). Three-dimensional reconstruction (A1, B1) and single confocal optical sections (A2–A4 and B2–B4) of the AL (taken from Okada et al., 2009).

Two major populations of unilateral LNs (LN1 and LN2) have been originally identified in the *Drosophila* AL and can most readily be distinguished by their GAL4 enhancer-trap (see Introduction section 2.6): LN1 by *np1227*, and LN2 by *np2426* (Okada et al., 2009; Tanaka et al., 2009). The LN1 cells innervate the core areas of the glomeruli specifically do not overlap with the areas of ORNs termini, while LN2 cells are more abundant and cluster throughout the entire glomerulus (both core and peripheral areas) (Okada et al., 2009) (see Fig. 2.9A1 and B1). The number of labeled LNs cells, LN1 (*np1227*, 31–48 cells) and LN2 (*np2426*, 15–22 cells) were reported in Okada et al., 2009. This architectural distinction suggests that these two LN populations might participate in different neural circuits, serving distinct functional properties in olfactory processing (Okada et al., 2009; Tanaka et al., 2009). Synaptic transmission from widely branching population of LN2 cells is also found to be necessary for the generation of odor evoked neural oscillations, but not the transmission of LN1 cells (Tanaka et al., 2009).

A recent study by the Luo group examined several additional iLN populations with different identities (Chou et al., 2010). In brief, I will focus on the following iLN subtypes in this thesis: *np3056*-GAL4 covers the largest iLN population; it includes all cells that were labeled

by *hb8-145*-GAL4, *lcch3*-GAL4 and *krasavietz*-GAL4 (Chou et al., 2010). *np6277*-GAL4 is also broadly expressed in many cell types close to the AL and, in addition, in ORNs. Lines *hb4-93*-GAL4 and *hb8-145*-GAL4 drive expression also in a subset of ORNs; *hb4-93*-GAL4 drives expression also in a subset of PNs (Chou et al., 2010).

Table 2.1. Summary of the number of LN subpopulations labeled by individual GAL4 lines and their corresponding neurotransmitter profiles used in this thesis.

Estimate of the number of LNs (±SD) labeled by individual GAL4 lines reported in Chou et al., 2010. The relative amounts of GABA and choline acetyltransferase (ChA) expression is given on the lower rows of the table (±SD). The neurotransmitter profiles of *np6277* and *hb4-93* were not estimated (data are adopted and summarized from Chou et al., 2010).

	LNs-GAL4 lines					
	np3056	***lcch3***	***hb8-145***	***hb4-93***	***np6277***	***krasavietz***
No. of LNs	56±4	30±8	7±1	35±3	519±30	16±4
	Average No. of cells/ AL					
GABA+	42±10	20±6	7±1	/	/	12±3
ChA+	2±3	0.3±0.9	0	/	/	2±1
GABA-, ChA-	14±9	5±5	0.4±0.5	/	/	5±2

2.3.4.2 Excitatory local interneurons

Some recent studies have suggested that some LNs (*krasavietz*-GAL4) can be excitatory (Olsen et al., 2007; Shang et al., 2007), although LNs are traditionally believed to be inhibitory neurons that release GABA as their neurotransmitter. *Krasavietz*-GAL4 was first identified as a major eLN driver (Shang et al., 2007), though later studies by other groups provided evidence that it is a mixed eLN/iLN driver with a debatable proportion of eLN populations (Chou et al., 2010; Huang et al., 2010; Seki et al., 2010; Acebes et al., 2011). *Krasavietz*-GAL4 labels an eLN population and the majority of the GABA-negative *krasavietz*-GAL4 LN somata are located ventrolateral to the AL neuropile (Fig. 2.10). The lateral excitation of PNs by eLNs is mediated solely by electrical synapses, which transmit both depolarization and hyperpolarization from eLNs onto PNs (Yaksi and Wilson, 2010). Each eLN is connected to most or all PNs but excitation is not via chemical synapses. All PNs converge onto each eLN and each eLN receives excitation from most or all PNs. PN-to-eLN synapses connection in the reverse direction was found to consist of mixed chemical-electrical synapses (Yaksi and Wilson, 2010).

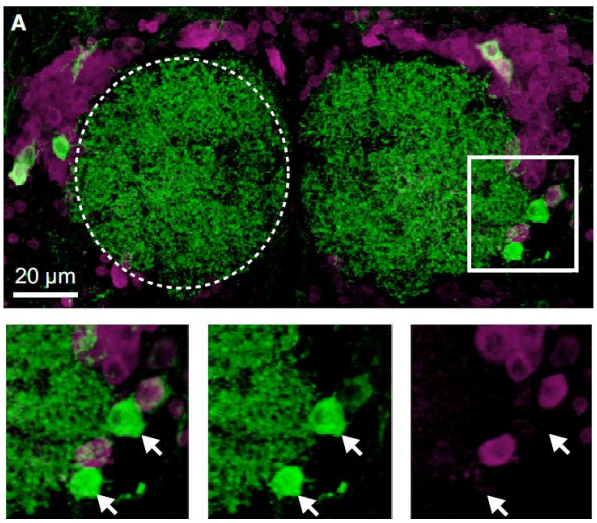

Figure 2.10 Excitatory LNs in the AL.
(A) Confocal z stack projection of the AL (genotype *krasavietz*-Gal4,*UAS-CD8:GFP*). Anti-GABA immunofluorescence (magenta) labels GABAergic neurons and CD8:GFP (green) labels *krasavietz*-GAL4 LNs population. Some ventrolateral LN somata are GABA negative and highlighted in the inset. LN dendrites are shown in dotted circle (taken from Yaksi and Wilson, 2010).

eLNs were first proposed to excite PNs by releasing ACh (Shang et al., 2007), however, it was later suggested that ACh is only used as a transmitter for eLN-to-iLN synapses (Yaksi and Wilson, 2010) but not for excitation of PNs. eLN-to-iLN synapses are also electrically coupled and this electrical component is pivotal for the proper development of the chemical component in eLN-to-iLN synapses (Yaksi and Wilson, 2010). iLNs can release GABA onto eLNs and exert a strong inhibitory connection in the opposite direction. eLNs and iLNs are interconnected and eLNs plays a role in the GABAergic inhibition recruitment. The major function of eLNs is GABAergic inhibition since eLN synapses onto iLNs are stronger than their synapses onto PNs. eLNs provide an important source of excitatory drive to iLNs (Yaksi and Wilson, 2010), although iLNs also receive excitatory input from PNs (Wilson et al., 2004). Abolishment of eLN-to-iLN synapse transmission boosted some PN odor responses and reduced the disinhibitory effect of GABA receptor antagonists on PNs. Taken together, eLNs exert two opposing effects on PNs by driving both direct excitation and indirect inhibition via synapses between eLN and iLN (Yaksi and Wilson, 2010).

2.3.5 Mushroom bodies form the higher olfactory center

The MB in the *Drosophila* adult brain is a prominent neuropile, which resembles the shape of a mushroom. Intrinsic third-order olfactory pathway neurons, Kenyon cells (KCs) form three fundamental compartments of the MB: calyx, peduncle and the lobes. Around 2000 to 2500 KCs build up the MB of each hemisphere (Aso et al., 2009; Heisenberg, 2003). They are classified into diverse subclasses according to their birth order, gene expression and axonal

projections. γ-neurons develop until the mid-larval stage (33%); followed by α'/β'-neurons (18%) during late larval stages; α/β- neurons (49%) are generated the last, during early to late pupal stages (Lee et al., 1999; Aso et al., 2009). KC cell bodies cluster in the dorsal posterior area of the brain and neurites project toward the anterior side to form the calyx by dendritic branching and conversion to form the peduncle (Fig. 2.11). The KC axons bifurcate dorsally and medially to form the vertical and medial lobes at the anterior end of the peduncle. The vertical lobe consists of the α and α' lobes, whereas the medial lobe can be subdivided into the γ, β and β' lobes (Ito et al., 1998; Crittenden et al., 1998). The α, α', β and β' lobes are divided into three strata, whereas the γ lobe appears more homogeneous (Fig. 2.11).

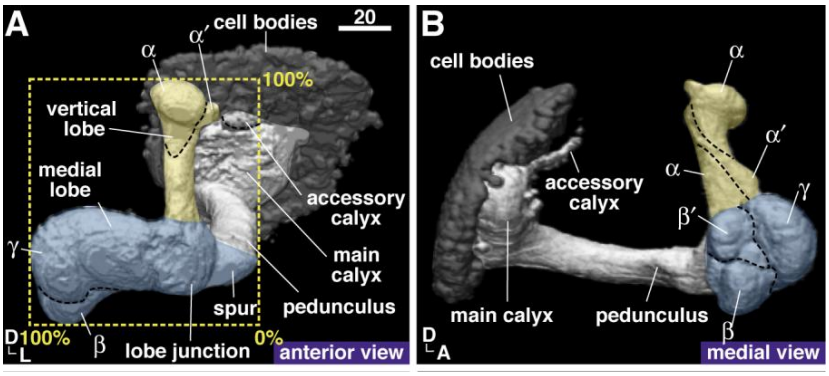

Fig. 2.11 Three-dimensional reconstruction of the MB.

Anterior (A) and medial (B) views of the MB in the left hemisphere with cell bodies. Cell bodies (dark gray) of KCs in the posterior cortex of the MB extend their axons to medial (blue) and vertical (yellow) lobes through the peduncle (light gray). KCs have their arborizations into the calyx (light gray) near the posterior edge of the peduncle and some arborizations also extend to the accessory calyx anteriorly. A, anterior; D, dorsal; L, lateral. Scale bar: 20 μm (taken from Tanaka et al., 2008).

Various KC subtypes perform differential roles in distinctive processes of olfactory learning and memory. Temporal inhibition of synaptic transmission of the chemical synapses to different subsets of KCs revealed that the output from α/β-lobes is required for memory retrieval, whereas output from α'/β'-KCs is necessary for acquisition and consolidation of a stable olfactory memory (Krashes et al., 2007). α-lobe neurons are proposed to contribute to long-term memory formation (Pascual and Preat, 2001), which was supported by later optical imaging experiments that indicated a change in α-lobe activity as a result of a training procedure that induces long-term memory (Yu et al., 2006). It remains crucial to understand how the relevant cell-signaling cascades function in the appropriate KCs subpopulations. In addition, a pair of MB innervating neurons provide a feedback loop between different lobe systems as a consolidation signal, whose constitutive activity is essential for aversive and appetitive memory stabilization (reviewed in Keene and Waddell, 2007). A number of extrinsic neurons are involved in olfactory learning and memory as well, which connect the

MB and other areas of the brain neuropiles; some of these neurons provide input and others are neuromodulatory (Tanaka et al., 2008). They arborize in only limited areas of each MB lobe and the internal arrangement of these neurons might represent the functional diversity of the lobe systems (Tanaka et al., 2008).

2.3.5.1 Synaptic organization in the adult Drosophila MB calyx

Microglomerulus structures are synaptic complexes in the adult calyx that comprise PN boutons, surrounded by a number of small postsynaptic profiles, including KCs and additional neurons (Yasuyama et al., 2002). Most presynaptic PN boutons are cholinergic and each individual PN bouton constitutes the center of a single microglomerulus (Fig. 2.12A). In the calyx, multiple presynaptic puncta (Brp^{Nc82} label) tightly outlining the inner edge of claw-like structures, juxtapose with each other and an abundant percentage of puncta within the microglomerular centers was detected (52%) (Leiss et al., 2009). The calyx is also densely innervated by extrinsic neurons that synthesize GABA and form synapses with both KCs and PNs within microglomeruli, reciprocally connecting these two elements (Yasuyama et al., 2002).

Olfactory information transfers from PNs to their postsynaptic partners, KCs, which have their dendrites in the MB calyx, where PNs mainly form presynapses. Presynaptic sites of KCs were formerly believed to be restricted to axonal elaborations within the MB lobes. Our lab demonstrated that KC neurites within the calyx of larval and adult *Drosophila* are therefore not exclusively postsynaptic but also form presynaptic AZs (KC-derived AZs in the calyx, KCACs) (Christiansen et al., 2011). Only α and α/β KC subpopulations, but not α'/β' form KCACs (Christiansen et al., 2011). Apart from this prominent way of KC-PN connectivity (KCACs), mixed identity of presynapses or AZ and postsynaptic specfication are found in KC neurite (Fig. 2.12B). The distal part of the KC neurite receives synaptic input from its major connection with a PN bouton. Presynaptic release sites along the promixal part of indivdual KC neurite represent new presynaptic elements in the calyx (Fig. 2.12C, D; Christiansen et al., 2011). Proposed connectivity of the newly identified KCACs are between KC-KC, KC-iLN or KC-PN. KCACs may also act as recurrent synapses transmitting information back to the calyx or MB lobes. These newly identified KC-derived presynapses in the calyx are hence candidate sites for memory trace formation during olfactory learning (Christiansen et al., 2011). Finding the postsynaptic partners of KCACs will be highly relevant to undertand the functional context of KCACs.

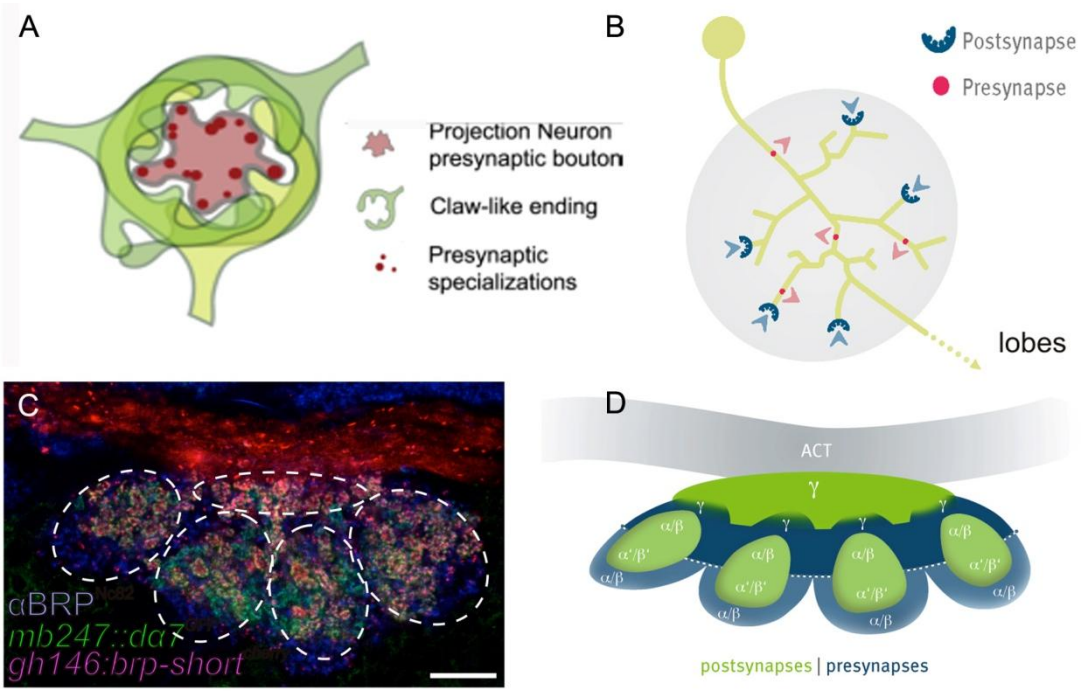

Fig. 2.12 Synaptic organizations in the adult calyx.

(A) Several KCs form claw-like endings (shades of green) encircle and receive synapses (red puncta: presynaptic sites) from a PN bouton (light red). (B) Schematic drawing indicating synaptic input and output sites on a single KC within the calyx. (C) Calycal microglomeruli are visualized by *UAS-brp-short*^{cherry} expressed in PNs (*gh146*-GAL4) and Dα7 expressed in KCs (*mb247::dα7GFP*). Presynaptic label by αBRP^{Nc82} is shown in blue. Five subunits of calyx are shown (in dotted circles), each harboring microglomeruli in the center and other synapses surrounded the central region. (D) Schematic drawing of the distribution of the pre- and postsynaptic regions of different KC subtype within the MB calyx. Presynapses are shown in blue and postsynapses in green. Scale bars: 100 μm (taken from Leiss et al., 2009; Christiansen et al., 2011).

2.3.6 The use of transgenic tools in visualizing AZs in the adult CNS

The AZ protein BRP shapes the T bar at the presynaptic AZ and is essential for proper AZ function. A fluorescently tagged BRP fragment (*UAS-bruchpilot-short*^{GFP}) (Schmid et al., 2008) represents a specific AZ marker and depends on endogenous BRP for localization. This dependence gives us a good estimate of the number of AZs with T bars. This BRP-derived construct labels AZs (Schmid et al., 2008) without changing number of synapses (Kremer et al., 2010). Together with the previously designed transgenic tool specific for PSDs visualization (GFP-labeled acetylcholine receptor subunits, *UAS-Dα7*^{GFP}, Kremer et al., 2010), it enables us to unravel synaptic circuits of the MB (Christiansen et al., 2011) and to assess experience-dependent changes in connectivity (Kremer et al., 2010) (staining see Fig. 2.12C).

2.4 Genetic screens for the generation of mutant alleles

Transposable elements are natural and ubiquitous components of genomes with a distribution ranging from bacteria to vertebrates (Berg and Howe, 1989). *P*, *PiggyBac* and *Minos* elements

are the three major well-characterized transposons in *Drosophila melanogaster*, which represent invaluable experimental tools for genetic manipulation and molecular genetic analysis. The Berkeley *Drosophila* Genome Project (BDGP) strives to disrupt each *Drosophila* gene by single transposable element inserted in a defined genomic region since 1993. The library at the Bloomington Stock Center offers a public resource of mutant strains that facilitate the application of *Drosophila* genetics to understand diverse biological problems. Up to date, the size of the BDGP gene disruption collection is up to ~14,740 strains (selected from *P* or *piggyBac* element integrations and newly generated *Minos* transposon insertions) and has achieved more than a 95 % coverage of *Drosophila* genes, which are therefore now under experimental control within their native genomic contexts (Bellen et al., 2011).

2.4.1 Site-specific genomic deletions by FLP-FRT recombination

PiggyBac elements identified in *Trichoplusia ni* (cabbage looper moth) are transposable elements that were introduced to the genome of *D. melanogaster* via germline transformation (Handler and Harrell, 1999). *PiggyBacs* show a global and local gene tagging behavior that is distinct from that of *P* elements; they do not share the same chromosomal hotspots (Thibault et al., 2004). A preference for insertions into introns has been reported for *piggyBac* elements (Häcker et al., 2003). *PiggyBacs* are more effective at gene disruption as they lack the *P* bias for insertion in the 5′ regulatory sequences; excisions in the germ line are nearly always precise. Therefore they constitute the most promising transposon for the application of generating strong loss-of-function alleles. They also show low remobilization rates, as was observed with a heat shock–inducible transposase (Thibault et al., 2004).

The elements used in the Exelixis collection are characterized by containing FRT sites of 199 bp either 5' (in *XP* and *WH* transposons) or 3′ (in *RB* transposons) of the *white*$^+$ (w^+) transgene (Fig. 2.13A; Thibault et al., 2004). Heat shock–driven FLP recombinase (*hs-FLP*) activates *trans*-recombination between FRT elements, resulting in genomic deletion with a single residual element tagging the deletion site. This strategy makes it possible to efficiently generate small custom deletions with molecularly defined endpoints throughout the genome. Deletions can initially be detected in the progeny by a loss or gain of the w^+ marker, depending on the type of insertions in the parental lines, their genomic orientation and the relative position of w^+ with respect to the FRTs (Fig. 2.13B). The crosses outlined (Fig. 2.13C) allow the efficient recovery of deletions within four generations. PCR screens for the

presence of the residual FRT element ends by using paired element-specific and genome-specific primers (two-sided PCR) or by PCR detection of a resulting hybrid element using element-specific primers (hybrid PCR) provide the final confirmation of the deletion ends (Fig. 2.13D).

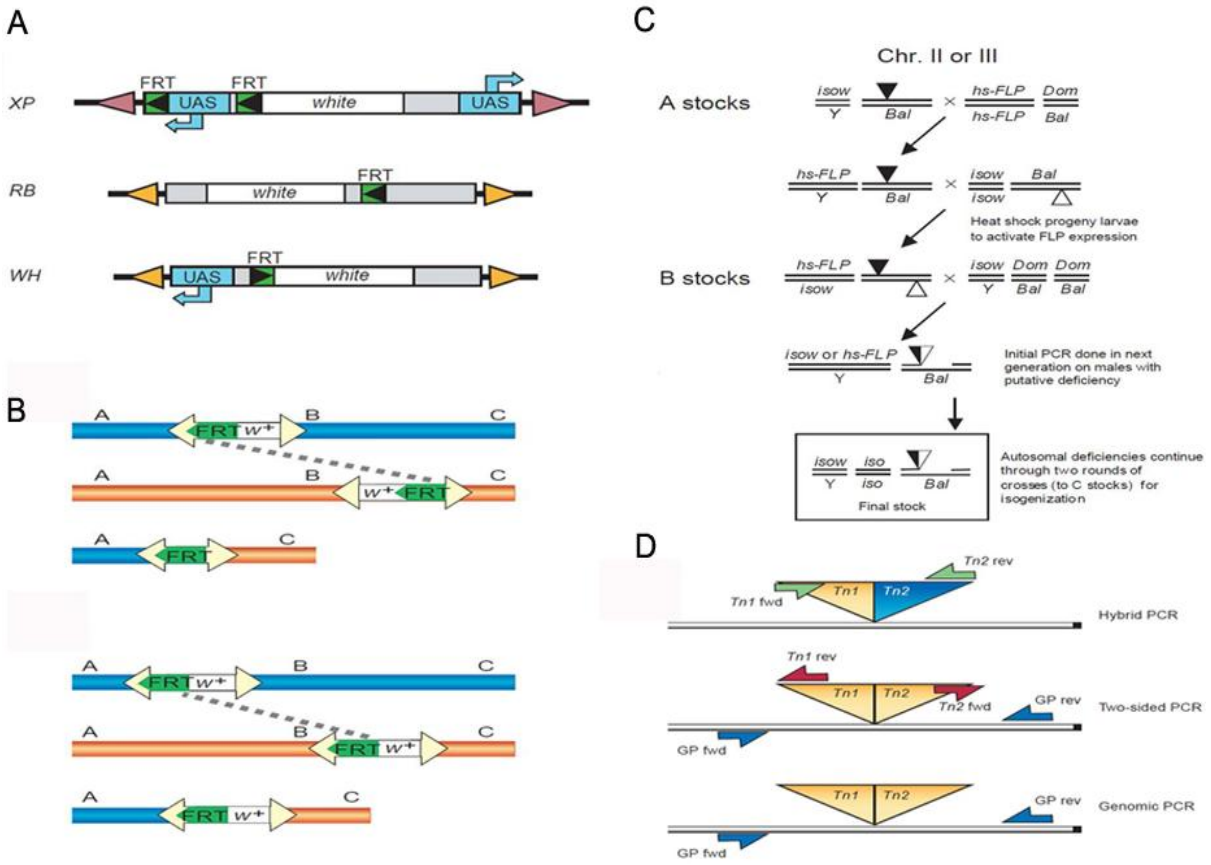

Fig 2.13 Schematic diagrams for deficiency generation by FLP-mediated recombination.
(A) Schematic of the three different transposon types used in FLP-FRT–based deletions (*XP*, *RB* and *WH*). The orientation of FRT sites (direction of the arrowheads), UAS-containing sequences and the *white* (*w*) gene are indicated (see Thibault et al., 2004 for detail). (B) w^- (upper panel) and w^+ (lower panel) deficiency generation by using FLP-FRT recombination (C) Genetic scheme to generate FLP-FRT–based deletions, using *P or piggyBac* insertions on Chromosome II or III as an example. Two FRT-bearing transposon insertions (triangles) are placed in *trans* in the presence of heat shock–driven FLP recombinase (*hs-FLP*). The generation of deletions upon FLP recombinase activation can be later detected by PCR. *Dom*, dominant visible marker mutation; *iso* (D) Transposon-specific primers were used to detect the presence of a fragment of known size across the newly formed hybrid (hybrid PCR). A genomic primer in combination with a transposon-specific primer for both ends of the transposon were used (two-sided PCR). Genomic primers for additional confirmation by PCR were also carried out (genomic PCR) (taken from Parks et al., 2004).

2.4.2 *P*-element imprecise excision screening

P-transposable elements transpose at high rates, depend completely on an exogenous transposase and serve as the most widely used transposable elements in genetic manipulations of the fly (Engels, 1983). Much information about the function of *D. melanogaster* genes can be gained by *P*-element mutagenesis. Yet the major drawback of this method is its strong bias for insertion at hotspots. There is a medium probability for another group of loci (warmspots)

and a bias against insertion into others (coldspots). 5′-UTRs are preferential targets for their integration within genes (Spradling et al., 1995). *P*-elements inserted near gene promoters can be mobilized preferentially (Spradling et al., 1995) and mobilization of single elements or of DNA between element pairs occasionally generates imprecise local deletions of genes (reviewed in Gray, 2000). During mobilization, mutational events can also be associated with the excision of all or part of a *P* element upon transposase activation. However, only a minority of the *P*-elements removes a random part of the adjacent genomic regions when mobilized in an imprecise excision screen.

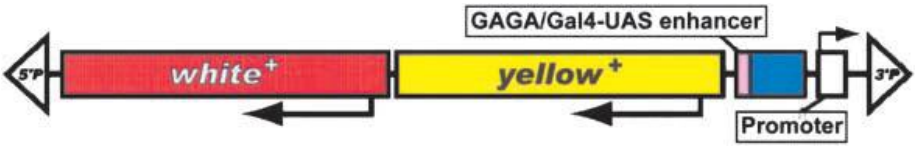

Fig. 2.14 *P*-element–based EY transposon.
The *P*-element–based EY transposon (P{EPgy2}) features a *white*$^+$ and an intronless *yellow*$^+$ gene that transcribed in the same direction; they lie in opposite orientation to the *P*-element promoter (taken from Bellen et al., 2004).

For imprecise excision deletions by mobilizing a single *P*-element (e.g. see construct in Fig. 2.14), a parental fly strain with a *P*-element inserted in or near the gene of interest is crossed to a strain carrying the Δ2-3 transposase. Then one screens for progeny that lacks the genetic *P*-element marker. Progeny with a loss of w^+ eye color indicates successful mobilization of *P*-elements. Subsequent genomic PCR screens by specific primers identify and validate imprecise excision events.

2.4.3 *Minos* element transposons in genetic screening

Minos was first discovered as a 1.8 kb long transposon of *D. hydei*, as one of the members of the widely dispersed class of Tc1-like transposons (Franz and Savakis, 1991). *Minos*-based transposon plasmids and vectors have been used successfully for the germ line transformation of diverse organisms and cultured cells (Loukeris et al., 1995a; Loukeris et al., 1995b; Zagoraiou et al., 2001; Klinakis et al., 2000). About 30 % of all insertions were in introns and around 55 % of insertions were within or next to genes that had not been hit by *P*-elements (Metaxakis et al., 2005). In contrast to other transposons, little sequence requirement beyond the TA dinucleotide insertion target is required for the insertion sites (Metaxakis et al., 2005). Therefore, the *Minos* element from *D. hydei* is very suitable as a tool for *Drosophila* genomics.

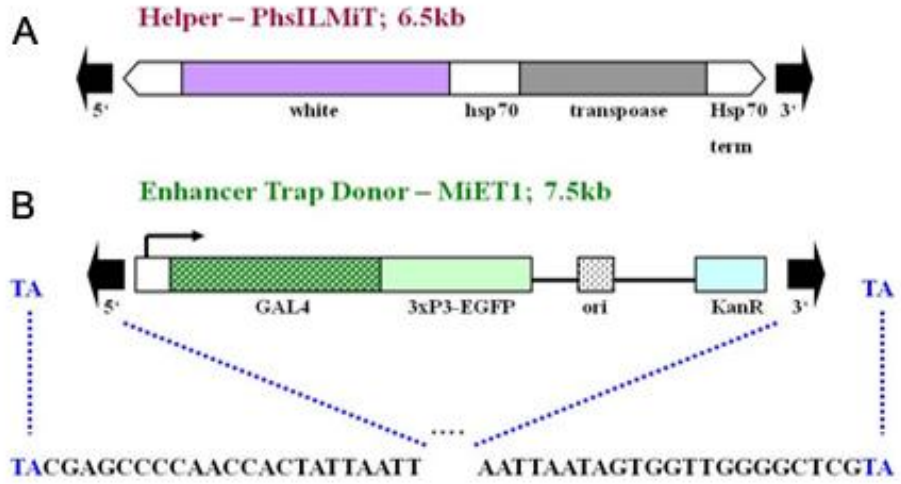

Fig 2.15 *Minos* donar and corresponding helper plasmid.
(A) Schematic diagram depicted the details of the helper plasmid (PhsILMiT) that expresses the *Minos* transposase for triggering the mobilization of a *Minos* element upon heat-shock activation. (B) The *Minos* transposable donor construct (MiET1) contained the 3xPax6/EGFP dominant marker (Berghammer et al., 1999), containing tandem repeat TA boxes (blue), flanking both 5' and 3' ends (adapted from Metaxakis et al., 2005).

We put our focus on one of the *Minos* donor constructs, pMiET1, based on the transposon donor pMiPR1 (Metaxakis et al., 2005), which contains the 3xPax6/EGFP dominant marker (Berghammer et al., 1999) (Fig. 2.15B). The plasmid pPhsILMiT is a derivative of the *P*-element vector pCaSper4 (Thummel and Pirrotta, 1992) and of pHSS6hsILMi20 (Klinakis et al., 2000), which contains an intronless *Minos* transposase gene under control of the hsp70 promoter as the source for heat-activated transposase (Fig. 2.15A). Stable fly lines producing *Minos* transposase from a balancer chromosome were established by co-injecting *D. melanogaster* embryos carrying the CyO balancer with the helper plasmid Δ2-3 (Laski et al., 1986) and the *P*-element-based plasmid pPhsILMiT (Metaxakis et al., 2005). The jump-start males were heat-shocked daily at 37 °C for 1 hr during the larval and pupal stages and transposition efficiency of 81 % was observed. No remobilization was detected when the jump-start males were kept continuously at 25 °C or 30 °C. Induced remobilization of *Minos* insertions can excise nearby sequences. *Minos* serves as a useful tool that complements the *P* element for insertional mutagenesis and genomic analysis in *Drosophila*.

2.5 P[acman]: A bacterial artificial chromosome (BAC) transgenic platform

Highly efficient phage-based *Escherichia coli* homologous recombination systems and recombineering techniques are widely used for manipulating large DNA fragments in mouse genetics. Mammalian genomic DNA can also be modified and sub-cloned into bacterial artificial chromosomes (BACs) (reviewed in Copeland et al., 2001). Due to the lack of appropriate genetic tools in *Drosophila* system, it remains a solid barrier to facilitate

structure/function analyses of large genes and gene complexes. Recent advances in integrating three essential technologies, conditionally amplifiable BACs, recombineering, and bacteriophage PhiC31–mediated transgenesis, provide us with a reliable platform to overcome the conventional challenges in cloning large DNA fragments of *Drosophila* genes (Venken et al., 2006).

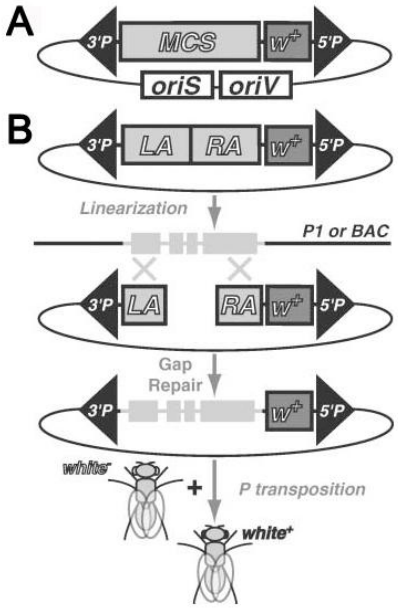

Fig. 2.16 P[acman]: BAC transgenesis in *Drosophila*.

(A) P[acman] vector contains *P*-element transposase sites (3'*P* and 5'*P*), a *white*$^{+}$ gene, an multiple cloning site (MCS), a low-copy origin of replication (*oriS*) and a copy-inducible origin of replication (*oriV*) are indicated. (B) P[acman] is linearized between both homology arms (LA and RA) and transformed into recombineering bacteria containing BAC clones. Integration into the germ line of *white*$^{-}$ flies is mediated by *P*-element–mediated transformation (taken from Venken et al., 2006).

In brief, this new transgenesis platform involves two key steps: recombineering-mediated gap repair on the genetically engineered P[acman] vector and PhiC31-mediated integration of P[acman] into the fly genome. Left and right homology arms (LA and RA) are located at either end of the targeted DNA fragment. They are first cloned and ligated into the multiple cloning site (MCS) of the *attB*-P[acman]-Ap^{R} vector (Fig. 2.16B). The donor vector that contains the necessary genomic clone (P1 or BAC clones) is transformed into a recombineering-competent *E. coli* strain in parallel. Linearized *attB*-P[acman]-Ap^{R} construct (between both homology arms LA and RA) is then transformed into the recombineering-competent *E. coli* strain that harbors the desired genomic clone for subsequent recombineering (Fig. 2.16B). Colony PCR screening identifies correct recombination events at both junctions after gap repair and subsequent DNA sequencing verifies the presence of the desired fragment.

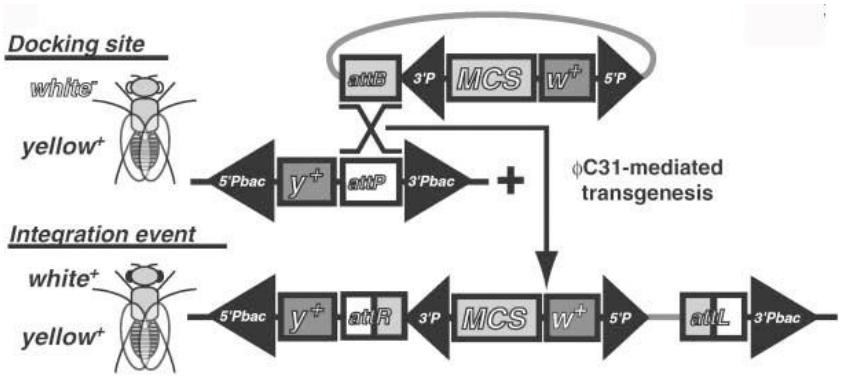

Fig. 2.17 P[acman] transgenesis in *Drosophila* using the PhiC31 system.

attB-P[acman] can integrate at an *attP* docking site (VK lines in Venken et al., 2006) in the fly genome mediated by the PhiC31 system. Successful integration events is indicated by a positive amplification of *attL* (left attachment) and *attR* (right attachment) sites in a PCR screen (taken from Venken et al., 2006).

P-element-mediated transformation still causes genes disruption and position effects that potentially affect the levels or patterns of transgene expression (Venken et al., 2006). PhiC31-mediated transgenesis circumvents this limitation by offering site-specific integration of large DNA fragments at specific docking sites in the *Drosophila* genome. For the integration of *attB*-P[acman] into the fly genome, both circular plasmid DNA of the *attB*-P[acman] construct and mRNA encoding PhiC31-integrase are co-injected into embryos carrying the *piggyBac-yellow*$^{+}$*-attP* docking site (Fig. 2.17). PhiC31-integrase (from bacteriophage PhiC31) mediates recombination between a bacterial attachment (*attB*) site in the injected plasmid and an engineered "docking" site containing a phage attachment (*attP*) site in the fly genome (Groth et al., 2004, Fig. 2.17). Successful integration events of *attB*-P[acman] can be genetically traced by screening for transgenic flies with both *yellow*$^{+}$ body color and *white*$^{+}$ eye color phenotypes (Fig. 2.17). Later validation of correct integration events can be conducted by confirming the loss of the *attP* PCR product (specific for the original docking site) and the positive amplicons of both *attL* and *attR* (specific for the integration event at left and right attachment sites (Fig. 2.17)). The efficacy of the integration events depends both on the size of the DNA fragment inserted and the position of docking sites chosen. The capacity (maximum length of DNA insert) of the *attB*-P[acman] vector reported so far is for Hepatocyte nuclear factor 4 (*Hnf4*), around 105 kb, with an integration efficiency of 1.6 % (Veneken et al., 2009).

2.6 *P*-element vectors for transgene expression and enhancer trapping

The binary GAL4-UAS system is one prevalent approach in *Drosophila* (Brand and Perrimon, 1993) to over-express a transgene artificially via fusion of the gene target to a specific promoter in a *P*-element vector (Serano et al., 1994). The yeast transcription factor GAL4

(promotional activator) is a reporter gene that recognize its *cis*-acting element, the Upstream Activating Sequence (UAS). The transcription/expression of the gene of interest under the control of UAS promoter is only activated in cells where GAL4 is expressed and depends on the insertion site of the GAL4 (O'Kane and Gehring, 1987). The enhancer-trap technique represents a procedure for placing regulatory elements of a known gene (particular cell type for UAS construct expression) upstream of GAL4 and subsequent cloning into a *P* transformation vector to create a P[GAL4] line. GAL4 may be expressed in various tissues by creating enhancer-trap lines under the control of specific endogenous promoters. In flies, minimal GAL4 activity is present at 16 °C, while maximal GAL4 activity is observed at 29 °C with minimal effects on fertility and viability (Duffy, 2002).

2.7 Objectives of the study

Our lab studies the structural and functional principles of active zone organization at *Drosophila* neuromuscular synapses. Our group had identified the protein BRP as a major building block structuring the active zone core. On central subject of this thesis was to explore novel additional components of the BRP matrix.

First the role of RIM, a known family of active zone proteins, was analyzed. Analysis showed that RIM is not essential for active zone structure but plays a role for effective synaptic vesicles transmission in our system. RIM-binding protein (RIM-BP) before was identified as biochemical interactive partner of RIM (Wang et al., 2000) and Ca^{2+}-channels (Hibino et al., 2002; Kaeser et al., 2011). However, RIM-BP function had not been studied genetically. By generating of loss of function alleles, we find RIM-BP to be a central component of the active zone core, pivotal for structural and particular functional integrity of the active zone.

In the course of the analysis, it became clear that active zones of the *Drosophila* CNS are highly diversified concerning their relative amounts of DRBP and BRP. Genetic tools in combination with whole brain stainings were used to assign DRBP-rich synapses to particular neuron populations in the *Drosophila* olfactory system.

3. Material and Methods

3.1 Genetics and driver lines

All fly strains were, if not otherwise stated, reared under standard laboratory conditions at 25 °C supplied with standard cultivation medium (Sigrist et al., 2003). *drbp* alleles used for the behavioral and vitality assays were reared under semi-defined medium (Bloomington recipe). y1, w1118 was used as background for transgenesis. Estimated cytology docking site for integration of the *rim* and *drbp* genomic rescue construct was 28E7 and transgenesis was mediated by Phi31 system using P[acman] strain, PBac{yellow[+]-*attP*-3B}VK00002.

The following fly stocks and drivers were used: *P{w+=GawB}elav*^{C155} (*elav*(x)-GAL4) (Lin and Goodman, 1994), *ok107*-GAL4 (Connolly et al., 1996, Bloomington stock 854), *gh146*-GAL4 (Bloomington stock 30026), *or10a*-GAL4 (Bloomington stock 9944), *UAS-drbp-RNAi* (VDRC stock 46925; Dietzl et al., 2007), *UAS-Dα7*^{GFP} (Leiss et al., 2009; Kremer et al., 2010); *mb247*-GAL4, *UAS-bruchpilot-short*^{GFP}, *mb247*::bruchpilot-short^{GFP} (Christiansen et al., 2011); two major iLN drivers (*np1227*-GAL4 and *np2426*-GAL4), a mixed population of iLNs/ eLNs driver (*krasavietz*-GAL4) and an ORN driver (*or83b*-GAL4) were kindly provided by Sachse's lab (Seki et al., 2011); iLN subpopulation driver lines *np3056*-GAL4, *lcch3*-GAL4, *hb8-145*-GAL4, *hb4-93*-GAL4 and *np6277*-GAL4 used in this study were kindly provided by Luo's lab (Chou et al., 2010). Other fly stocks for mutation alleles screenings (*piggyBac* elements: PBac{WH}tinc[f01062], PBac{WH}Rim[f03825], PBac{WH} cpo[f01629] (3.4.1)) were obtained from Exelixis (Harvard); *P*-element P{EPgy2}Rim[EY05246] (3.4.2), *Minos* element insertions (Mi{ET1}MB07541, *rim*^{Minos} and Mi{ET1}MB02027, *drbp*^{Minos}) and deficiency stocks (*Df*(3R)*ED5785* and *Df*(3R)*BSC566*) were obtained from Bloomington stock center.

3.2 *In-situ* hybridization

For the *rim* cDNA template, total RNA of adult fly heads (strain *w*^{1118}) was extracted and transcribed into random hexamer primed cDNA using the Superscript III kit. Cloning of *rim* fragment into pBluescript® II KS+ (pKS+) vector by using restriction sites XhoI and NotI, amplified by primer pairs: 5′-CAAGACCTCGAGATCCAGCGACATGTGATTCC-3′ and 5'-GCGGCCGC TCTTCGGATCCTGCGATGTG-3'. All final constructs were double-strand sequenced before further use. Whole-mount embryonic in situ hybridizations were performed as described by the Berkeley *Drosophila* Genome Project (http://www.fruitfly.org/). The *rim*

sense RNA probe was linearized with XhoI and in vitro transcribed using T7 RNA polymerase. For antisense probes, the plasmid was cut with EcoRI, and SP6 RNA was *in vitro* transcribed.

3.3 Antibodies production

For the anti-DRBP$^{N\text{-}Term}$ antibody, a rabbit polyclonal antibody was raised against a 6×His-tagged fusion protein with the following sequence:
MQYGTGQTSVEKLLSGTSGITGIPPLPVNIHTMKAMPTALSQRGTIQLYNLQSTTMPL
LSLNSHNLPPAGSTSYSALGAGGGTSLTHPTMANLGLLDTGTLLGSTGLSGLGVGPSV
GGITGATSLYGLSGGGGGAGGLGSSYGPPFLDVASSASYPFTAAALRQASKMKMLDE
IDIPLTRYNRSSPCSPIPPNNWGLDEFTDGLSVSMMHNRGGLALGALDLDTRNHGLN
GASEPQVDMLDIPG
The fragment for expression was amplified from *drbp* cDNA clone AT04807 (*Drosophila* Genomics Resource Center) using primers: 5′-CACCATGCAGTACGGAACCGGACAG-3′ and 5′-CTATCCAGGAATATCGAGCATATC-3′ and TOPO cloned into pENTR D-TOPO.
For expression, the sequence was then transferred to pDEST17 by a Gateway reaction and expressed in *Escherichia coli* and purified using a protocol including denaturing and refolding of the protein. The antibody containing serum was affinity purified against the same peptide that was used for immunization.
For the anti-DRBP$^{C\text{-}Term}$ antibody, a rabbit polyclonal antibody was raised (Seqlab) against a C-terminal synthetic peptide (C-VLSKGKDLFGKF). The specificity of the affinity-purified anti-DRBP antibodies was confirmed by immuno-fluorescence analysis of larval muscle filet preparations of control and *drbp* mutant animals.

For the anti-RIM$^{N\text{-}Term}$ antibodies, two rabbit polyclonal antibody were raised (Seqlab) against N-terminal synthetic peptides (C-DEMPDLSHLTPHER and C-EEEKQNEIMRRK). For the anti-RIM$^{C\text{-}Term}$ antibodies, two rabbit polyclonal antibody were raised (Seqlab) against C-terminal synthetic peptides (C-EKKVFMGVAQIMLDD and C-SRRSSIASLDSLKL). However, we could not confirm the specificity of all the affinity-purified anti-RIM antibodies and we are not reporting any staining in this thesis.

3.4 Genetic screens for the generation of mutant alleles

In this thesis, we utilized the available genetic tools and attempted at generating deletion mutants as described (Introduction section 2.4). Studying these mutants offers a way to reach

a deeper understanding of the roles of AZ proteins of interest. Single flies genomic PCR was performed according to Gloor and Engels, 1992.

Squishing buffer (10 mM Tris/HCl pH 8.2, 1 mM EDTA, 25 mM NaCl, 200 µg/ml proteinase K) was used to extract the genetic materials for the single fly PCR. A primer pair was used to amplify a 547 bp amplicon as the internal control for all the single fly PCR and RT-PCR experiment: 5'- CATACACATACACTTGCACGC-3' and 5'-GCGGCCTGTAGAGTTCGTA-3.

3.4.1 FLP-FRT recombination deletion

rim$^{ex1.26}$*:* Screening of positive progeny by the gain of eye color during the deletion generation and confirmation of the presence of the residual element by PCR detection of a resulting hybrid element by RT-PCR. The presence of the parental line PBac{WH}tinc[f01062] was verified by getting a 531 bp amplicon amplified by the primers: 5'-TCATTAGCGCACAGCGAGCA-3' and WH3'-: 5'-CCTCGATATACAGACCGATAAAAC-3'; the other parental line PBac{WH}Rim[f03825] was verified by getting a 369 bp amplicon amplified by the primer pairs: WH5'-: 5'-TCCAAGCGGCGACTGAGATG-3' and 5'-GTGGACGCCATCGAGCAGTT-3'.

rim$^{ex2.40}$*:* Positive candidates from w^+ deletion generation crosses are screened and confirmed by PCR using genome-specific primer and the primer from the residual *piggyBac* element. The presence of parental line PBac{WH} cpo[f01629] was verified by having a 512 bp amplicon amplified by primers: WH5'-: 5'-TCCAAGCGGCGACTGAGATG-3' and 5'-CCATGCTGACCGGCAATAAT-3' and other parental line PBac{WH}Rim[f03825] was verified by having a 554 bp amplicon amplified by primer pairs: 5'-TGGCATTAGCAATCGGTACG-3' and WH3'-: 5'-CCTCGATATACAGACCGATAAAAC-3'.

The fly strain, *Df*(3R)*ED5785* was used as a deficiency chromosome for evaluating *rim* alleles. It carries a deleted segment from 90C2 to 90D1, corresponding to computed breakpoints in the 3R chromosome from 13543832-13769792.

Df(3R)*S201:* Screening of positive candidates by the loss of eye color in deletion generation and confirmed with the presence of a 1.7 kb amplicon by RT-PCR. Fusion product of both parental *piggyBac* elements was amplified by using primers described in Parks et al., 2004: XP5'+: 5'-AATGATTCGCAGTGGAAGGCT-3' and RB3'+: 5'-TGCATTTGCCTTTCGCCTTAT-3'.

3.4.2 *P*-element imprecise excision screen

One of the *P*-element–based transposon insertion lines constructed in the BDGP collection, P{EPgy2}Rim[EY05246] (Bellen et al., 2004, Fig. 2.15), was used for generating the imprecise excision *rim* alleles in this thesis, rim^{del71} and rim^{del103}. P{EPgy2}Rim[EY05246] (Bellen et al., 2004) is inserted 393 bp upstream of exon 16 of the predicted PB isoform of *rim*, located on the third chromosome. A fly strain carrying the Δ2-3 transposase on the second chromosome was used to activate *P*-element mobilization (see Fig. 3.1 for the crossing scheme).

Adult male flies from the progeny of the cross between the *P*-element and the transposase line (loss of w^+ eye color, see Fig. 3.1) were tested for imprecise and precise excision events via single fly genomic PCR. The fly strain, *Df*(3R)*BSC566* was used as a deficiency chromosome for evaluating *rim* alleles in the *P*-element imprecise excision screen. It carries a deleted segment from 90C2 to 90F6, corresponding to computed breakpoints in the 3R chromosome from 13581026-14023935. 10 genomic primer pairs of *rim* were designed for mapping imprecise excision events.

Region (-1) - 507 bp	5'-TGAGCACAGCACGCGAGAGA-3' and 5'-AGGAGAGGAGGAGGTGTATG-3'
Region (-2) - 411 bp	5'-CCTCCTCCTCTCCTCAGTCT-3' and 5'-TGCAGACAACTCAACATCCGCTCTT-3'
Region (-3) - 615 bp	5'- AGAGCGGATGTTGAGTTG-3' and 5'-TTCCATGCCACCATCTGA-3'
Region (-4) - 762 bp	5'-TGCTCGTGGTGCATCAGA-3' and 5'-CTACCTTGGGGTAGAGTT-3'
Region (-5) - 611 bp	5'-CCAAGGTAGTTCCTAAGT-3' and 5'-CACCCCGTAGCTTTAAGT-3'
Region (+1) - 341 bp	5'-GGCAGCGGTGGTAAGTGGTT-3' and 5'-CACACGCTTACACGGCAACTA-3'
Region (+2) -535 bp	5'-TTGGACCGTCGTGGTGGATA-3' and 5'-CACTTACCACCGCTGCCAAC-3'
Region (+3) - 547 bp	5'-GAGGTGCAGCAGTTGCCATTTG-3' and 5'-ACGACGGTCCAACGGACTGA-3'
Region (+4) - 616 bp	5'-GCAGATTCCTTCGGCGCTTC-3' and 5'-AATGGCAACTCCTGCACCTC-3'
Region (+5) - 564 bp	5'-GTCAGGTTGTTGGCGTCATT-3' and 5'-GAAGGAATCTGCCGCATCCG-3'

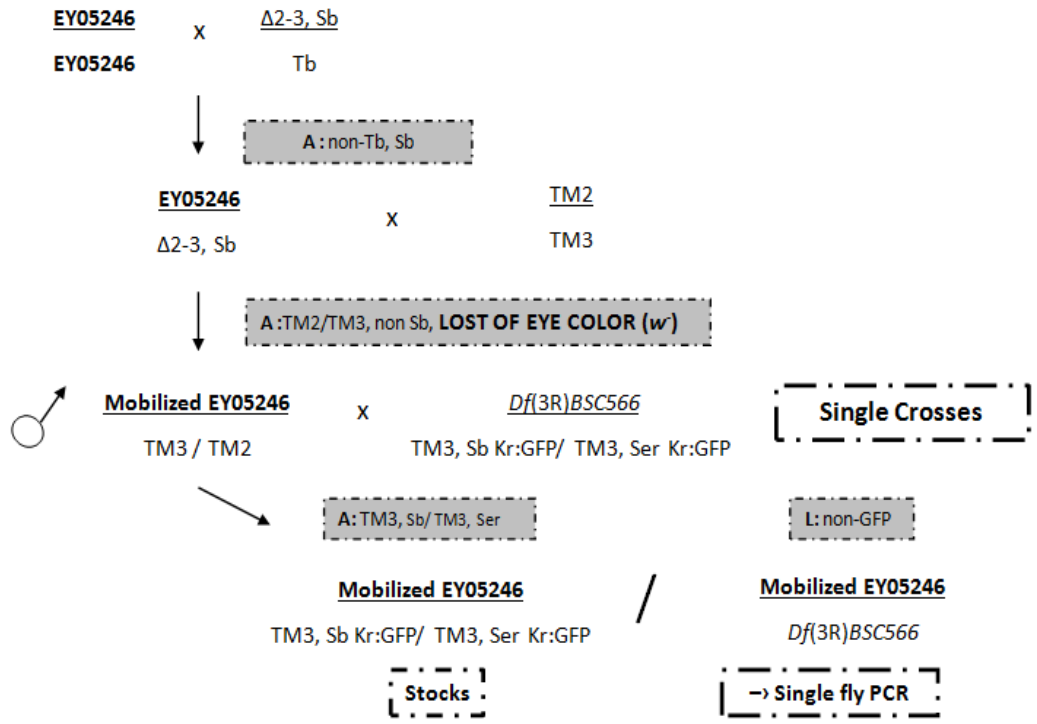

Fig. 3.1 Crossing scheme for the *P*-element imprecise excision screening.

Offsprings with desired genotypes were selected by genetic markers expressed at different developmental stages: adult (A) or larval (L) (highlighted in grey). Adult male flies with w^- eye color were selected as positive candidates and they were put in *trans* to a deficiency chromosome, *Df*(3R)*BSC566*. Single fly genomic PCR were performed to evaluate and map the potential *rim* candidates produced by the *P*-element imprecise excision screening.

3.4.3 *Minos* element mobilisation screen

In an attempt to induce precise or imprecise excision deletions in the nearby genomic sequences adjacent to the TA of the *Minos* insertion, a remobilization screen of a single *Minos* insertion (Mi{ET1}MB02027) was carried out (details see Introduction section 2.4.3). In this thesis, we are reporting our strategy and the result of the *Minos* element mobilization screen of the gene of interest. The *Minos* transposon that inserted between the 6th and 7th exon of the *drbp* locus was crossed with a fly strain carrying the heat-activated transposase (pPhsILMiT construct, MIT in short in Fig. 3.2) on the second chromosome. The jump-start males were heat-shocked daily at 37 °C for 1 hr during the larval and pupal stages to induce the *Minos*-element mobilization. Adult flies progeny of the cross between the *Minos*-element and the transposase line (loss of GFP-tag, see Fig. 3.2) were tested for imprecise and precise excision events via single fly genomic PCR.

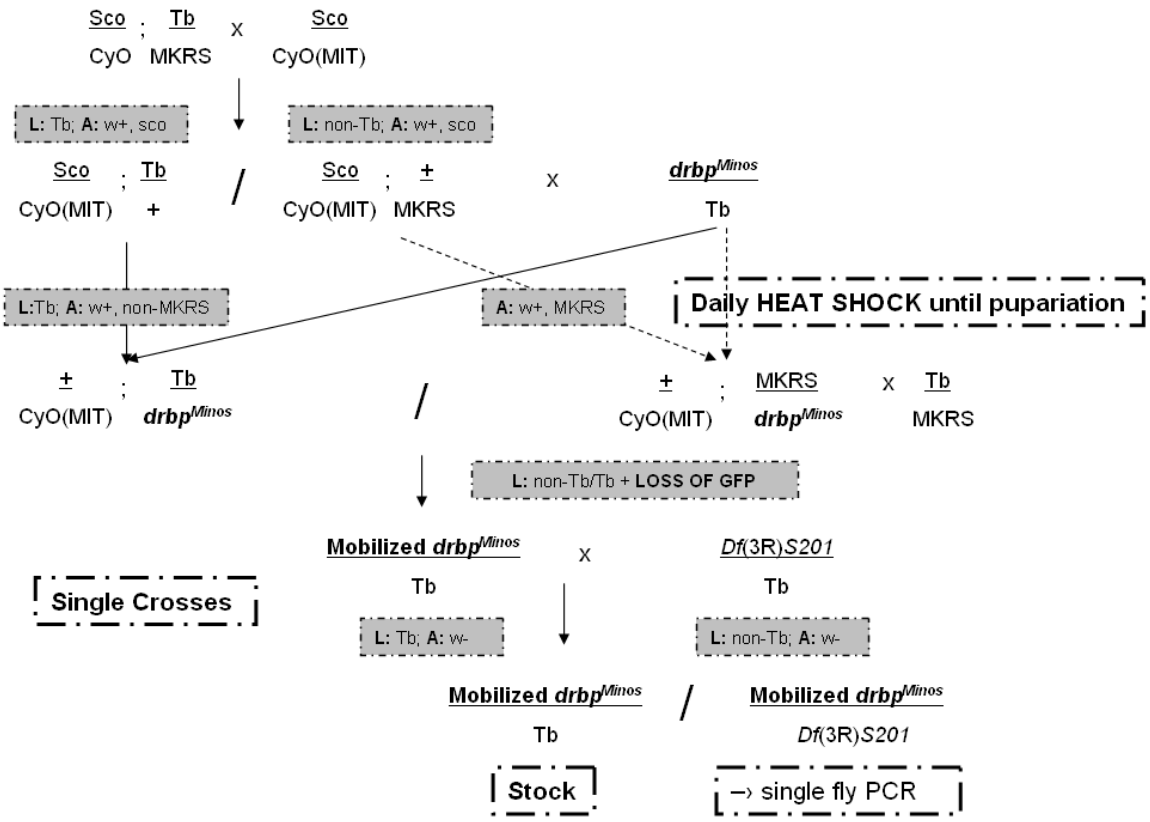

Fig. 3.2 Crossing scheme for the *Minos* element mobilization screening.

Offsprings with desired genotypes were selected by genetic markers expressed at different developmental stages: adult (A) or larval (L) (highlighted in grey). Adult flies with the loss of 3xEGFP construct were selected as positive candidates and they were put in *trans* to a deficiency chromosome, *Df*(3R)*S201*. Single fly genomic PCR were performed to evaluate the potential intragenic *drbp* alleles produced by the mobilization screening.

Primer pairs were used for checking the mobilization of up- and downstream region of the *Minos* insertion:

Region Up(-1) - 507 bp	5'-GGCCAGCACCAGCTTGAG-3' and 5'-ATATGCTATATGGCTAGGCT-3'
Region Down(+1) - 666 bp	5'-TAGCATATATAGCGACCA-3' and 5'-TTCGGCTGGTCATGAGTG-3'

3.5 P[acman]: A bacterial artificial chromosome (BAC) transgenic platform

PhiC31-mediated transgenesis offers site-specific integration of large DNA fragments at specific docking sites in the *Drosophila* genome, based on homologous recombination. It permits direct comparison of differently mutagenized DNA fragments integrated at the same target site. In this thesis, we generated *rim* and *drbp* genomic rescue constructs, based on the BAC transgenic platform (details see Introduction section 2.5 and Venken et al., 2006).

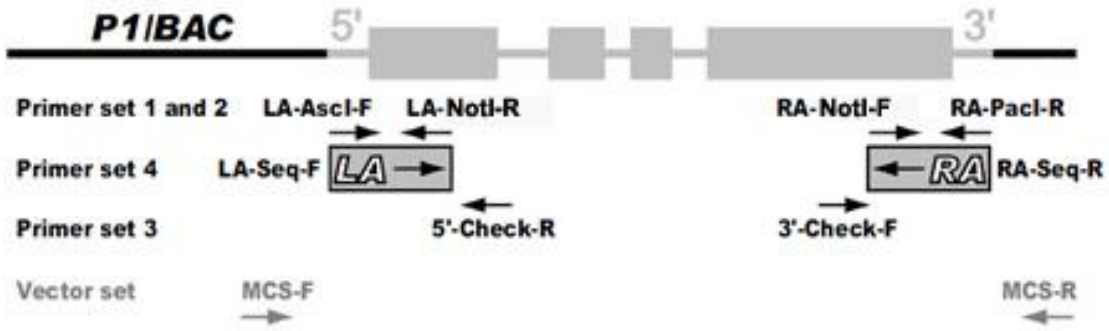

Fig. 3.3 Multiple cloning site of P[acman] and primer design for gap-repair of P[acman].

"A desired genomic fragment (grey), consisting of exons (boxes) and introns (lines), is contained within a genomic clone, P1 bacteriophage or BAC. Four primer sets are designed for the DNA fragment to be retrieved. Primer sets 1 and 2, incorporating appropriate restriction sites for cloning, are used to PCR amplify 500 bp homology arms, a left arm (LA) and a right arm (RA). Primer set 3 (5'-Check-R and 3'-Check-F) is used with vector specific primers (MCS-F and MCS-R) to screen by PCR for correct recombination at the left end (MCS-F and 5'-check-R) and the right end (3'-Check-F and MCS-R). Primer set 4 (LA-Seq-F and RA-Seq-R) is used to sequence across the junctions to confirm correct retrieval of the desired fragment)" (taken from Venken et al., 2006).

Common primers used were listed here:

MCS-F	5'-TTTAAACCTCGAGCGGTCCGTTATC-3'
MCS-R	5'-CTAAAGGGAACAAAAGCTGGGTAC-3'
attP-F	5'-CTTCACGTTTTCCCAGGTCAGAAG-3'
attP-R	5'-GTCGCGCTCGCGCGACTGACGGTC-3'
attB-F	5'-GTCGACGATGTAGGTCACGGTC-3'
attB-R	5'-TCGACATGCCCGCCGTGACCGTC-3'
MCS-Cloning-F	5'-CGGGATCCGCTAGCAAAAAAACCGGTGTAAAACGACGGCCAGTGAG-3'
MCS-Cloning-R	5'-CGGGATCCACTAGTAAAAAAATGCATAAAAAAGAATTCGGAAACAGCTATGACCATG-3'

The presence of *attL* was checked by using primer pair attB-F and attP-R; the presence of *attR* was checked by using primer pair attP-F and attB-R (see Introduction section 2.5).

3.5.1 *rim* genomic rescue construct

BAC clone BACR45M04 (RP98-45M4) (genomic region 13,575,585 - 13,747,153), obtained from RPCI-98 library of BACPAC Resource Center (BPRC) was used as template for cloning and recombination events.

Left homology arm (LA) flanked by AscI-NotI was produced by PCR primers:

5′-AGACGGCGCGCCGCTGAGGCTTCCTCAATGAT-3′ and

5′-AGTCGCGGCCGGAGCCAGAGTCGGAAGAGAA-3′;

Right homology arm (RA) flanked by NotI-PacI was produced by primers:

5′-AGTCGCGGCCGCAAGGACTGCGCTCTCGTTGG-3′ and

5′- AGACTTAATTAAAAGGTTACGCCCATTATCCC-3′.

The PCR products of LA and RA were cut by NotI and ligated to produce LARA. LARA was cut and ligated into attB-P[acman]-ApR vector using AscI-PacI. Recombination event between the BAC and attB-P[acman]-LARA-ApR entailing the complete *rim* locus (genomic region 13,697,805 - 13,747,020) was completed as previously described (Venken et al., 2006).

3.5.2 *drbp* genomic rescue construct

BAC clone CH321-59F24 (genomic region 11,161,593 - 11,262,853), obtained from CHORI-321 library of BACPAC Resource Center (BPRC) was used as template for cloning and recombination events.

Left homology arm (LA) flanked by AscI-NotI was produced by PCR primers:

5′-AGACGGCGCGCCAGGCGGCAGGTCCTTCAGAT-3′ and

5′-AGTCGCGGCCGCATCCTCGAGAGTGGCATTGA-3′;

Right homology arm (RA) flanked by NotI-PacI was produced by primers:

5′-AGTCGCGGCCGCTGCGACAGTAGCTAGCAAGA-3′ and

5′- AGACTTAATTAACTGCAATTCTGCGCCGACAA-3′.

The PCR products of LA and RA were cut by NotI and ligated to produce LARA. LARA was cut and ligated into attB-P[acman]-ApR vector using AscI-PacI. Recombination event between the BAC and attB-P[acman]-LARA-ApR entailing the complete *drbp* locus (genomic region 11,193,728 - 11,230,728) was completed as previously described (Venken et al., 2006).

3.6 Immunostainings of adult *Drosophila* central nervous system (CNS)

Brain stainings were essentially performed as described previously (Wu and Luo, 2006). Brains were dissected in HL3 (70 mM NaCl, 5 KCl, 20 mM $MgCl_2$, 10 mM $NaHCO_3$, 5 mM trehalose, 115 mM sucrose and 5 mM HEPES; pH adjusted to 7.2 at room temperature (Stewart et al., 1994)) on ice and immediately fixed in cold 4 % 0.1 mM phosphate buffered saline (PBS) (8 g NaCl, 2 g KCl, 2 g KH_2PO_4, 1.15 g Na_2HPO_4 x $2H_2O$, add 1 L H_2O, pH 7.4) for 20 mins at RT. The brains were then incubated in 1 % PBT for 20 mins and preincubated in 0.3 % PBT with 10 % NGS for 3 hrs at RT. For primary antibody treatment, samples were incubated in 0.3 % PBT containing 5 % NGS and the primary antibodies for 2 days at RT. After primary antibody incubation, brains were washed in 0.3 % PBT for 4× for 30 mins at RT, then overnight at 4 °C. All samples were then incubated in 0.3 % PBT with 5 % NGS containing the secondary antibodies for 1 day at RT. Brains were washed for 4× for 30 mins at RT, then overnight at 4 °C. Adult brains are mounted in Vectashield overnight before

confocal scanning (Vector Laboratories). Antibody dilutions used for adult CNS staining were: mouse monoclonal Nc82 anti-BRP$^{C\text{-}Term}$ antibody 1:100; rabbit anti-RBP$^{N\text{-}Term}$ antibody 1:1500; rabbit anti-RBP$^{C\text{-}Term}$ antibody 1:800; mouse monoclonal 3E6 anti-GFP antibody 1:500; chicken monoclonal anti-GFP antibody 1:1500. Confocal secondary antibodies concentrations were: goat anti-rabbit-Cy3 1:400; goat anti-mouse Alexa Fluor-488 1:400; goat anti-mouse Cy5 1:400; goat anti-chicken Alexa Fluor-488.

3.7 Image acquisition and analysis

For the adult CNS, image acquisition and processing was performed as previously described (Christiansen et al., 2011). Conventional confocal images were acquired with a Leica TCS SP5 confocal microscope (Leica Microsystems) using a 20×, 0.7 NA oil objective for whole-brain imaging with a voxel size of 327 × 327 × 200 nm. A 63×, 1.4 NA oil objective was used for calyx or antennal lobes scans, using a voxel size of 90 × 90 × 30 nm. Confocal stacks were processed using ImageJ software (http://rsbweb.nih.gov/ij/). The magnified images (AZ spots) were smoothened (3-4 Pixel Sigma radius) using the Gaussian blur function in the ImageJ software.

Segmentation of 3D image stacks of the central body region of brains was done using Amira® software, Visage Imaging GmbH. The first step was to separate the object of interest (central brain region) from the background (part of optical lobes on both hemispheres). A unique label was defined for each region in the first fluorescence channel (e.g. Nc82). This was done by manually assigning the central brain region to interior regions on the basis of the voxel values (volumetric pixels, see example in Fig. 3.4). By this procedure, each voxel value outside the central brain region was excluded from the interior label (i.e. the area belonging to the central brain region of each focal plane was included for later measurements). A full statistical analysis of the image data associated with the segmented materials was obtained by applying MaterialStatistics module of the Amira® software, in which the mean gray values of the interior region (central brain region) is calculated. The voxel value of the second fluorescence channel (DRBP$^{C\text{-}Term}$) was also obtained by applying the same mask/ label already defined for the first channel. The mean voxel values of the central brain regions were compared, as measured in individual adult brains, in order to evaluate the synaptic marker label (Fig. 4.17).

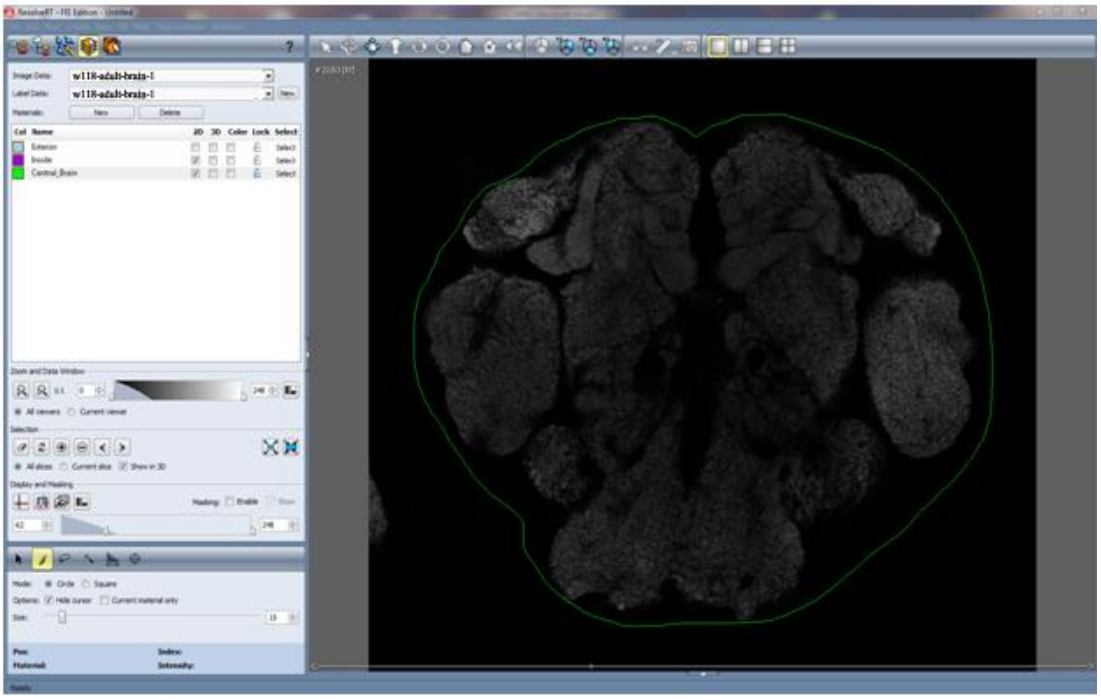

Fig. 3.4 An example of the label/mask manually defined in the Amira® software.

A unique label was defined for each region in the first fluorescence channel (e.g. Nc82) by manually assigning the central brain region to interior regions (area in the green circle). The area belonging to the central brain region of each focal plane was included for later measurements.

3.8 Adult vitality

The effect of the loss of function in RIM and DRBP were addressed by adult hatching rates. *rim* alleles were placed in *trans* to the deficiency chromosome, *Df*(3R)*ED5785*. *drbp* alleles were placed in *trans* to the deficiency strain, *Df*(3R)*S201*. The number of hatched progeny from two independent crosses was counted. The adult hatching rates of the intragenic alleles (in *trans* to *Df*) was compared to the expected Mendelian ratio (33.3 %) in the wild-type situation.

3.9 Behavioral assays

Adult locomotive analysis was performed based on previous reports (Wagh et al., 2006; Owald et al., 2010). Male animals were collected on the day of eclosion and tested within 72 hrs. On the day of assay, flies were anesthetized on ice and wings were clipped. Individual animal with clipped wings was kept in an empty food vial and adapt to darkness for at least 2 hrs before testing. Experiments were performed under a red light and the locomotive performance of each fly was tested. For the negative geotaxis, the maximum height (10 cm) was recorded that the tested fly reached within 30 s after tapping the fly to the bottom of the scaled vial. To test the walking ability, flies were placed in the center of a 145 mm diameter

Petri dish with a 2 × 2 cm grid. The number of grid lines crossed within a period of 30 s was recorded. 15 individual adults were tested thrice (n = 15).

Locomotion assay of *drbp* mutant larvae was performed by measuring number of contractile motions of the larva in a 30 s interval. Third instar larvae of each genotype were put on an agarose plate pre-warmed at 25 °C and number of contractile motions of 15 individual larvae were counted thrice (n = 15).

3.10 Statistical analysis

The nonparametric Mann-Whitney rank sum test was used for statistical analysis of all linear independent data groups (Prism; GraphPad Software, Inc.). The data are reported as mean ± SEM, n indicates the sample number, and p denotes the significance: * $p<0.05$, ** $p<0.01$, ***$p<0.001$. Linear and non-linear (Gaussian fit) regression was used to determine significant data correlation.

4. Results

4.1 Rab3 Interacting Molecule (RIM): a central active zone cytomatrix component

Current available tools in *Drosophila* studies provided us with higher resolution in understanding mechanistic roles of presynaptic proteins in AZs. Ca^{2+}-channels are pivotal for SV fusion at slots near the AZ cytomatrix (Kittel et al., 2006; Fouquet et al., 2009). Apart from Ca^{2+}-channels and the BRP matrix, we are interested in mechanistically studying additional AZ cytomatrix proteins. Rab3 Interacting Molecules (RIMs) are evolutionarily conserved scaffolding proteins that are localized at AZs (Wang et al., 1997; Wang et al., 2000; Kaeser et al., 2011; Han et al., 2011). They have been suggested to tether Ca^{2+} channels to the AZ membrane via a direct interaction to the Ca^{2+} channel α1 subunit (Wang et al., 2000) and via an indirect interaction with RIM binding proteins (Kaeser et al., 2011). In fact, studies in mammals have shown important synaptic roles for RIMs in SV docking and priming (Kaeser et al., 2011). We were interested to study which functional role RIM might play at the *Drosophila* NMJ.

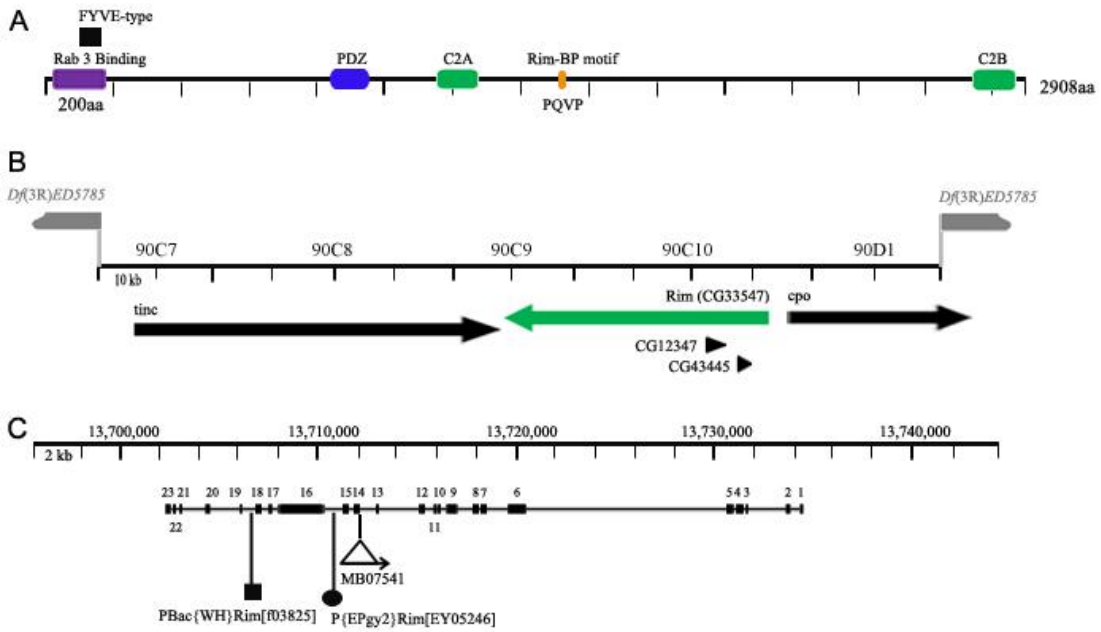

Fig. 4.1 Schematic representation of the *rim* locus.

(A) RIM entails an N-terminal zinc finger domain, a PDZ domain, and two C-terminal C2 domains (C2A, C2B), based on FlyBase CG33547-PB, 2908 aa. (B) Genomic organization of the *rim* (CG33547) locus. A subset of annotated genes in the chromosomal region 90C7-D1 is illustrated. The breakpoints of *Df*(3R)*ED5785* (gray bars) is shown. (C) Gene model of *rim*. Based on FlyBase CG33547-PB, *rim* encompasses 23 exons. The position and orientation of *Minos* element Mi{ET1}MB07541 insertion (rim^{Minos}) are depicted. Position of transposons insertion in the *rim* locus (PBac{WH}Rim[f03825] and P{EPgy2}Rim[EY05246]) that have been used to create mutant alleles are also illustrated.

Genetic analysis of RIM family proteins in *Drosophila* was not yet reported, thus it is an interesting target for our studies. *Drosophila* is predicted to encode a single *rim* gene (Wang and Südhof, 2003). The FlyBase consortium suggests the existence of up to 13 isoforms. Detailed genomic organization of the *rim* locus (CG33547) is illustrated in Fig. 4.1B-C. The locus covers several annotated genes spanning the chromosomal region 90C7-D1. We refer to the longest RIM isoform PB in our studies, with the predicted coding DNA sequence (CDS) of *rim* being 2908 aa long and encompassing 23 exons. RIM entails an N-terminal zinc finger domain, a PDZ domain, and two C-terminal C2 domains (C2A, C2B) (Fig. 4.1A).

4.2 RIM is specifically expressed in the nervous system

We first wanted to investigate the spatio-temporal expression pattern of *rim* by *in situ* hybridizations of *Drosophila* embryos. The result revealed a strong, specific label of *rim* in the central nervous system (CNS) (Fig. 4.2). The onset of *rim* mRNA expression corresponds to the onset of neuronal differentiation and axon outgrowth (Broadie and Bate, 1993). Thus, the *rim* mRNA appears specifically expressed in postmitotic neurons.

Fig. 4.2 *In situ* hybridization of *rim* in *Drosophila* embryos.

Specific staining was obtained when an antisense probe of *rim* cDNA is used. No labeling of sense probes was observed. *Drosophila rim* was specifically expressed in the CNS and ventral chord throughout embryo genesis (not shown). a, b and c indicated different views of an embryo probed with antisense *rim* cDNA.

4.3 Generating *rim* alleles for molecular and genetic analysis of RIM

We next wanted to create loss of function alleles for *rim* in our studies. Thus, we subjected *rim* to genetic analysis and several attempts were carried out to create intragenic deletion mutants. In Fig. 4.1C, the insertion positions of the available transposon alleles of the *rim* locus that have been used in our analysis are depicted. A deficiency strain spanning the locus of *rim* and neighboring genes, *Df*(3R)*ED5785* (Fig. 4.1B; breakpoints see Material and Methods section 3.4) was used in this study as well. Position of other transposon insertions in the *rim* locus (PBac{WH}Rim[f03825] and P{EPgy2}Rim[EY05246]) that had been used to create deletion mutant alleles are also shown (Fig. 4.1C).

4.3.1 Identification of *rim* deletion alleles by FLP-FRT recombination deletion screening

We performed *piggyBac* element deletion mutation screenings to establish *rim*-specific mutant situations by *trans* allelic combinations. One transposon insertion residing in the *rim* locus (PBac{WH}Rim[f03825] was used for FLP-FRT recombination deletion screenings (Fig. 4.1C, 4.3A, hereafter P2). Downstream, a *piggyBac* element residing in the *tinc* locus, PBac{WH}tinc[f01062], was chosen (Fig. 4.3A, left) as the parental line (P1) for the $rim^{ex1.26}$ screening. Upstream *piggyBac* element PBac{WH} cpo[f01629] inserted in the *cpo* locus was used (Fig. 4.3A, right) as the parental line (P1) for the $rim^{ex2.40}$ screening.

Both parental pairs used for FLP-FRT recombination deletion screenings mentioned bear *WH* FRT sites (see Introduction section 2.4.1). Heat shock–activate FLP recombinase (*hs-FLP*) at 37 °C promotes *trans*-recombination between FRT elements. Deletions can initially be detected in the progeny by a gain of the w^+ transgene in deletion screens for both $rim^{ex1.26}$ and $rim^{ex2.40}$. Five candidates out of 65 w^+ progeny lines for $rim^{ex1.26}$ and only one candidate out of 65 w^+ progeny lines for $rim^{ex2.40}$ were shortlisted for further two-sided PCR screenings. This was to further confirm the presence of residual FRT element from both parental lines. PCR primers were designed by using transposon-specific primers facing outward and genome-specific primers (details in Material and Methods section 3.4.1). For $rim^{ex1.26}$, two-sided PCR indicated the presence of parental transposons 1 (P1) (Fig. 4.3B(I)) and parental line 2 (P2) (Fig. 4.3B(II)); two-sided PCR for $rim^{ex2.40}$ indicated the presence of both P1 (Fig. 4.3C(I)) and P2 (Fig. 4.3C(II)). After validation of the presence of both parental lines by two-sided PCR, we wanted to confirm chromosomal deletions of the genomic region spanning between the parent lines. $rim^{ex1.26}$ and $rim^{ex2.40}$ were placed in *trans* to the *rim* deficiency, *Df*(3R)*ED5785*. A primer pair was designed to amplify the genomic region in between two parental elements. $rim^{ex1.26}$ adult animals were viable when they were placed in *trans* to the *Df* but were embryonic lethal in the case of $rim^{ex2.40}$. Embryo progeny of $rim^{ex2.40}/Df$ were used as the genetic material for the singly fly PCR. The absence of genomic amplification for $rim^{ex1.26}$ (Product size: 667 bp) and $rim^{ex2.40}$ (Product size: 748 bp) (Fig. 4.3B(III) and 4.3C(III)) was revealed in single flies genomic PCRs. Both alleles, $rim^{ex1.26}$ and $rim^{ex2.40}$ lacked the genomic region spanning between the parental lines (Fig. 4.3B(III) and 4.3C(III)).

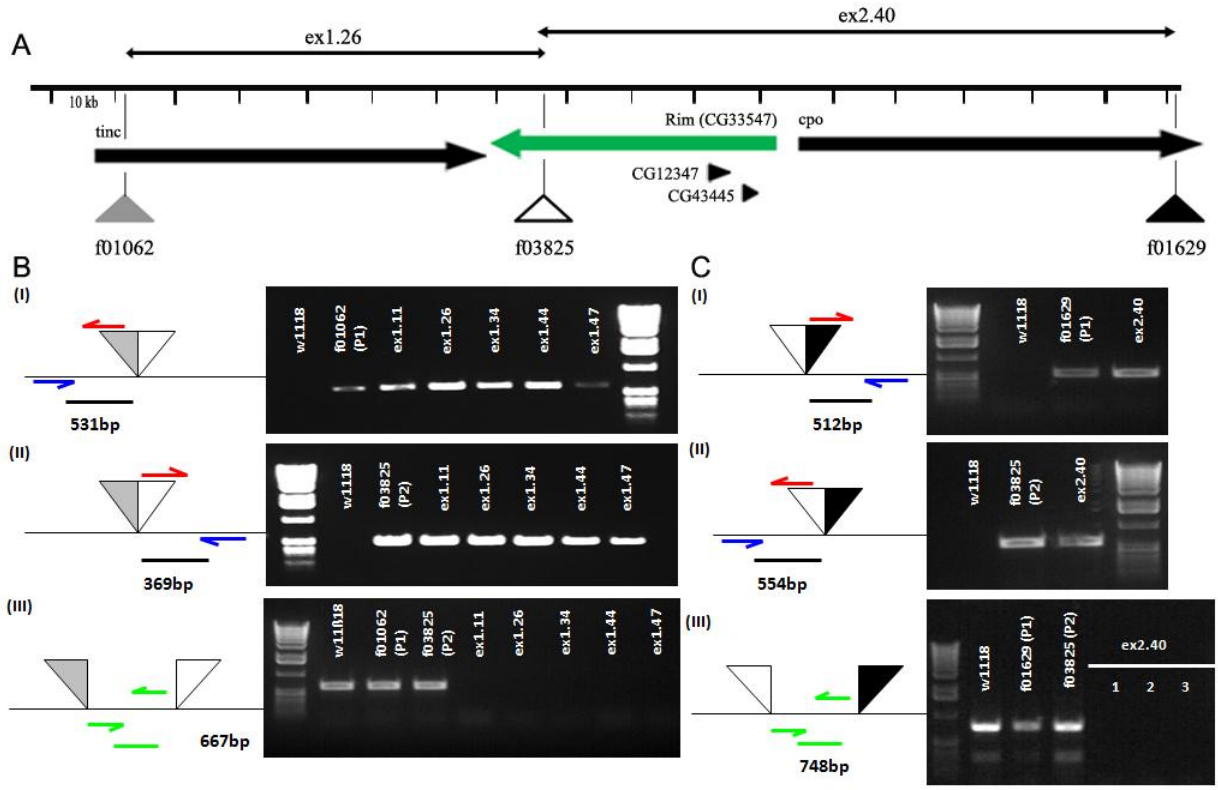

Fig. 4.3 Production of *rim*$^{ex1.26}$ and *rim*$^{ex2.40}$ by FLP-FRT recombination.

(A) Parental *piggyBac* transposon lines PBac{WH}tinc[f01062] (gray triangle) and PBac{WH}Rim[f03825] (white triangle) are chosen to create *rim*$^{ex1.26}$. Parental *piggyBac* transposon lines PBac{WH} cpo[f01629] (black triangle) and PBac{WH}Rim[f03825] (white triangle) are chosen to create *rim*$^{ex2.40}$. Position of insertion are depicted. (B) (I) Screening of positive candidates by the gain of eye color in deletion generation and confirmed with the presence of hybrid products of each parental line. An amplicon of 531 bp (presence of P1-f01062) and (II) an amplicon of 369 bp (presence of P2-f03825) are detected by RT-PCR. (III) Adult progeny of potential deletion mutant lines crossed over deficiency stock (*Df*(3R)*ED5785*) are subjected to further PCR to confirm the deletion of genomic region. Primer pair was designed to amplify genomic region in between two parental elements and the absence of amplicon indicated the removal of genomic sequence spanning P1 and P2. (C) (I) Screening of positive candidates by the gain of eye color in deletion generation and confirmed with the presence of hybrid products of an amplicon of 512 bp (presence of P1-f01629) and (II) an amplicon of 554 bp (presence of P2-f03825) by RT-PCR (III) Primer pair was designed to amplify genomic region between P1 and P2 elements, using embryo progeny of genotype *rim*$^{ex2.40}$ placed in *trans* to the *Df*(3R)*ED5785* deficiency as the testing material. The absence of amplicon indicated the removal of genomic sequence in the *rim*$^{ex2.40}$ FLP-FRT recombination.

The *rim*$^{ex1.26}$ deficiency removes 60.785 kb of genomic region spanning P1 and P2. Based on the CG33547-PB isoform (2908 aa), this deficiency covers the C-terminus C2B domain coding region of the *rim* locus and the complete coding region of the downstream gene *tinc*. *rim*$^{ex2.40}$ deletes 95.824 kb of genomic region between P1 and P2, including an N-terminal region of RIM that entails the N-terminal Rab3 binding, zinc-finger domain, a PDZ domain, and the first C-terminal C2 domains (C2A). It also partially deletes the N-terminal coding region of an upstream gene, couch potato (*cpo*). This made the characterization of the loss of function in the allele *rim*$^{ex2.40}$ difficult because *cpo* was reported to play essential role in the CNS (Bellen et al., 1992). We then tested vitality for the retrieved *rim* mutant alleles by

positioning *rim*$^{ex1.26}$/*rim*$^{ex2.40}$ in *trans*. However, adult locomotive behavior of *rim*$^{ex1.26}$ /*rim*$^{ex2.40}$ (result not shown) did not show any difference to the condition when *rim*$^{ex1.26}$ was in *trans* to *Df* (Fig. 4.8). We conclude that *rim*$^{ex1.26}$ allele may not be essential to represent the phenotype of *rim*.

4.3.2 Retrieval of *rim* deletion alleles by *P*-element mobilization screen

Next we wanted to generate intragenic deletion mutants for the *rim* locus by the *P*-element mobilization screening. Imprecise excision events occur randomly by mobilization of the *P*-elements from its original insertion site resulting in removing random parts of the adjacent genomic regions. A deletion screen searching for imprecise mobilization of *P*-elements, P{EPgy2}Rim[EY05246] was carried out by crossing in a transposase expressing chromosome strain (delta 2-3). Mobilization of *P*-elements in potential mutant candidates was detected by a loss of eye color (w^-) upon activation of transposase. 250 candidates with loss of eye color (w^-) from the *P*-element mobilization screen were sorted out and 250 single crosses (placed in *trans* to *Df*) were set up for subsequent PCR verifications and genetic mappings (see Introduction section 2.4.2; Material and Methods section 3.4.2).

Candidate chromosomes from imprecise excision screening were mapped by using genomic primer pairs designed to amplify regions adjacent, either upstream (region -1 to -5) (Fig. 4.5A) or downstream (region +1 to +4) (Fig. 4.4A) to the parental transposon insertion site. DNA extracted from adult progeny of 250 potential *rim* alleles (in *trans* to *Df*) were used as genetic material for single fly PCR screening. Two new *rim* alleles, *rim*^{del71} and *rim*^{del103} with longer upstream intragenic deletions (compared to other shortlisted candidates tested, see also Fig. 4.5B) were identified. We systematically checked for regions not allowing for amplification and mapped the breakpoint position of both *rim*^{del71} and *rim*^{del103} downstream (Fig. 4.4B, C) to the original parental transposon site. We then screened for the absence of genomic template upstream of the original parental insertion site (Fig. 4.5B). We detected a different upstream breakpoint position for *rim*^{del71} and *rim*^{del103} (Fig. 4.5C and D). Using primer pair (-4) amplification was observed for *rim*^{del53}/*Df* and *rim*^{del71}/*Df* but not for the *rim*^{del103}/*Df* (Fig. 4.5B).

Of note, the newly gained *rim* alleles (*rim*^{del71} and *rim*^{del103}) placed in *trans* to *Df* showed a reduced ratio of adult animals hatching (Table 4.1) as well as deficits in adult locomotive ability (Fig. 4.8).

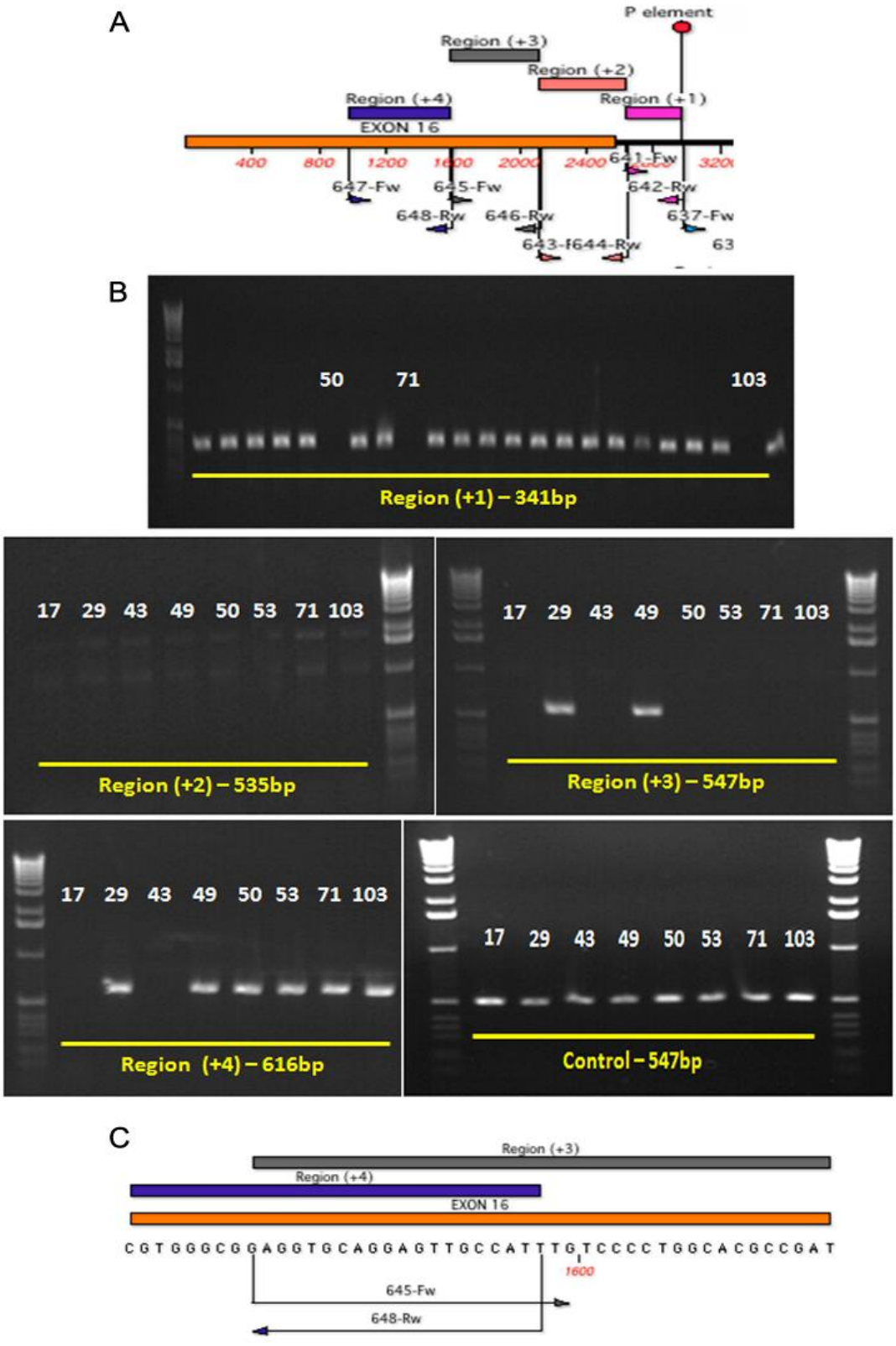

Fig. 4.4 Schematic representation of the downstream region for mapping the *P*-element imprecise excision screen in creating *rim*^{del71} and *rim*^{del103}.

(A) Primer pairs designed to screen for the imprecise excision of the *P*-element, of regions (+1 to +4) downstream to the transposon insertion site. (B) PCR result showing potential candidates (w^-) by checking for the mobilization of downstream regions (+1 to +4). (C) The diagram depicts the same breakpoint position of *rim*^{del71} and *rim*^{del103} downstream. (D) Internal control experiment indicated the presence of DNA sample/ template for the screen PCRs performed.

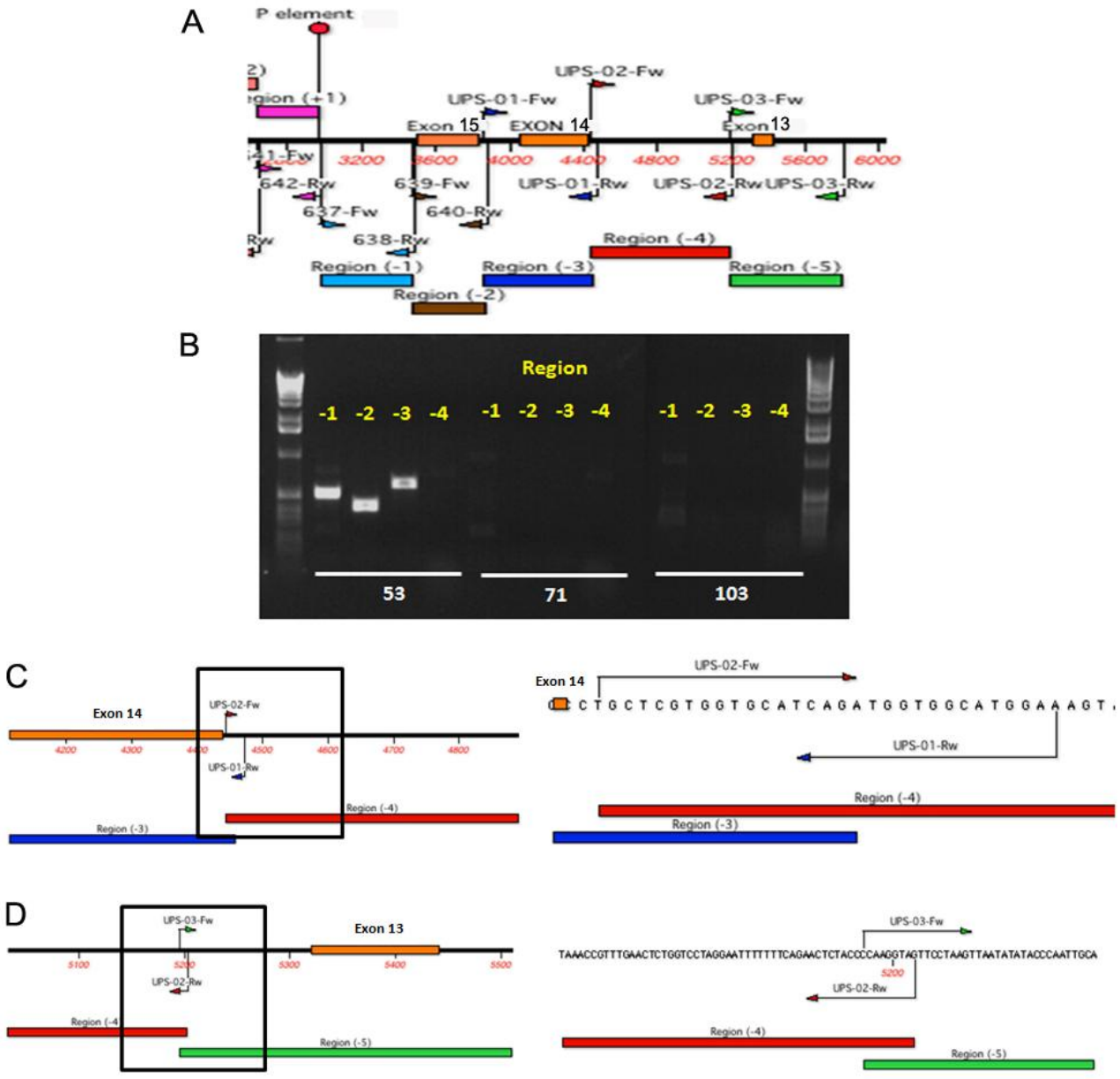

Fig. 4.5 Mapping the upstream region of alleles *rim*^{del71} and *rim*^{del103}.
(A) Primer pairs designed to screen for the imprecise excision of the *P*-element, of regions (-1 to -5) upstream to the transposon insertion site. (B) PCR result showing potential candidates (w^-) by checking for the absence of upstream regions (-1 to -4) (C) Schematic diagram depicted the breakpoint of *rim*^{del71} and (D) *rim*^{del103} upstream region.

The first (*rim*^{del71}) and second allele (*rim*^{del103}) represent small internal deletions that remove the majority of three common exons (exon 14 -16) in the *rim* gene. According to the isoform PB, 47.59 % of the original predicted peptide sequence of RIM could still be translated in both *rim*^{del71} and *rim*^{del103} (Fig. 4.6B). An additional deletion of 744 bp genomic sequence upstream of exon 14 was detected in *rim*^{del103} (Fig. 4.5D, absence of region -4). In the truncated protein product, the C2B domain close to the C-terminus and the conserved PXXP motif that was proposed to bind RIM-binding protein (DRBP) are absent (Fig. 4.6B, CG33547-PB isoform) (summary diagram in Fig. 4.6A). The biochemical interaction between

PXXP motifs of RIM and the third SH3 domain of DRBP was later confirmed by a Yeast-2-Hybrid experiment (Fig. S7 in Liu et al., 2011). Taken together, we successfully identified two intragenic deletion alleles in the rim locus (*rim*^{del71} and *rim*^{del103}) by the *P*-element mobilization screening.

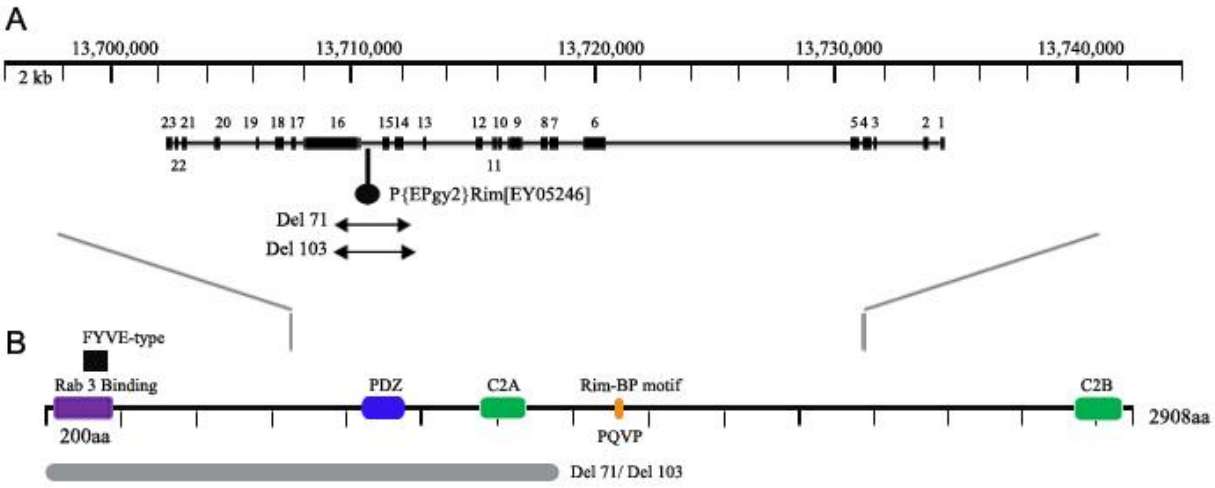

Fig. 4.6 Summary of *P*-element imprecise excision screening.

(A) Parental transposon element P{EPgy2}Rim[EY05246] (insertion position: 13,710,797), 393 bp upstream of exon 16 was used to create mutant alleles. Breakpoints of *rim*^{del71} and *rim*^{del103}created in the *P*-element excision screen are depicted and (B) predicted translation products (gray) of *rim*^{del71} and *rim*^{del103} are illustrated.

4.3.3 *Minos* element as a hypomorphic *rim* allele

While the excision screen was ongoing, another transposon insertion strain in the *rim* locus (Mi{ET1}MB07541, henceforth called *rim*^{Minos}; Fig. 4.1C) became available via FlyBase. Animals carrying this allele, *rim*^{Minos} over *Df* hatched slightly below (10 % less) expected Mendelian ratio (Table 4.1) and mutant adults show a deficit in adult locomotive behavior (Fig. 4.8). Thus, this transposon insertion was considered as a candidate for the loss of function assay because it resides within a coding exon in the *rim* locus.

4.4 Production of genetic tools

4.4.1 A Genomic rescue construct for *rim*

The *Drosophila rim* locus spans more than 40 kb. The predicted full length cDNA of *rim* isoform PB encodes a protein of 2908 aa. Due to the lack of complete cDNA clones available, we employed the P[acman] technology to clone the genomic region entailing the entire *rim* locus. In brief, left and right homology arm (LA and RA) located at either end of the targeted *rim* locus were cloned and ligated into the multiple cloning site of the *attB*-P[acman]-Ap^{R}

vector (see Material and Methods section 3.5.1 for details). BAC clone (BACR45M04) harboring the *rim* locus was first transformed into a recombineering-competent *E. coli* strain. Later transformation of the linearized *attB*-P[acman]-*rim* construct into the recombineering-competent *E. coli* strain enabled subsequent recombineering. We successfully produced a *rim* rescue genomic transgene harboring 48.954 kb (3R:13,697,805 - 13,747,020) of the genomic region based on the BAC transgenic platform (Rescue, see Fig. 4.7, blue block; successful integration event in flies, not shown). Evaluation of the efficacy of this rescue transgene, however, was challenging because of the absence of *rim* null alleles and the weak phenotypes of the available *rim* alleles, which were characterized by only partially reduced adult vitality (Table 4.1) and locomotion activity were detectable (Fig. 4.8).

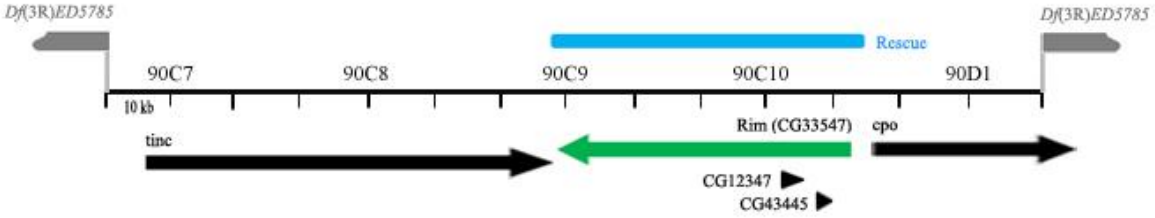

Fig. 4.7 Production of *rim* genomic rescue construct based on P[acman] transgenesis.
Position of the *rim* genomic rescue construct was depicted in blue block. *rim* genomic rescue covered a total of 48.954 kb (3R:13,697,805 - 13,747,020) DNA genomic fragments that entailed the entire *rim* locus.

4.4.2 Production of N- and C-Term antibodies against RIM

In this thesis, we tried to raise N- and C-Term specific peptide antibodies against RIM (epitopes see Material and Methods section 3.3) but we were unsure of the specificity. Only very weak staining in peripheral synapses NMJ or synaptic-like staining in the larval CNS was detected (data not shown). The weak antibody label of RIM did not co-localize with BRP and was not down-regulated in any of the RIM excision mutants at the NMJ.

4.5 Characterization of RIM mutants

4.5.1 Adult RIM mutants hatched at a lower rate

We first evaluated the effect of the loss of function in RIM mutants by measuring the rate of adult animals hatching. The *rim* deletion alleles $rim^{ex1.26}$, rim^{del71}, rim^{del103} as well as the rim^{Minos} allele were placed in *trans* to deficiency strain, *Df*(3R)*ED5785*. We did not subject the $rim^{ex2.40}$ allele to the adult vitality test as alleles of an upstream gene, *cpo* that was affected in the $rim^{ex2.40}$ mutant was reported to have second instar larval lethality (Bellen et al., 1992). The number of hatched progeny in two independent crosses was counted. All the *rim* deletion mutations (RIM mutants/*Df*) assayed were found to have lower adult vitality than the

expected 33.3 % Mendelian ratio (Table 4.1). By comparing to the normal wild-type adult, intragenic deletion alleles of *rim*: rim^{del71} (23.7 %), rim^{del103} (21.1 %) as well as rim^{Minos} (22.8 %) were showing similar adult hatching rate (Table 4.1). A similar reduction in adult hatching rate (9.2 %) was also observed in another $rim^{ex1.26}$ mutant, in which the second C2 domain of *rim* together with a downstream gene, *tinc* were removed (Table 4.1). This indicates the partial loss of RIM in the *rim* deletion mutations $rim^{ex1.26}$, rim^{del71}, rim^{del103} and hypomorphic rim^{Minos} allele is sufficient to affect adult vitality.

Table 4.1 Hatching rate of adult *rim* mutants.

Hypomorphic rim^{Minos} mutant flies and other alleles $rim^{ex1.26}$, rim^{del71} *and* rim^{del103} (represented by asterisk * in the table) were placed in *trans* to deficiency strain, *Df*(3R)*ED5785*. The number and the percentage of adult progeny (*rim* allele/*Df*) hatched in each cross were highlighted in grey. All *rim* mutant adults (*rim* allele/*Df*) hatched at least 9 % less than the expected Mendelian ratio of 33.3 %.

	First cross against *Df*(3R)*ED5785*				Second cross against *Df*(3R)*ED5785*					Average percentage of both crosses			
	w[1118]/w[1118]; +/+ ; */Df(3R)ED5785	w[1118]/w[1118]; +/+ ; Df(3R)ED5785 / TM2, GFP	w[1118]/w[1118]; +/+ ; */ TM2, GFP	w[1118]/w[1118]; +/+ ; MKRS/ TM2, GFP	w[1118]/w[1118]; +/+ ; */Df(3R)ED5785	w[1118]/w[1118]; +/+ ; Df(3R)ED5785 / TM2, GFP	w[1118]/w[1118]; +/+ ; */ TM2, GFP	w[1118]/w[1118]; +/+ ; MKRS/ TM2, GFP	Total number of hatched flies	w[1118]/w[1118]; +/+ ; */Df(3R)ED5785	w[1118]/w[1118]; +/+ ; Df(3R)ED5785 / TM2, GFP	w[1118]/w[1118]; +/+ ; */ TM2, GFP	w[1118]/w[1118]; +/+ ; MKRS/ TM2, GFP
$rim^{ex1.26}$	29	/	37	38	26	/	44	54	228	24.1%	/	35.5%	40.4%
rim^{del71}	22	42	43	/	28	37	39	/	211	23.7%	37.4%	38.9%	/
rim^{del103}	21	37	52	/	25	40	43	/	218	21.1%	43.6%	35.3%	/
rim^{Minos}	25	/	38	35	20	/	40	39	197	22.8%	/	39.6%	37.6%

4.5.2 Adult RIM mutants show locomotion deficits

We then subjected *rim* mutation alleles to an assay for adult locomotive behavior. The *rim* deletion alleles $rim^{ex1.26}$, rim^{del71}, rim^{del103} as well as rim^{Minos} were placed in *trans* to the deficiency. For assaying the walking ability, flies were placed in the center of a 145 mm diameter Petri dish and the number of grid lines crossed within a period of 30 s was recorded. The maximum height (10 cm) reached by the tested fly within 30 s after tapping the fly to the bottom of the scaled vial was recorded for the negative geotaxis assay. All of the *rim* mutation

alleles (RIM mutants/*Df*) tested showed deficits in their locomotive abilities on both the horizontal and vertical planes (Fig. 4.7). The *rim* mutant adults showed a stronger deficit in locomotive behavior on the horizontal plane (control (w^{1118}/*Df*): 24.98 ± 0.4; $rim^{ex1.26}$: 12.8 ± 0.4; rim^{del71}: 13.07 ± 0.3; rim^{del103}: 11.73 ± 0.3; rim^{Minos}: 13.04 ± 0.5; P<0.0001 compared to control, Mann-Whitney U test) than their locomotive abilities in the vertical plane (control: 9.64 ± 0.1; $rim^{ex1.26}$: 8.87 ± 0.2; rim^{del71}: 8.04 ± 0.2; rim^{del103}: 6.47 ± 0.3; rim^{Minos}: 5.98 ± 0.3; ns, P<0.01, P<0.0001 compared to control, Mann-Whitney U test) (Fig. 4.7). However, we could not attribute the resultant phenotype to any known pathway or mechanism, since complex downstream pathways might contribute to the observed deficit in movement. We can draw the conclusion that *rim* alleles used in this study display a surprisingly mild phenotype. Additional measurements are required to elucidate the underlying synaptic role of RIM.

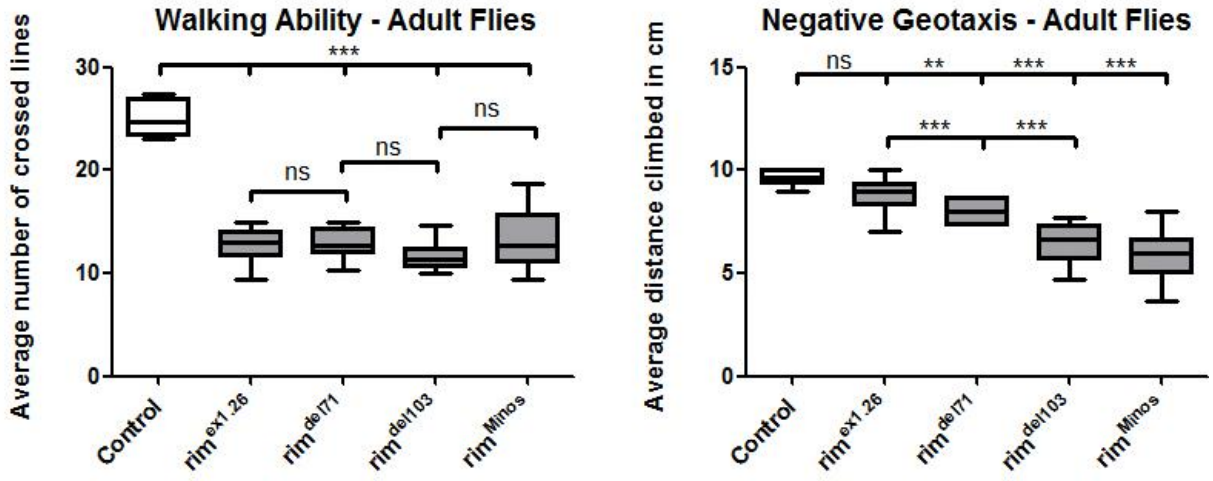

Fig. 4.8 Adult locomotion assay of *rim* alleles.
Adult locomotive behavioral assays were performed to evaluate adult *rim* mutant alleles according to Wagh et al., 2006 (3 times for each adult, n = 15 adult, details see Material and Methods section 3.9). *rim* mutant adults shown stronger deficit in locomotive behavior on a horizontal plane (control: 24.98 ± 0.4; $rim^{ex1.26}$: 12.8 ± 0.4; rim^{del71}: 13.07 ± 0.3; rim^{del103}: 11.73 ± 0.3; rim^{Minos}: 13.04 ± 0.5; P<0.0001 compared to control, Mann-Whitney U test) than their locomotive abilities in vertical plane (control: 9.64 ± 0.1; $rim^{ex1.26}$: 8.87 ± 0.2; rim^{del71}: 8.04 ± 0.2; rim^{del103}: 6.47 ± 0.3; rim^{Minos}: 5.98 ± 0.3; ns, P<0.01, P<0.0001 compared to control, Mann-Whitney U test).

4.5.3 RIM's role in homeostatic plasticity at the NMJ

To further characterize whether RIM protein is playing a crucial role in certain deficits, the rim^{del103} hypomorph was subjected to electrophysiology studies in collaboration with Graeme Davis's group. RIM thereby was found to be involved in maintaining proper synaptic baseline transmission, presynaptic calcium influx and the size of the readily releasable pool (RRP) of SVs, consistent with known activities of RIM (Müller et al., in review). Electrophysiology data also defined a novel role for RIM in the homeostatic control of neurotransmitter release (Müller et al., in review; details in Discussions section 5.1.2).

4.6 RIM-binding protein (DRBP) is a novel component of the AZ cytomatrix

In the previous sections, we have reported our studies about the *Drosophila* RIM protein, whose mammalian homologue is a key component in the AZ scaffold. Mammalian RIMs are reported to directly interact with the presynaptic voltage-gated Ca^{2+}-channel $\alpha 1$ subunit (Wang et al., 2000; Kaeser et al., 2011). We have investigated the RIM homologue in our system independently and found that RIM hypomorphic alleles that we have generated (*rim*$^{ex1.26}$, *rim*^{del71}, *rim*^{del103} and *rim*^{Minos}) showed less prominent defects. Thus, RIM may not be fundamental in organizing Ca^{2+}-channels at active zones of *Drosophila*. We next sought to screen for a novel master organizer at the AZ that is pivotal for Ca^{2+}-channels clustering.

In *Drosophila*, homologues for most mammalian AZ cytomatrix components are encoded (Schoch and Gundelfinger, 2006; Jin and Garner, 2008). From those, we chose the *Drosophila* homologue of RIM-binding proteins (RIM-BPs) as our gene target. *Drosophila* encodes a single *drbp* gene (here short *Drosophila* RBP, DRBP; gene locus (CG43073)), while mammals encode three RIM-BPs-family loci (Mittelstaedt and Schoch, 2007). Mammalian RIM-BPs have been described to interact with Ca^{2+}-channels and be enriched at presynaptic terminals (Hibino et al., 2002; Wang et al., 2000; Mittelstaedt and Schoch, 2007). However, its synaptic role remains unclear. Here, we describe the use of *Drosophila* as a model system to elucidate the critical structural and functional roles of fly RIM-BPs in building the AZ cytomatrix architecture and proper SV release.

The detailed genomic organization and a gene model of the *drbp* (CG43073) locus are illustrated in Fig. 4.9B-C. DRBP covers several annotated genes spanning chromosomal regions 88F1-F4. FlyBase predicts 7 isoforms for DRBP. We here refer to DRBP isoform PB, since it was the longest predicted isoform available when we first started our investigations. The predicted coding DNA sequence (CDS) of *drbp* is 1599 aa long and encompasses 19 exons. Predicted domain organizations invariably contain three Src homology 3 (SH3) domains (I-III) with a stretch of fibronectin 3 (FN3)-like domains between SH3-I and SH3-II among various species (Wang et al., 2000; Hibino et al., 2002; Mittelstaedt and Schoch, 2007) (Fig. 4.9A).

4.7 Production of N- and C-terminal antibodies

First, we raised antibodies against N- and C-terminus of DRBP (Material and Methods section 3.3) to address the localization of DRBP at *Drosophila* synapses. Both peripheral synapses at NMJs (Fig. 2A in Liu et al., 2011) and adult brain CNS synapses were stained (Fig. 4.15 - 4.17, discussed later). Staining pattern of both antibodies (epitopes see Fig. 4.9A) showed close proximity to BRP puncta at the AZ when co-stained with Bruchpilot^{Nc82}. We conclude that DRBP is an AZ protein at the *Drosophila* NMJ.

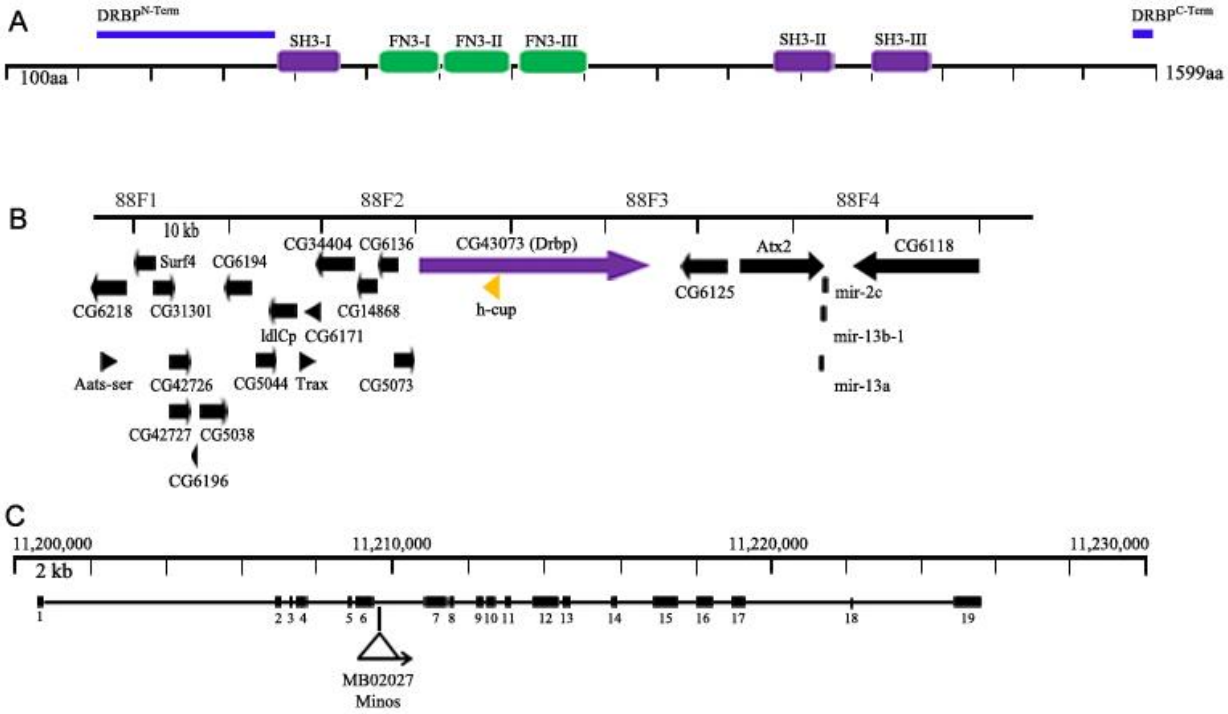

Fig. 4.9 Schematic representation of the *drbp* locus.
(A) DRBP entails three Src homology 3 (SH3) domains interrupted by Fibronectin type 3 (FN3) domains. Antibody binding epitopes for N- and C-termini DRBP antibodies were shown in blue (based on FlyBase CG43073-PB). (B) Genomic organization of the *drbp* (CG43073) locus. A subset of annotated genes in the chromosomal region 88F1-F4 was illustrated. (C) Gene model of *drbp*. *drbp* encompasses 19 exons. The position and orientation of *Minos* element Mi{ET1}MB02027 insertion (*drbp*^{Minos}) in the *drbp* locus was depicted.

4.8 Generation of tools for molecular and genetic analysis of DRBP

4.8.1 *drbp* deficiency strain

There was one pair of *piggyBac* element insertion resided upstream (PBac{WH}f00570) and in the coding region of *drbp* locus (PBac{WH}CG43073^{f07217}) (not shown, details in FlyBase) that allowed generation of the intragenic *drbp* mutant by means of FLP-FRT recombination deletion screening. However, one of the *piggyBac* transposon element ends of PBac{WH}f00570 was defect or incomplete (test PCR, data not shown). Therefore we

utilized another pair of parental *piggyBac* transposon lines that is adjacent to the *drbp* locus: P{XP}d00347 and PBac{RB}Atx2[e00368] to produce a deficiency strain of *drbp* (Fig. 4.10A, triangles).

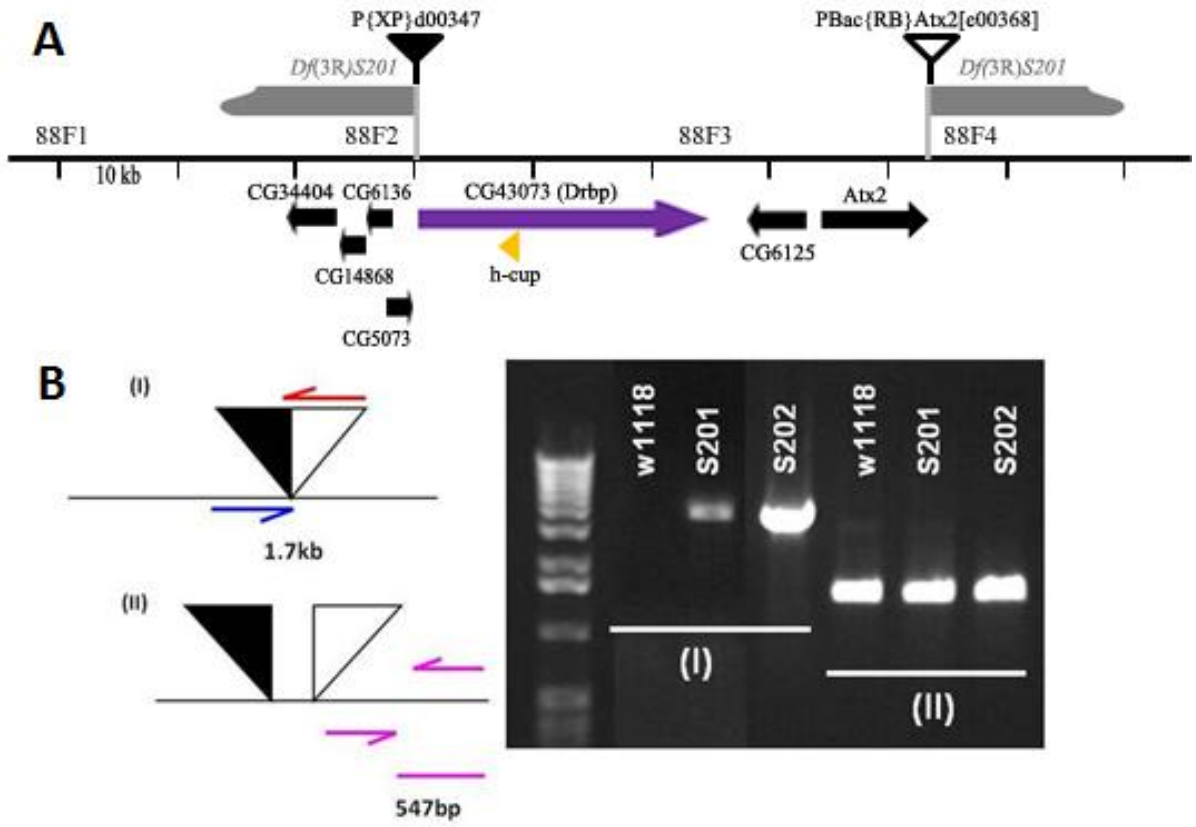

Fig. 4.10 Production of *Df*(3R)*S201* based on FLP-FRT recombination.
(A) Parental *piggyBac* transposon lines P{XP}d00347 and PBac{RB}Atx2[e00368] (in triangles) were chosen to create *Df*(3R)*S201*. (B) (I) Screening of positive candidates by the loss of eye color in deletion generation and confirmation with the presence of a 1.7 kb fusion amplicon of both parental *piggyBac* elements by RT-PCR (line S201 and S202) (II) Internal control experiment indicated the presence of DNA template for the screen PCRs performed.

Expression of heat shock–driven FLP recombinase at 37 °C provokes the precise recombination deletion between two FRT-bearing transposon insertions in *trans* (Parks et al., 2004). Deletions were first detected in the progeny by a loss of the w^+ marker (w^- eye color), dependent on the orientation and nature of parental *piggyBac* elements chosen (*XP* and *RB* pair chosen in this deletion screen, Fig. 4.10A). Two candidates with w^- eye color out of 65 single crosses were shortlisted for further hybrid PCR screenings. Chromosomal deletions of a genomic region spanning between parental lines were confirmed by PCR amplification of a 1.7 kb hybrid product using element-specific primers (hybrid PCR). The removal of the genomic region spanning the entire *drbp* coding DNA sequence and genes in nearby loci (Fig. 4.10A) was validated by the presence of a specific 1.7 kb amplicon (4.10B(I)). An internal control experiment (4.10B(II)) indicated the presence of DNA sample/ template for the PCR

screens performed. A deficiency strain of *drbp*, *Df*(3R)*S201* was hence retrieved by the *piggyBac* elements deletion mutation screening. Based on the FlyBase CG43073-PB isoform (1599 aa), *Df*(3R)*S201* removes 42.303 kb of a genomic region spanning between two parental lines. Homozygous *Df*(3R)*S201* animals are embryonic lethal and only balanced animals can develop to adulthood. The w^- background and the embryonic lethality of *Df*(3R)*S201* provide a valuable tool for further genetic analysis.

4.8.2 *Minos* element as a hypomorphic *drbp* intragenic allele

The only available intragenic element in the *drbp* locus is the *Minos* transposon that inserted between the 6th and 7th exon (based on FlyBase CG43073-PB, 1599 aa; Fig. 4.9C, MB02027, $drbp^{Minos}$). $drbp^{Minos}$ was positioned in *trans* over a self-produced deficiency entailing *drbp* as well as a neighboring locus (*Df*(2R)*S201*, see Fig. 4.10). In these larvae, DRBP levels ($DRBP^{C\text{-}Term}$) at NMJs were reduced to one third of control levels (Fig. 2A in Liu et al., 2011) and one quarter of control levels in adult CNS synapses (Fig. 4.17B´ and D). These hypomorphic *drbp* mutant flies hatched below the expected Mendelian ratio (Table 4.2) and mutant larvae showed markedly reduced locomotion (Fig. 4.14). We predicted this transposon insertion to be an interesting candidate for the loss of function assay because it resides within a coding exon in the *drbp* locus.

4.8.3 Attempt to retrieve *drbp* loss of function alleles by *Minos* element mobilization

Intragenic *Minos* transposon shows reduced $DRBP^{C\text{-}Term}$ stainings at NMJ (Fig. 2A in Liu et al., 2011) and adult CNS synapses (Section 4.10). However, hypomorphic $drbp^{Minos}$ is found to be insufficient to satisfactorily address DRBP's role at the AZ. We intended to extend our genetic screenings in the *drbp* locus by using imprecise mobilization of the *Minos* transposon element (Introduction section 2.4.3). We aimed to isolate *drbp* null alleles by this approach since insertion site of the parental $drbp^{Minos}$ (Fig. 4.11A) is close to the N-terminus of the DRBP peptide. A deletion screen in the hope of random removal of adjacent *drbp* genomic regions upon mobilization of the GFP-tagged *Minos* element was carried out. Successful mobilization events mediated by heat-activated *Minos* transposase were first screened by the removal of the pMiET1 construct in which fluorescence was no longer detectable (marked by 3xEGFP construct, see also Fig. 4.11B). The observed mobilization rate of the *Minos* element upon activation by *Minos* transposase was relatively high in our study, around 8 % (50 potential candidates with loss of 3xEGFP in 600 single crosses).

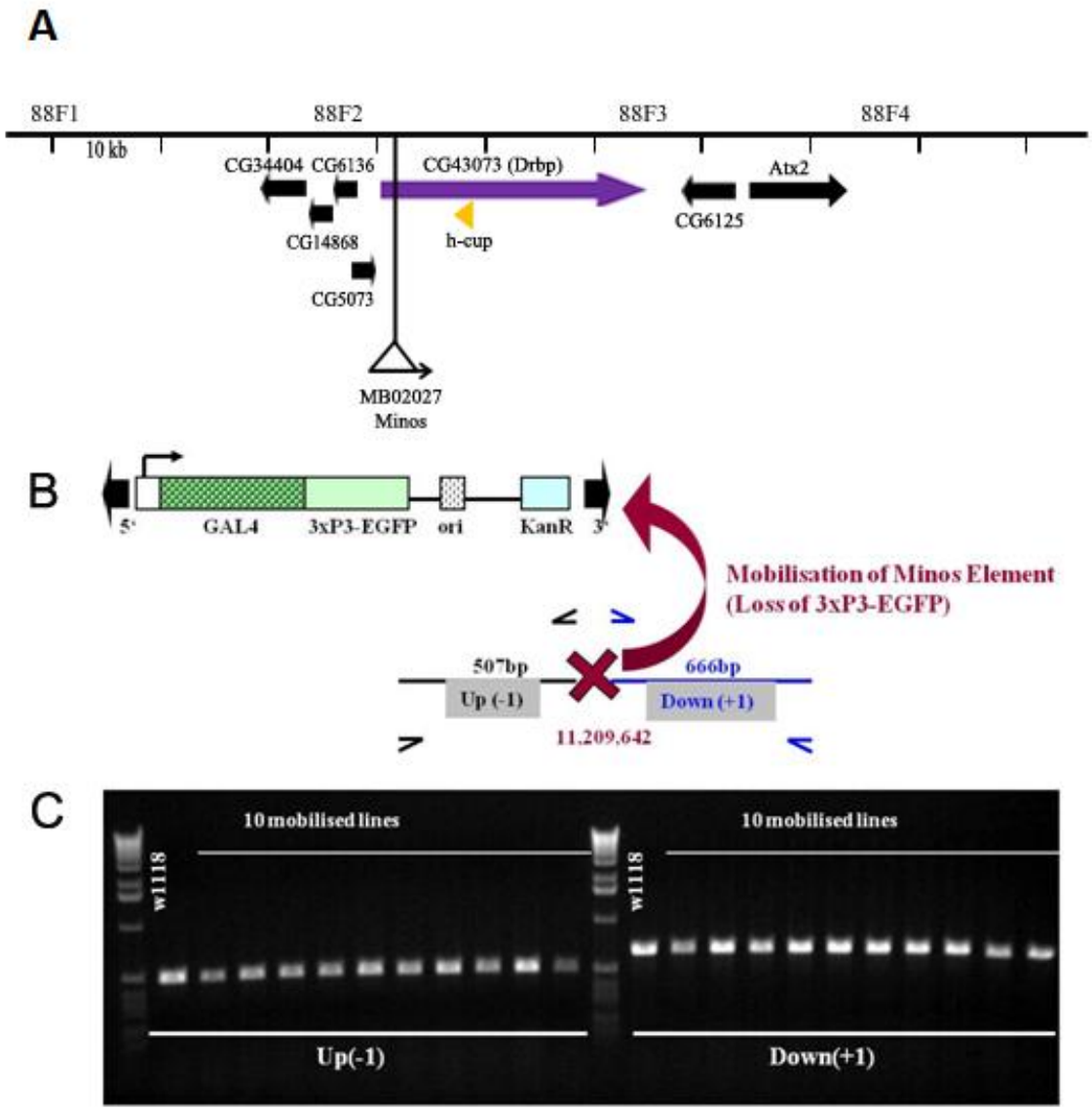

Fig. 4.11 Schematic representation of the attempt to mobilize *Minos* element MB02027.
(A) Genomic organization of the *drbp* locus illustrated position of the transposable *Minos* element (MB02027) insertion. (B) Mobilized candidates were first sorted by the loss of the 3xEGFP construct and subjected to single-fly PCR (over deficiency) to map the deletion event (pMiET1 construct). Specific primers amplifing up- and downstream genomic regions (-1 and +1) of the insertion site were designed to check for the deletion. (C) Example of 10 mobilized fly lines subjected to the single-fly PCR screening. DNA extracted from adult progeny of 50 potential *drbp* alleles (in *trans* to *Df*) was used as genetic material for single fly PCR screening. Unfortunately precise jump out of *Minos* element from the insertion site did not cause a detectable excision of up- or downstream genomic regions flanking the locus by PCR.

Specific primers amplifying up- and downstream genomic regions (-1 and +1) (refer to Fig. 4.11) of the insertion site were designed to check for the deletion. DNA extracted from adult progeny of 50 potential *drbp* alleles (in *trans* to *Df*) were used as genetic materials for single fly PCR screening. However, PCR screen data of those imprecise excision mutant candidates isolated did not give us a positive outcome (Fig. 4.11C as an example). No random deletion of either upstream (-1 region, 507 bp) or downstream (+1 region, 666 bp) adjacent genomic region upon the mobilization of *Minos* element was detected. We had obtained few candidates

that showed adult lethality but the mapping and characterization was challenging, since the length of bp of the excised genomic sequence was probably too small to be detectable by PCR. The maximum length of genomic sequence excised after *Minos* mobilization reported so far was 800 bp, for the *robo3* gene (Metaxakis et al., 2005). There is little doubt that successful excision to generate mutants by means of this screen also depends on the position of *Minos* insertion and other external factors. Thus, the *Minos* element mobilization screening unfortunately did not return any *drbp* loss of function allele.

4.8.4 Generating DRBP null alleles by chemical mutagenesis

To better characterize the synaptic role of *drbp*, we next sought to generate null alleles by means of other mutant screenings. Chemical mutagenesis was combined with complementation testing over *Df* and $drbp^{Minos}$ to retrieve *drbp* null alleles (experiment was performed by Sara Mertel). Several alleles with premature stop codons in the locus ($drbp^{STOP1}$, $drbp^{STOP2}$, $drbp^{STOP3}$; Fig. 4.12) were isolated.

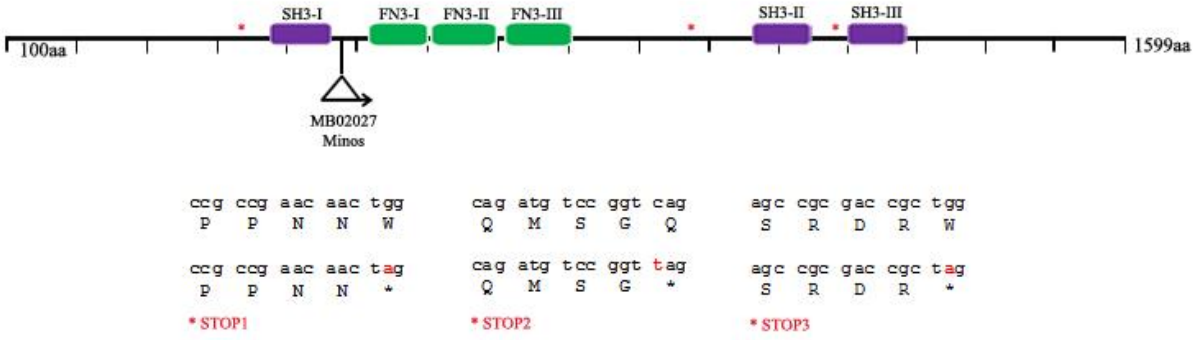

Fig. 4.12 Positions of premature stop codons in *drbp* null alleles that are generated by EMS screenings.

Positions of STOP codons and corresponding mutated nucleotides are indicated in red asterisks. The position and orientation of the *Minos* element Mi{ET1}MB02027 insertion ($drbp^{Minos}$) in the *drbp* locus is depicted.

Animals carrying these alleles over *Df* only rarely reached adulthood (Table 4.2), and mutant larvae barely moved (Fig. 4.14). At mutant larval NMJs (*in trans* to deficiency), DRBP immunoreactivity was completely absent when stained with either N-Term (Fig. S4 in Liu et al., 2011) or C-Term antibodies (Fig. 2A in Liu et al., 2011). Considering the position of premature STOP codons, we assumed them to be either null alleles ($drbp^{STOP1}$) or very close to nulls ($drbp^{STOP2}$, $drbp^{STOP3}$). Subsequent analysis found essentially identical phenotypes for all three STOPs. One copy of the genomic transgene encompassing the entire *drbp* locus (Rescue, see Fig. 4.13A) partially restored NMJ staining (Fig. 2A in Liu et al., 2011) and partially rescued $drbp^{STOP1-3}$ larval vitality (Fig. 4.14).

4.8.5 Genomic rescue construct

DRBP is a large gene in *Drosophila* and the *drbp* locus is spanning a genomic region of 25.149 kb (3R:11,200,584 - 11,225,733 [+]). The predicted full length cDNA of *drbp* isoform PB is of 1599 aa. Due to the lack of complete cDNA clones available, we employed the P[acman] technology to clone the genomic region entailing the entire *drbp* locus.

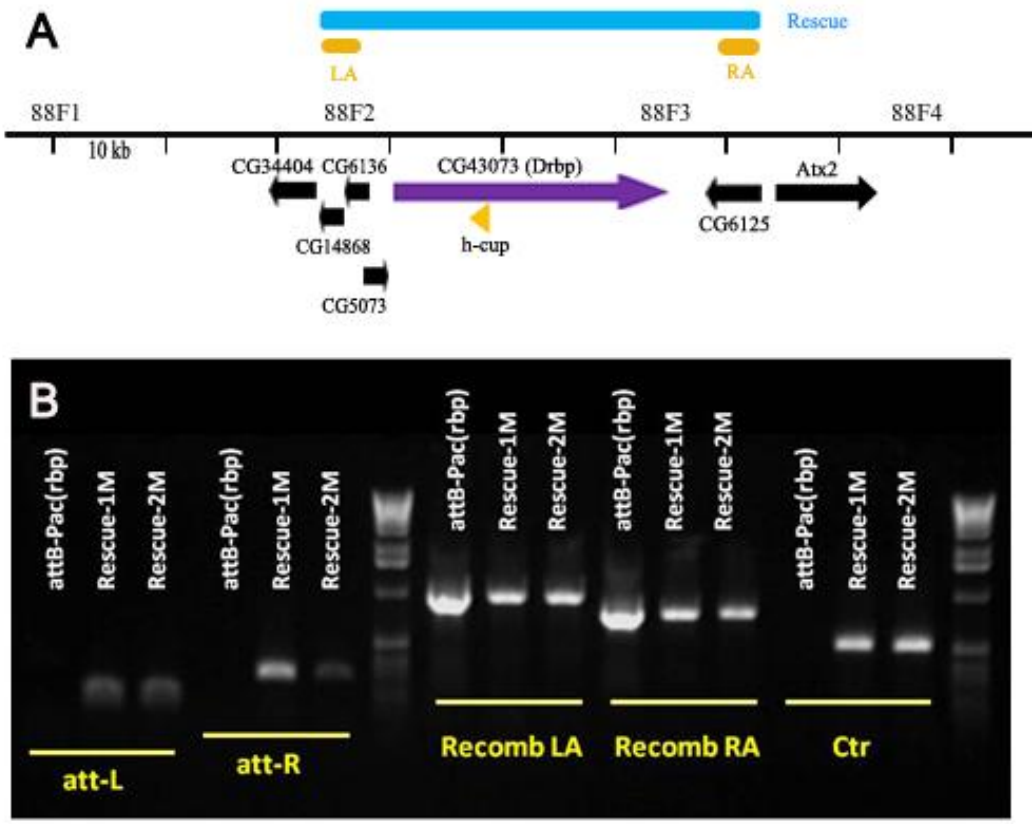

Fig. 4.13 Production of the *drbp* genomic rescue construct based on P[acman] transgenesis.
(A) Position of the *drbp* genomic rescue construct (3R:11,193,728 - 11,230,728) is depicted in blue block. Positions of the left homology arm (LA) and the right homology arm (RA) in creating the *drbp* genomic rescue construct are depicted in orange blocks. (B) PCR result of successful integration of the *attB*-P[acman]-*drbp* plasmid (lines Rescue-1M and Rescue-2M) in the chosen docking site (VK0002 on the 2nd chromosome) is shown, original *attB*-P[acman]-*drbp* plasmid was used as the template for RT-PCR. Control experiments indicated the presence of genomic DNA template only in lines Rescue-1M and Rescue-2M, but not in the original *attB*-P[acman]-*drbp* plasmid.

In brief, a left and right homology arm (LA and RA) located at either end of the targeted *drbp* locus were cloned and ligated into the multiple cloning site of the *attB*-P[acman]-Ap^R vector (see Introduction section 2.5 for details). BAC clone (CH321-59F24) harboring the *drbp* locus was first transformed into the recombineering-competent *E. coli* strain. Later transformation of the linearized *attB*-P[acman]-*drbp* construct into the recombineering-competent *E. coli* strain enabled subsequent recombineering. We successfully produced a *drbp* genomic rescue transgene harboring 37 kb (3R:11,193,728 - 11,230,728) of genomic region based on the BAC transgenic platform (Rescue, see Fig. 4.13A, blue box). Fig. 4.13A

(in orange boxes) depicts the positions of left homology (LA) and right homology arm (RA) designed for the recombineering of the entire *drbp* locus into the *attB*-P[acman] plasmid before PhiC31-mediated transgenesis. Successful integration of the *attB*-P[acman]-*drbp* plasmid at a predetermined *attP* docking site, PBac{yellow[+]-attP-3B}VK00002, into the *Drosophila* genome, was validated by single fly PCR (Fig. 4.13B). DNA extracted from individual w^+ adult flies (lines Rescue-1M and Rescue-2M) were used for PCR reactions. Positive PCR amplification of *attL* and *attR* was detected (Venken et al., 2006 and Introduction section 2.5), while the original *attB*-P[acman]-*drbp* plasmid that served as the negative control showed no amplification (Fig. 4.13C, left, *attL* and *attR*). The presence of recombined LA and RA in the Rescue-1M and Rescue-2M fly strains was also demonstrated (Fig. 4.13C, right, Recomb LA and Recomb RA). One copy of the *drbp* genomic rescue transgene could partially restore $DRBP^{C\text{-}Term}$ staining (larval NMJ and adult CNS synapses; Fig. 2A in Liu et al., 2011 and Fig 4.17), larval vitality (Fig. 4.14) and rescued the deficit in presynaptic neurotransmitter release (Fig. 3 in Liu et al., 2011).

4.9 Characterization of DRBP mutant alleles

4.9.1 Adult DRBP mutants hatched at a lower rate

We first evaluated the effect of the loss of function in DRBP by addressing adult hatching rates. Thus, the *drbp* EMS alleles $drbp^{STOP1}$, $drbp^{STOP2}$, $drbp^{STOP3}$ (provided by Sara Mertel) as well as $drbp^{Minos}$ were placed in *trans* to the deficiency strain, *Df*(3R)*S201*. The number of hatched progeny from two independent crosses was counted. All the *drbp* alleles (DRBP mutants/*Df*) assayed were found to have clearly lower adult vitality than the expected (33.3 %) Mendelian ratio (Table 4.2). By comparing to the normal wild-type control chromosomes, EMS alleles of *drbp* gave the following values: $drbp^{STOP1}$ (0.0 %), $drbp^{STOP2}$ (6.7 %) and $drbp^{STOP3}$ (12.2 %) (data provided by Christoph Mettke, shown in Table 4.2). A milder reduction in adult hatching rate (20.3 %) was observed for the obviously only hypomorphic $drbp^{Minos}$ allele (Table 4.2), in which the position of the transposon insertion may affect downstream transcription/translation of most of the predicted functional domains of *drbp* (see Fig. 4.12 for position).

Table 4.2 Hatching rate of *drbp* mutant flies.
Hypomorphic $drbp^{Minos}$ mutant flies and EMS alleles $drbp^{STOP1\text{-}3}$ (represented by asterisk * in the table) were placed in *trans* to deficiency strain *Df*(2R)*S201*. The number and the percentage of adult progeny (*drbp* allele/*Df*) hatched in each cross are highlighted in grey. All *drbp* mutant adults (*drbp* allele/*Df*) hatched below Mendelian ratio. $drbp^{Minos}$ adult hatched 13 % less and $drbp^{STOP1\text{-}3}$ adults hatched at least 23 % less than expected Mendelian ratio of 33.3 % (data pooled with diploma thesis of Christoph Mettke, 2010).

	First cross against *Df*(3R)*S201*			Second cross against *Df*(3R)*S201*				Average percentage of both crosses		
	w[1118]/w[1118]; +/+ ; */Df(3R)S201	w[1118]/w[1118]; +/+ ; Df(3R)S201/TM3, P{ActGFP}JMR2 Ser[1] OR w[1118]/w[1118]; +/+ ; Df(3R)S201/ TM6, Tb	w[1118]/w[1118]; +/+ ; */TM3, Sb[1] Kr-GFP OR w[1118]/w[1118]; +/+ ; */ TM6, Tb	w[1118]/w[1118]; +/+ ; */Df(3R)S201	w[1118]/w[1118]; +/+ ; Df(3R)S201/TM3, P{ActGFP}JMR2 Ser[1] OR w[1118]/w[1118]; +/+ ; Df(3R)S201/ TM6, Tb	w[1118]/w[1118]; +/+ ; */TM3, Sb[1] Kr-GFP OR w[1118]/w[1118]; +/+ ; */ TM6, Tb	**Total number of hatched flies**	w[1118]/w[1118]; +/+ ; */Df(3R)S201	w[1118]/w[1118]; +/+ ; Df(3R)S201/TM3, P{ActGFP}JMR2 Ser[1] OR w[1118]/w[1118]; +/+ ; Df(3R)S201/ TM6, Tb	w[1118]/w[1118]; +/+ ; */TM3, Sb[1] Kr-GFP OR w[1118]/w[1118]; +/+ ; */ TM6, Tb
***drbp*^{Minos}**	19	37	41	23	42	45	207	20.3%	38.2%	41.5%
***drbp*^{STOP1}**	0	26	39	0	27	41	133	0.0%	39.8%	60.2%
***drbp*^{STOP2}**	6	20	45	2	14	32	119	6.7%	28.6%	64.7%
***drbp*^{STOP3}**	3	17	20	7	25	26	98	10.2%	42.9%	46.9%

4.9.2 The *drbp* alleles show larval locomotive defects

We then addressed the larval locomotive behavior in *drbp* mutation alleles. *drbp* EMS alleles *drbp*^{STOP1}, *drbp*^{STOP2}, *drbp*^{STOP3} (provided by Sara Mertel) and hypomorphic *drbp*^{Minos} were placed in *trans* to the *Df*(3R)*S201* deficiency strain. Third instar larvae of each genotype were put on an agarose plates and the number of contractile motions per 30 seconds was measured. All of the tested *drbp* mutation alleles (DRBP mutant/*Df*) showed deficits in their larval locomotive ability (Fig. 4.14). *drbp*$^{STOP1-3}$ larvae moved about 75 % less and *drbp*^{Minos} larvae moved about 50 % less than control larvae (control: 29.3 ± 0.3; *drbp*^{Minos}: 17.0 ± 0.3; *drbp*^{STOP1}: 7.4 ± 0.2; *drbp*^{STOP2}: 7.8 ± 0.2; *drbp*^{STOP3}: 11.9 ± 0.1; P<0.0001 compared to control, 2 way ANOVA test) (Fig. 4.14). One copy of the genomic transgene encompassing the entire *drbp* locus (Rescue, see Fig. 4.13A) was introduced. EMS alleles *drbp*$^{STOP1-3}$ and *drbp*^{Minos} were placed in *trans* to the *drbp* deficiency (genetically combined with the *drbp* genomic transgene). It partially rescued locomotive defects of *drbp* $^{STOP1-3}$ and *drbp*^{Minos} larvae (Rescue; *drbp*^{Minos}: 23.4 ± 0.3; Rescue; *drbp*^{STOP1}: 20.9 ± 0.2; Rescue; *drbp*^{STOP2}: 22.1 ± 0.2; Rescue; *drbp*^{STOP3}: 21.7 ± 0.3; P<0.0001 compared to respective *drbp* mutants, Mann-Whitney U test) (Fig. 4.14). This assay revealed deficits in larval locomotion in hypomorphic *drbp*^{Minos} and all of the *drbp* EMS alleles (DRBP mutant/*Df*); introduction of one copy of *drbp* genomic rescue is sufficient to restore the larval locomotive ability of DRBP mutants partially in *drbp* null background.

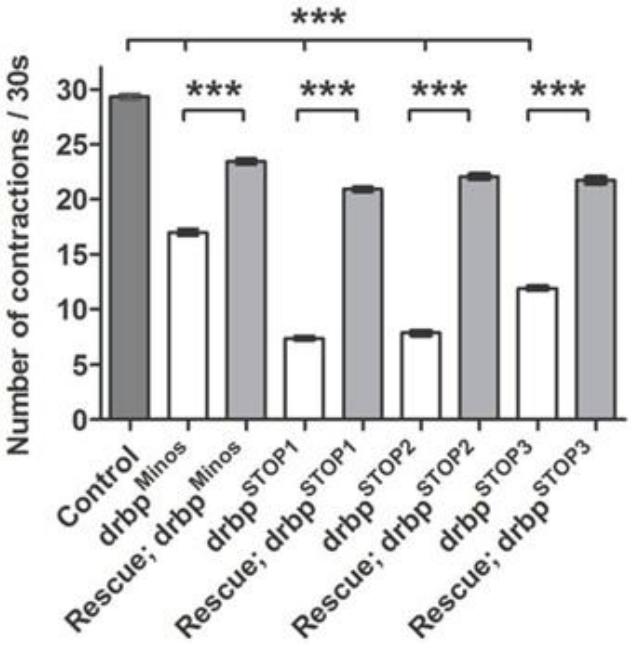

Fig. 4.14 Locomotion assay of *drbp* mutant larvae.
Third instar larvae of each genotype were put on an agarose plate and number of contractile motions per 30 seconds was measured (3 times for each larva, n = 15 larvae). $drbp^{Minos}$ larvae moved about 50 % less and $drbp^{STOP1-3}$ larvae about 75 % less than control larvae (control: 29.3 ± 0.3; $drbp^{Minos}$: 17.0 ± 0.3; $drbp^{STOP1}$: 7.4 ± 0.2; $drbp^{STOP2}$: 7.8 ± 0.2; $drbp^{STOP3}$: 11.9 ± 0.1; P<0.0001 compared to control, 2 way ANOVA test). Locomotive defects could be partially rescued by introduction of one copy of the *drbp* genomic rescue construct (Rescue; $drbp^{Minos}$: 23.4 ± 0.3; Rescue; $drbp^{STOP1}$: 20.9 ± 0.2; Rescue; $drbp^{STOP2}$: 22.1 ± 0.2; Rescue; $drbp^{STOP3}$: 21.7 ± 0.3; P<0.0001 compared to respective *drbp* mutant, Mann-Whitney U test).

4.9.3 Role of DRBP in the AZ

To further characterize the synaptic role of DRBP, the DRBP null $drbp^{STOP1}$ and hypomorphic $drbp^{Minos}$ were subjected to larval NMJ stainings (confocal and STED microscopy); ultrastructure analysis (electron microscopy) and electrophysiology studies in collaboration with our colleagues. In the following sections, results from the ultrastructure analysis and the electrophysiology studies are highlighted.

4.9.3.1 Role of DRBP in maintaining the proper ultrastructure of AZ cytomatrix

(Experiment was performed by Dr. Carolin Wichmann, figure is put here for illustration) To understand whether AZ cytomatrix organization is affected in *drbp* mutants, transmission electron microscopy analysis was carried out. Both TEM of high-pressure frozen/freeze-substituted (Rostaing et al., 2004; Siksou et al., 2007; Fouquet et al., 2009) (Fig. 4.15) and conventionally embedded (Fig. S5 in Liu et al., 2011) samples in *drbp* mutants were imaged. In 3D electron tomography reconstructions, the entire cytomatrix of *drbp* null ($drbp^{STOP1}/Df$) was severely misshapen (Fig. 4.15B). At AZ membranes of *drbp* nulls, abnormally shaped electron-dense material but no regular T bars were found (Fig. 4.15A). Structures resembling

T bars platforms remained present in the *drbp* hypomorph (*drbp*^{Minos}/*Df*) but were clearly defective in size and conformation. Pedestals were mostly affected as indicated in a significant drop of T bar width (Fig. 4.15A, arrowheads). Free-floating electron-dense material detached from the AZ plasma membrane was occasionally observed in *drbp* nulls (Fig. S5C-D in Liu et al., 2011) and these atypical electron-densities still tethered SVs (Fig. S5B in Liu et al., 2011, arrows; insets in C-D). SVs tethering function may still be mediated by the C-terminal end of Bruchpilot (Hallermann et al., 2010). In addition, numbers of membrane-proximal SVs (up to 5 nm distance) counted over the whole AZ were slightly but significantly reduced in *drpb*^{STOP1} animals (Fig. 4.15B). Severe defects in the structural integrity of the pedestal foot structure of the cytomatrix were observed, arguing for a role of DRBP as a critical building block for the proper assembly of AZ cytomatrix. The slight decrease in SVs at the AZ membrane may also suggest a role of DRBP in SV priming, docking and tethering.

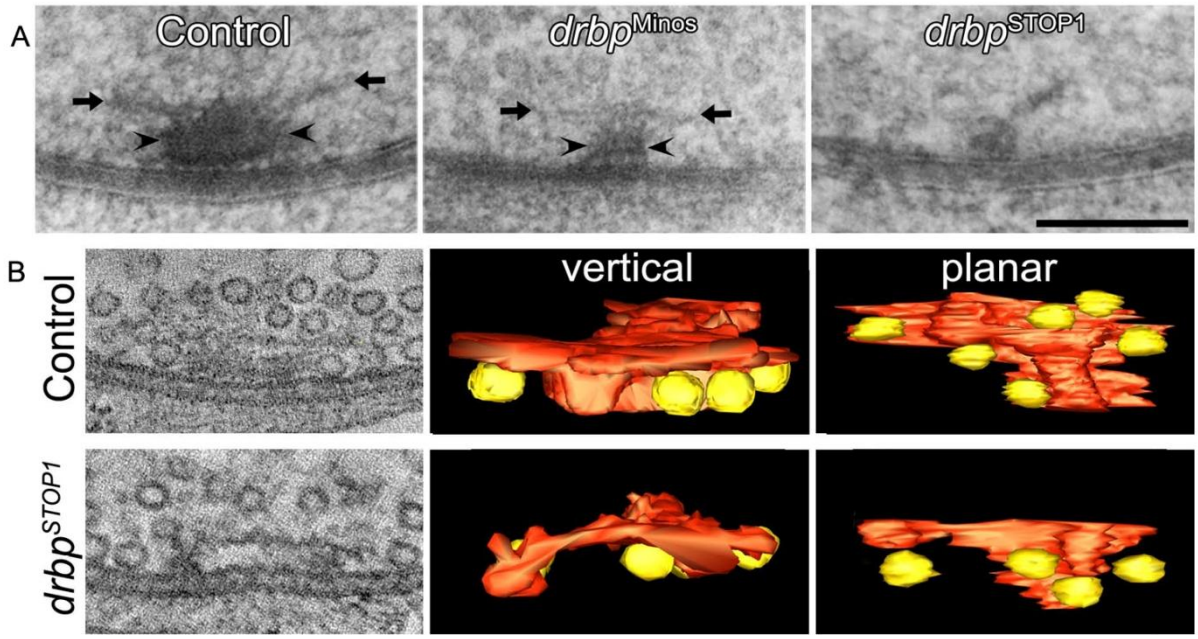

Fig. 4.15 *drbp* mutant synapses show ultrastructural defects under transmission electron microscopy.
"(A) T bar EM images from controls, *drbp*^{Minos} and *drbp*^{STOP1} NMJs. T bar pedestals marked with arrowheads, T bar platforms with arrows. In *drbp*^{Minos} T bars appear thinner whereas *drbp*^{STOP1} synapses lack normally shaped T bars. (B) Electron tomography of control and *drbp*^{STOP1} T bars. Left: virtual single section from reconstructed tomogram. Rendered model is shown in the middle (vertical view) and right (planar view from the bottom on the pedestal) panels. Red: T bar; yellow: membrane proximal SVs. Scale bars: 100 nm" (taken from Liu et al., 2011).

4.9.3.2 DRBP is essential for synaptic transmission

(Experiment was performed by Elena Knoche and Stephanie Wegener; figure is put here for illustration) To address whether DRBP is important for synaptic transmission, two-electrode voltage clamp recordings were performed at larval NMJs in the presence of 1 mM Ca^{2+}. In the

drbp hypomorph larvae, evoked excitatory junctional current (eEJCs) amplitudes were reduced by about half compared to controls and eEJC was practically abolished in *drbp* null larvae (Fig. 4.16A). eEJC amplitudes remained only at about 10% of the control level for all three null alleles tested (over deficiency) by recording in elevated extracellular Ca^{2+} (Fig. 4.16B). One copy of the genomic *drbp* transgene (Fig. 4.13A) completely rescued this deficit in synaptic release (Fig. 4.16B). Miniature excitatory junctional currents (mEJC) amplitudes are an indicator for the spontaneous fusion of single SVs. Both mEJC amplitudes and frequency were unchanged in $drbp^{STOP1}$ (Fig. 4.16C), despite enlarged postsynaptic glutamate receptor fields observed in the NMJ synapses (Fig. 2A-C in Liu et al., 2011). The number of quanta (i.e. SVs) released per individual action potential (quantal content, Fig. 4.16D) was dramatically reduced in the absence of DRBP (Fig. 4.16C). From these experiments, we conclude that DRBP is essential for synaptic transmission at larval *Drosophila* NMJs.

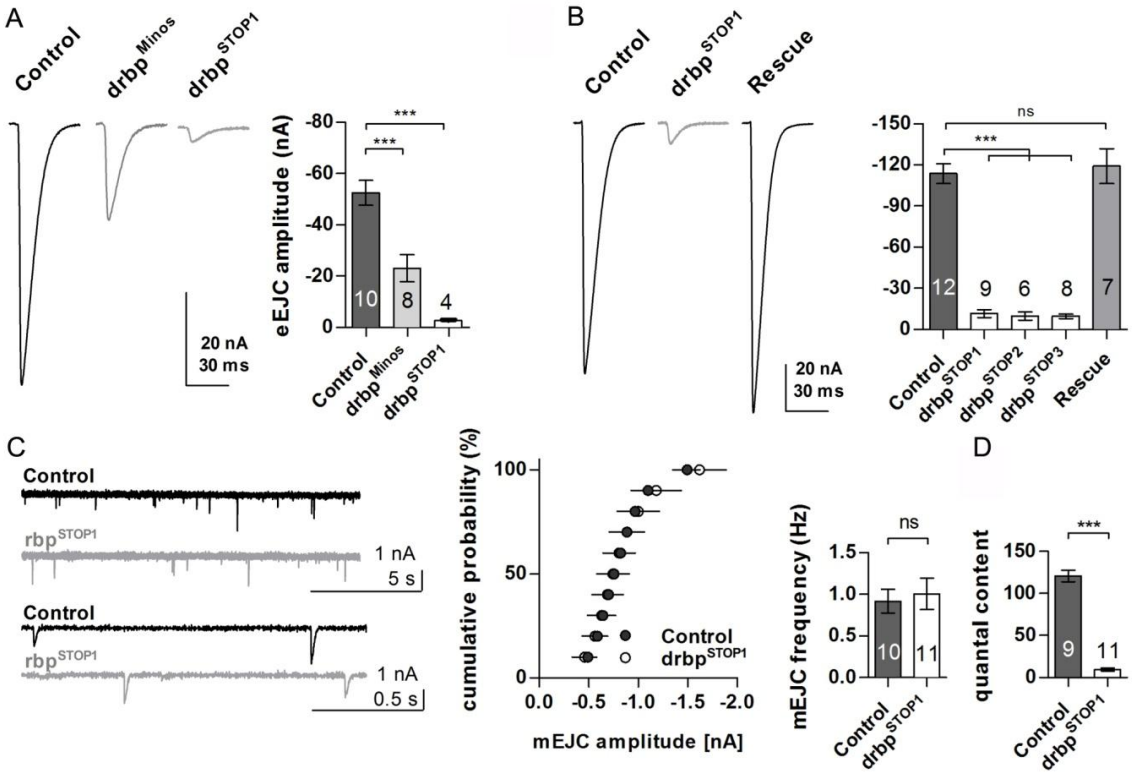

Fig. 4.16 *drbp* mutants suffer from defective evoked neurotransmitter release.

"(A) eEJCs sample traces and quantification for control, $drbp^{Minos}$ and $drbp^{STOP1}$ (1 mM extracellular Ca^{2+}, 0.2 Hz). (B) eEJC sample traces and quantification for control, *drbp* null mutants and genomic rescue recorded at 2 mM extracellular Ca^{2+}. (C) (Left) mEJC Sample traces. (Middle) Mean cumulative histogram of mEJC amplitudes (mean ± standard deviation; two-tailed Kolmogorov-Smirnov test: $P > 0.05$). (Right) mEJC frequency (Control: 0.92 ± 0.14, n = 10; $drbp^{STOP1}$: 1.01 ± 0.19, n = 11; students t test: $P > 0.05$). (D) Quantal content of $drbp^{STOP1}$ eEJCs was significantly reduced (Control: 120.8 ± 6.9, n = 9; $drbp^{STOP1}$: 9.5 ± 1.8, n = 11; $P < 0.0001$; students t test). All panels show mean values and errors bars representing SEM (unless otherwise noted). *, $P \leq 0.05$; **, $P \leq 0.01$; ***, $P \leq 0.001$; ns, not significant, $P > 0.05$" (taken from Liu et al., 2011).

4.10 Use of a hypomorphic *drbp* allele to confirm specificity of DRBP staining at adult CNS synapses

Specific antibodies against N- and C-terminus (epitopes see Fig. 4.9A) of DRBP were raised which stained synapses at NMJs (Fig. 2 in Liu et al., 2011, left). First, we addressed whether these DRBP antibodies also stained central nervous system (CNS) synapses of adult flies. In fact, a neuropile specific labeling could be observed (Fig. 4.17). As a specificity control, the hypomorphic *drbp* allele, $drbp^{Minos}$ (Fig. 4.9C, MB02027) was put in *trans* over the deficiency *Df*(2R)*S201* (Fig. 4.10A). Immunostaining experiments showed that the $DRBP^{C\text{-}Term}$ levels in the adult central brain were reduced to one quarter of control levels (Fig. 4.17B, B´ and B´´: $drbp^{Minos}$; mean gray values 8.61 ± 0.28, n = 6; Fig. 4.17A, A´ and A´´: control 33.62 ± 1.5, n = 8; $p<0.0001$, Mann-Whitney U test; quantifications in Fig. 4.17D (see section 3.7 for details of the analysis). This reduction is consistent with the levels of DRBP staining observed for larval NMJs of this allele (reduction to 36 % of control intensity, Fig. 2A in Liu et al., 2011). One copy of a genomic transgene encompassing the entire *drbp* locus (Rescue, see Fig. 4.13A) partially restored the adult CNS staining (Fig. 4.17C, C´ and C´´: Rescue; $drbp^{Minos}$: 23.92 ± 0.72; $P<0.0001$ compared to control, Mann-Whitney U test). $Bruchpilot^{Nc82}$ levels remained unaltered in the adult CNS of flies carrying the hypomorphic $drbp^{Minos}$ allele (control: 38.59 ± 2.1; $drbp^{Minos}$: 35.08 ± 2.1; Rescue; $drbp^{Minos}$: 35.94 ± 2.3; not significant compared to control, Mann-Whitney U test). Thus, the specificity of the $DRBP^{C\text{-}Term}$ antibody staining at adult CNS synapses is validated with this experiment.

4.11 AZ composition diversity in the fly CNS

4.11.1 DRBP staining in the adult fly CNS

After confirming the specific character of DRBP antibody staining in the CNS, we first compared stainings for N- and C-Term DRBP antibodies. This particularly to understand whether different isoforms might be present differing in N and C-term epitopes (epitopes see Fig. 4.9A). Therefore, CNS staining patterns were compared for N- and C-Term DRBP antibodies in isogenic w^{1118} strain. The observed staining pattern of DRBP antibodies was largely different from the $Bruchpilot^{Nc82}$ label in the adult CNS synapses (Fig. 4.18A, A´´ and B, B´´). The general staining pattern of DRBP N- and C-Term antibodies was similar, with only minor differences in certain neuropiles (compare Fig. 4.18A´ with B´). Mushroom Bodies (MB) lobes is used as an example to demonstrate the degree of difference of DRBP N- and C-Term labels: DRBP showed strong labeling with the N-Term antibody in all the MB lobes (Fig. 4.18A, A´, A´´ and C) while the $DRBP^{C\text{-}Term}$ labeling was strongly enriched in the

α/β lobes, but weaker in the γ lobes and hardly detectable in the α′/β′ lobes (Fig. 4.18B, B´, B´´ and D). With these experiments we show that the labeling with antibodies for the N- and C-Term seems largely not isoform-specific.

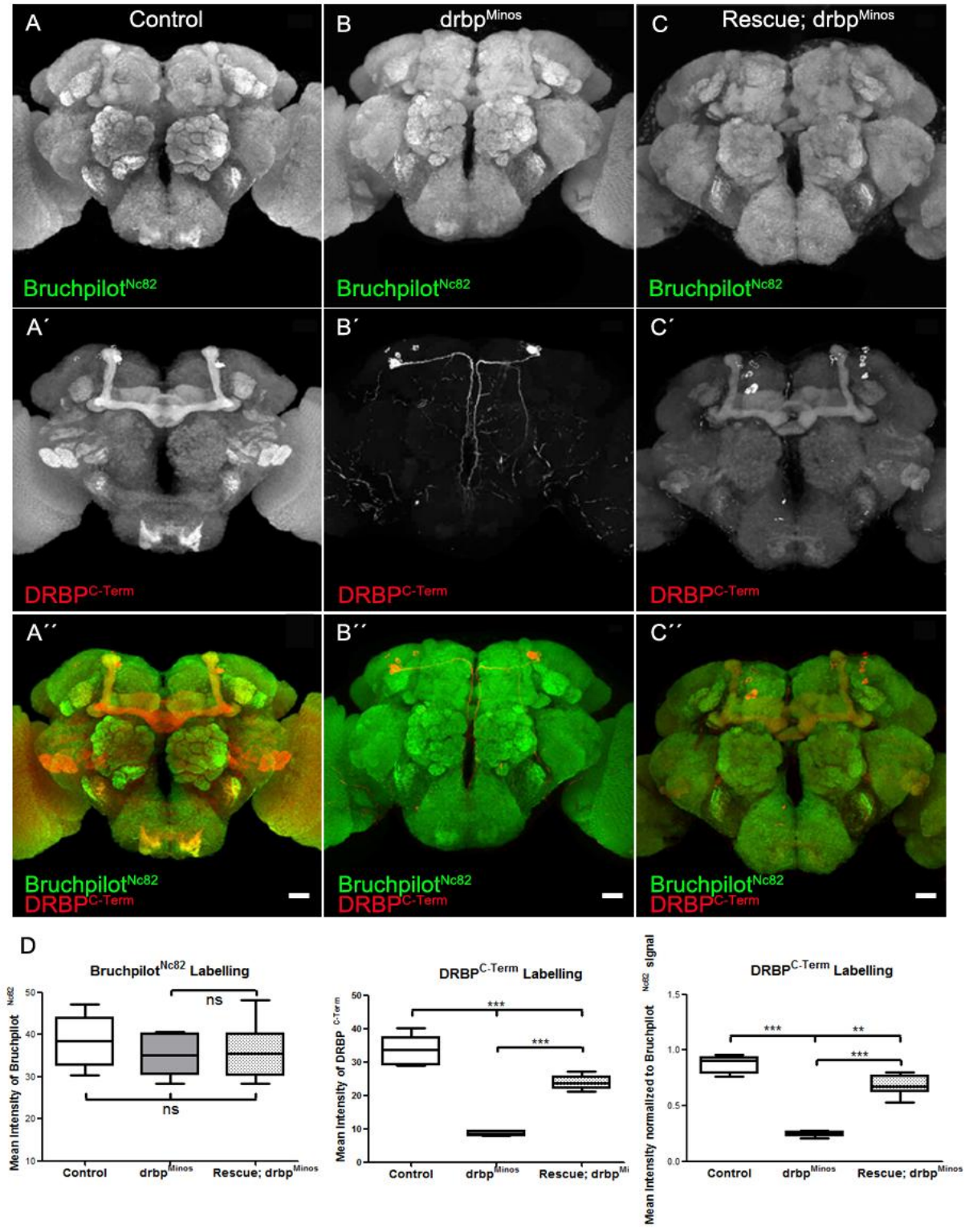

Fig. 4.17 *drbp*^{Minos} shows reduced DRBP$^{C\text{-}Term}$ signal in the adult central brain.
(A,A',A'') Adult CNS synapses of control animals were labeled by DRBP$^{C\text{-}Term}$ antibody (red, merge with Bruchpilot^{Nc82} label in green). (B,B',B'') CNS synapses of *drbp*^{Minos} mutants had severely reduced DRBP$^{C\text{-}Term}$ signal intensity compared to controls and (C,C',C'') staining was partially restored in presence of one copy of a *drbp* genomic transgene (Rescue) in the null mutant background (over *Df*(3R)*S201*). (D) Quantification of

DRBP$^{C\text{-}Term}$ (control: 33.62 ± 1.5; *drbp*^{Minos}: 8.61 ± 0.28; Rescue; *drbp*^{Minos}: 23.92 ± 0.72; P<0.0001 compared to control, Mann-Whitney U test) and Bruchpilot^{Nc82} (control: 38.59 ± 2.1; *drbp*^{Minos}: 35.08 ± 2.1; Rescue; *drbp*^{Minos}: 35.94 ± 2.3; not significant compared to control, Mann-Whitney U test) signal within the central brain region. The central brain region of individual adult brains was segmented and mean gray values of the voxels (volumetric pixels) of the labeled region were calculated using the Amira® software (see Material and Methods section 3.7 for details). n=8 individual animals for the control and rescue groups; n=6 animals for *drbp*^{Minos}. Scale bars equal 20 µm in A´´, B´´ and C´´.

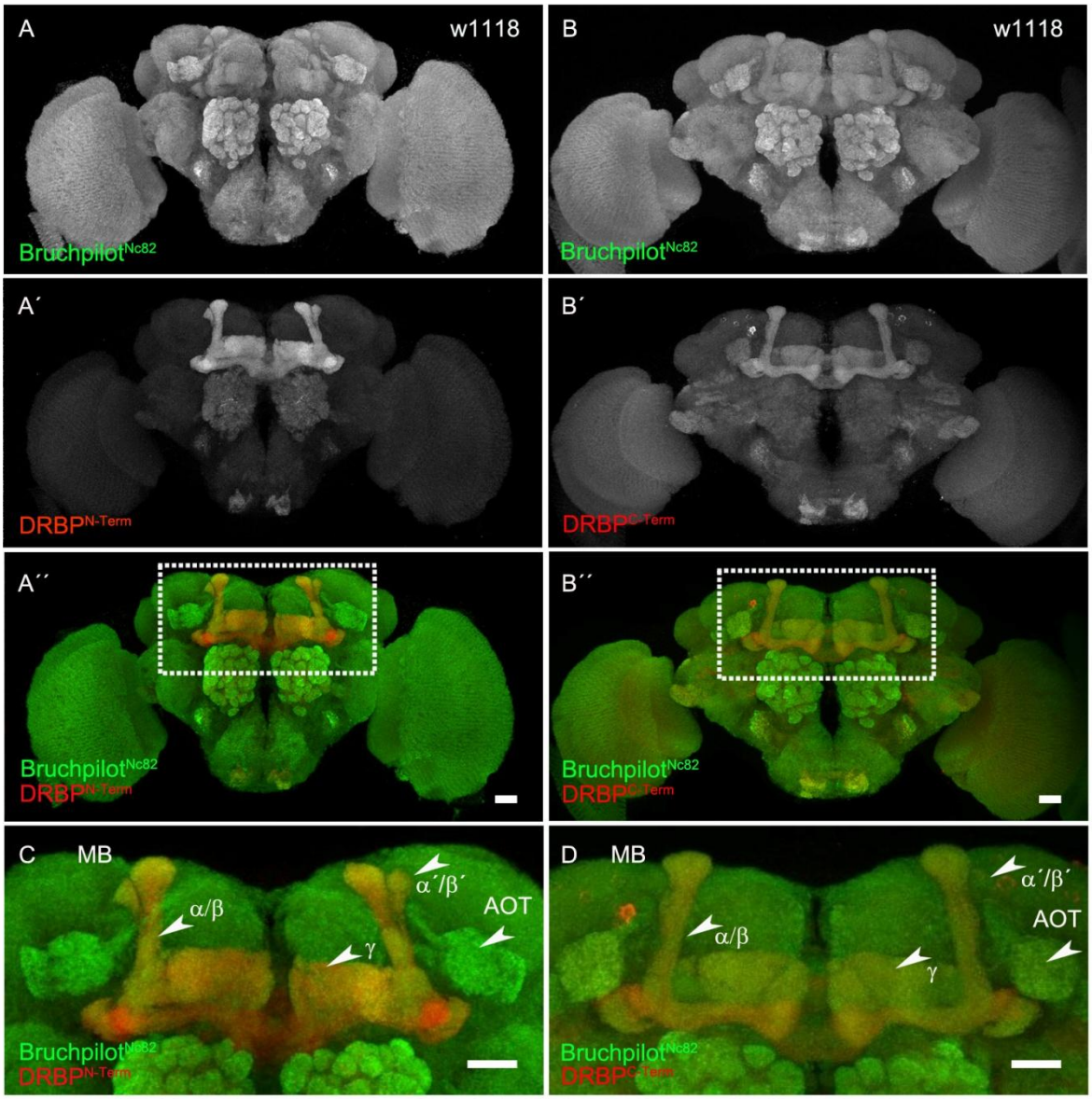

Fig. 4.18 Confocal analysis of DRBP staining at *Drosophila* central nervous system (CNS) synapses.

(A, A´, A´´) DRBP N- or (B, B´, B´´) C-Term label (red) in the w1118 *Drosophila* adult central brain co-labeled with Bruchpilot^{Nc82} (green). Please see the epitopes of DRBP N- or C-Term in Fig. 4.9A. White dashed box indicates area of interest shown at higher magnification in C and D. (C, D) White arrowheads highlight the differential label of DRBP N- or C-Term in mushroom body (MB) lobes and the anterior optic tubercle (AOT). DRBP$^{N\text{-}Term}$ is present and highly accumulates in all the subtypes of the Kenyon cells (KCs): α/β; α´/β´ and γ; DRBP$^{C\text{-}Term}$ label is enriched preferentially in α/β neurons of KCs, when compared to the N-Term label. DRBP$^{C\text{-}Term}$ is clearly present in the AOT but the DRBP$^{N\text{-}Term}$ label is hardly visible here (compare A' and B'); these observations implicate a unique role and function of both the DRBP N- and C-Term, maybe even in olfactory learning and behavior processes. Scale bars in B-E: 20 µm.

4.11.2 DRBP antibody staining pattern in diverse neuropiles of the fly CNS

From all analysis, DRBP is obviously a bona fide AZ protein (Liu et al., 2011). Within AZs, it co-localizes with Bruchpilot. However, initial co-labeling experiments already showed that the ratio between DRBP and Bruchpilot differs between neuropile areas, indicating that the cytomatrix at active zones (CAZ) composition might differ between synapse types. We thus systematically addressed the distribution of DRBP in comparison to Bruchpilot^{Nc82} by acquiring optical slices of several neuropile regions at high magnification (see Material and Methods section 3.7 for parameters of image acquisition). Notably, double labeling of DRBP$^{C\text{-}Term}$ and Bruchpilot^{Nc82} (Fig. 4.19) revealed that synapses in different neuropiles of the fly brain were highly diversified regarding their CAZ protein composition. DRBP-rich synapses concentrated in the central parts of antennal lobe (AL) glomeruli while Bruchpilot^{Nc82} label appeared low at these synapses (Fig. 4.19B, similar observations in DRBP$^{N\text{-}Term}$ staining, not shown). DRBP C-Term-rich synapses accumulated in α/β MB lobes (Fig. 4.19C). A different degree of CAZ composition diversity was also observed in other neuropiles: (Fig. 4.19E) ellipsoid body, (Fig. 4.19F) synaptic input layer in fan-shaped body and optical lobe Fig. 4.19G). I will focus on synaptic CAZ diversity of the AL and of calyx in section 4.13.

4.12 Neuron-population specific *drbp* RNAi helps to assign identity to synapse composition classes

So far, our analysis suggested that different synapse types (different concerning pre- and postsynaptic neuron associated) might differentiate concerning their AZ composition. Thus, to assign AZ composition to synapse type, we performed RNAi experiments in specific neuron populations. For this, a *UAS-drbp-RNAi* line (Stock number: v45926) was acquired from the Vienna *Drosophila* RNAi Center, VDRC (Dietzl et al., 2007) and expression driven pan-neuronally using the GAL4 driver *elav(x)*-GAL4 (Lin and Goodman, 1994). This pan-neuronal expression of *UAS-drbp-RNAi* strongly reduced the specific DRBP$^{N\text{-}Term}$ labeling in almost all neuropiles, including the MB lobes and ALs of adult flies, where *elav(x)*-GAL4 was expressed strongly (Fig. 4.20A, similar observation to the expression pattern of *UAS-2xEGFP* driven by *elav(x)*-GAL4, data not shown). A similar trend for the DRBP$^{C\text{-}Term}$ signal was observed in almost all neuropiles (Fig. 4.21A). Next, we expressed *UAS-drbp-RNAi* in KCs by *ok107*-GAL4 (Connolly et al., 1996). This also provoked a specific and severe loss of DRBP immunoreactivity in all MB lobes of the adult CNS, for both DRBP$^{N\text{-}Term}$ and DRBP$^{C\text{-}}$

Term signal (Fig. 4.20B and 4.21B). We conclude that the *drbp* RNAi construct effectively targets the *drbp* mRNA and thus enables effective knockdown of DRBP in particular neuronal populations.

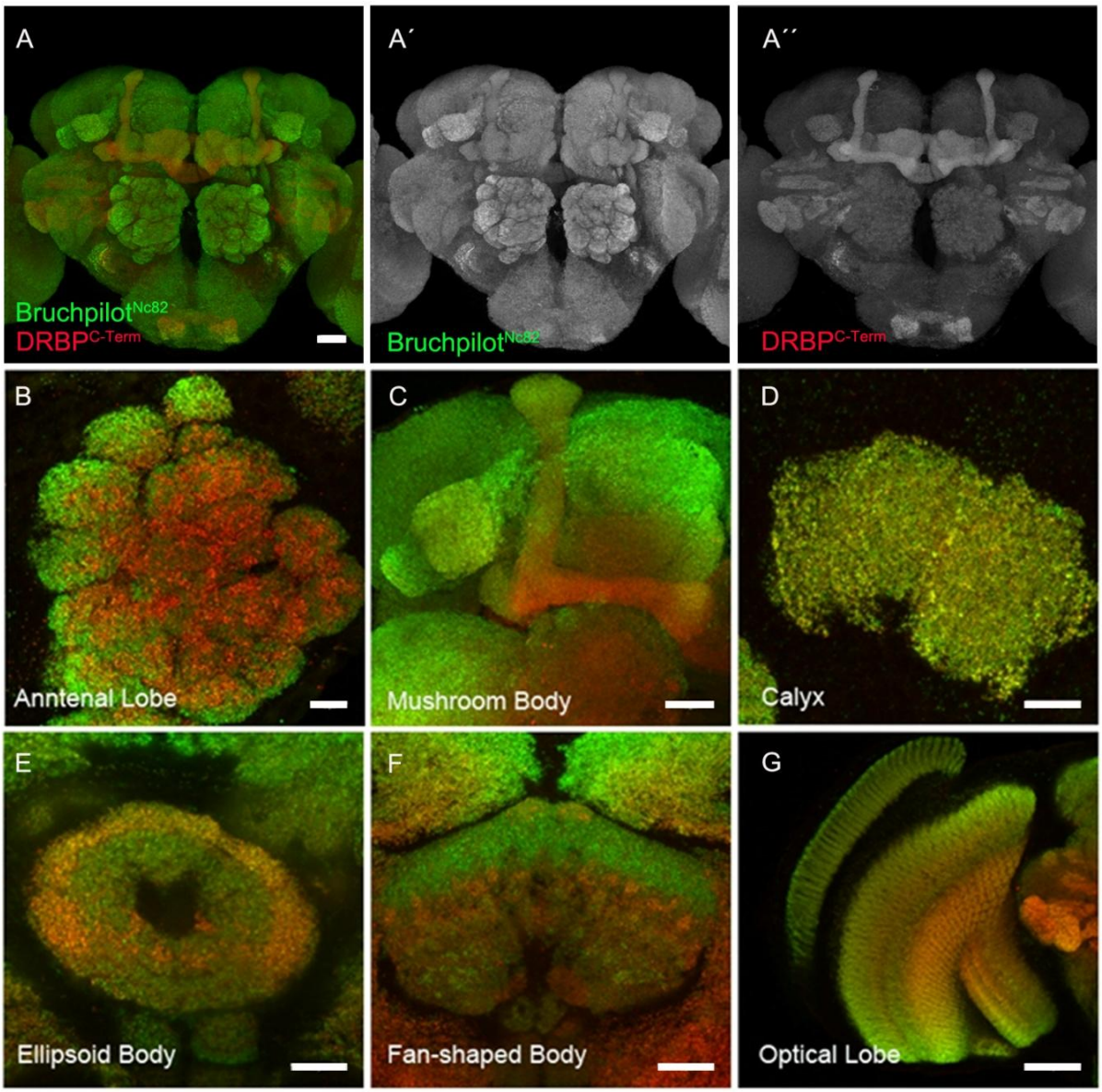

Fig. 4.19 AZ composition diversity in the fly's CNS.

Overview of Bruchpilot Nc82 (green) and DRBP C-Term (red) label in the *w1118 Drosophila* adult central brain (A, A´ and A´´). (B-G) Higher resolution images of different neuropiles: (B) antennal lobes, mushroom body (C) lobes and (D) calyx, (E) ellipsoid body, (F) fan-shaped body and (G) an optical lobe are shown. Synapses in different neuropiles in the fly brain are highly diversified regarding their CAZ composition. Scale bars in A, A´, A´´ equal 20 µm; B-G equal 25 µm.

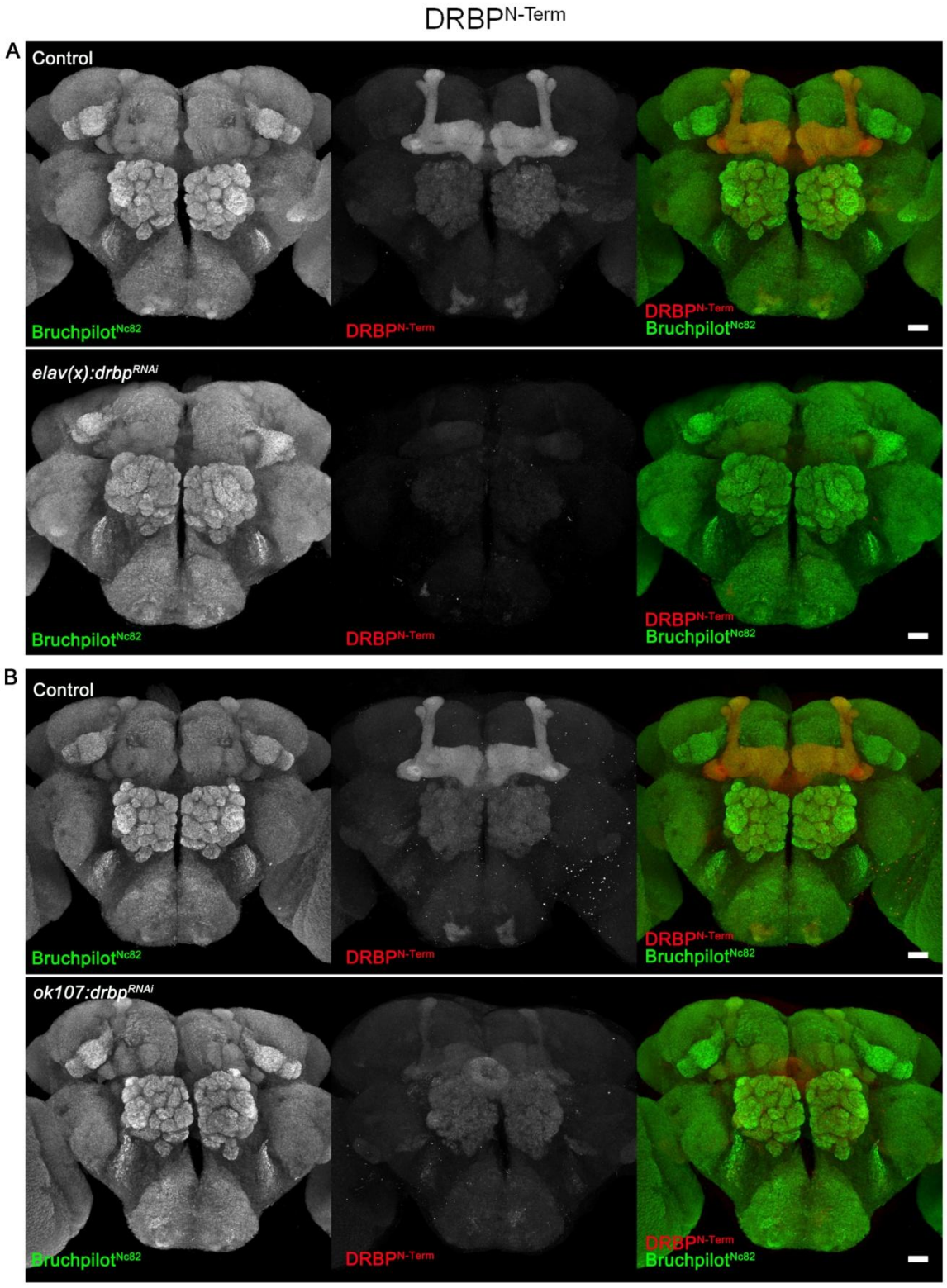

Fig. 4.20 DRBP$^{N\text{-}Term}$ signal is reduced after pan-neuronal expression of *UAS-drbp-RNAi*.

(A) Expression of *UAS-drbp-RNAi* under control of the X-linked elav-GAL4 enhancer-trap line, expressing GAL4 throughout the brain. The *P{w+=GawB}elav*^{C155} is used (Lin and Goodman, 1994). The staining reveals a strong reduction of the DRBP$^{N\text{-}Term}$ signal in almost all neuropiles, particularly in the MB lobes and antennal lobes of adult flies, where elav-GAL4 drives expression strongly. (B) *UAS-drbp-RNAi* expressed in KCs (*ok107*-GAL4, Connolly et al., 1996) provoked a strong reduction of the DRBP label in MB lobes. Scale bars equal 20 µm.

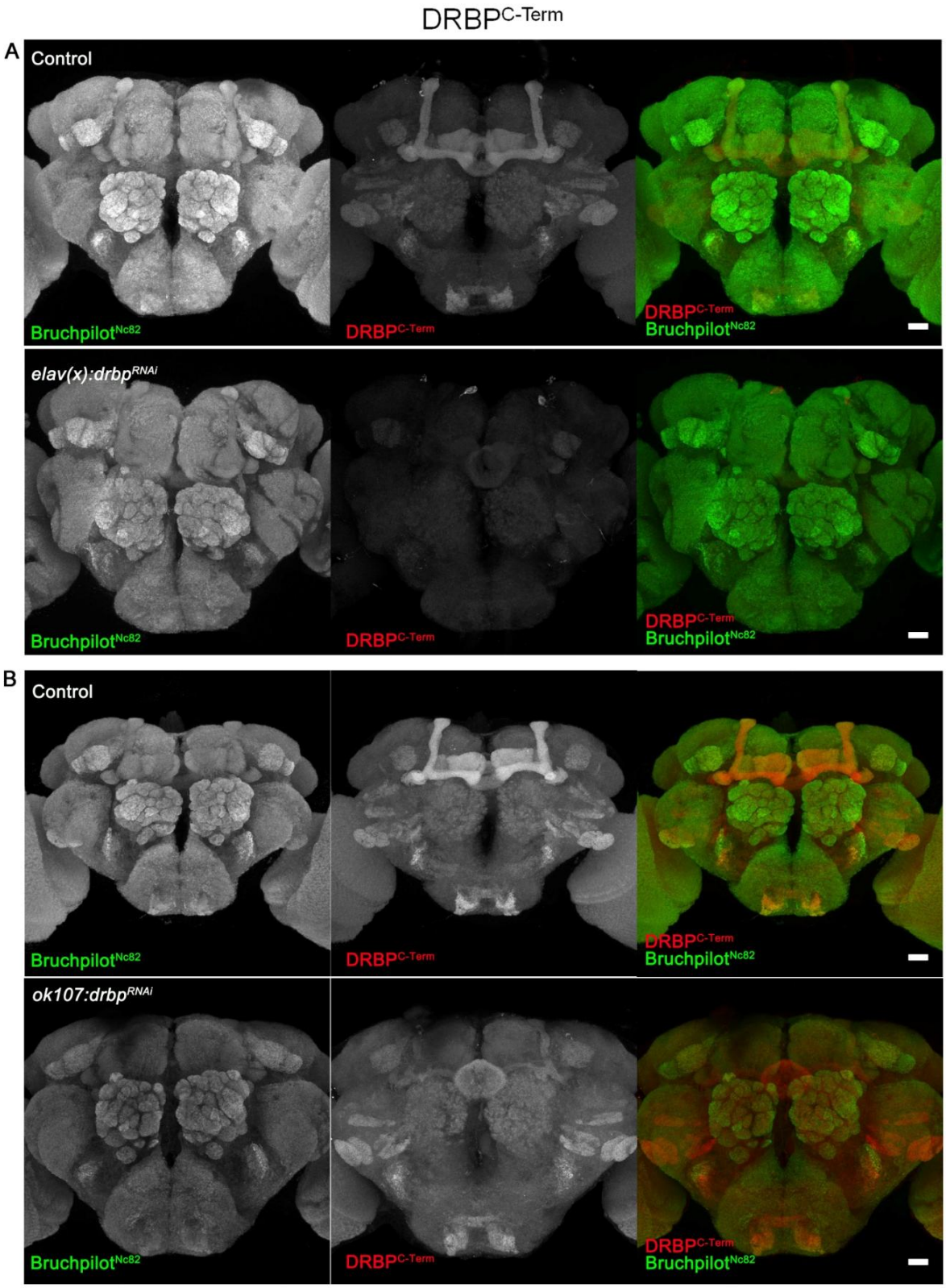

Fig. 4.21 DRBP$^{C\text{-}Term}$ signal is reduced after pan-neuronal expression of *UAS-drbp-RNAi*.

(A) Expression of the *UAS-drbp-RNAi* under control of the panneuronal driver line *elav(x)*-GAL4 (Lin and Goodman, 1994) reveals a strong reduction of the DRBP$^{C\text{-}Term}$ signal in almost all neuropiles, particularly in the MB lobes and antennal lobes of adult flies, where elav-GAL4 drives expression strongly. (B) *UAS-drbp-RNAi* expressed in KCs (*ok107*-GAL4) provoked a strong reduction of the DRBP label in MB lobes. Note that the overall staining intensity is higher for B than for A (compare the Bruchpilot^{Nc82} label). Scale bars equal 20 µm.

4.13 Mapping of DRBP-rich CNS synapses to neuron types

As said above, the heterogeneous labels of DRBP and BRP in certain neuropiles suggested AZ composition diversity in the adult CNS (section 4.11.2) (Fig. 4.19). Next, we sought to study whether and if which neuron populations DRBP-rich synapses could be assigned to. To do that, we drove expression of *UAS-Brp-short*^{GFP} (presynaptic AZ marker) or *UAS-Dα7*^{GFP} (postsynaptic sites) (see Introduction section 2.3.6) in diverse neuronal types (using particular GAL4 lines) and co-labeled with the DRBP$^{C\text{-}Term}$ antibody.

4.13.1 Analysis of AZ diversity in the AL of adult flies

In the previous section (4.11), we had observed that endogenous DRBP label mainly concentrated in the core area of the AL glomeruli (Fig. 4.19B) and hardly showed any co-localization with BRP label. In order to understand this phenomenon, we first mapped the DRBP-positive synapses relative to the presynaptic termini of ORNs. This was done by expressing *UAS-bruchpilot-short*^{GFP} in ORNs using the GAL-4 enhancer trap covering expression of the most abundant OR type (*or83b*). BRP punctae rarely were in close proximity to endogenous DRBP punctae in all the glomeruli (Fig. 4.22A-E). Endogenous DRBP was hardly detectable at presynaptic terminals of ORNs; thereby DRBP-rich synapses may not be abundant at AZs of ORNs.

4.13.1.1 CAZ diversity between AL glomeruli

We next investigated whether endogenous DRBP enrichment opposes postsynaptic PN dendrites. For that, we expressed postsynaptic marker *UAS-Dα7*^{GFP} using *gh146*-GAL4 (expression in PNs). Endogenous DRBP was observed to enrich at postsynapses of PNs in the DL-1 glomerulus (Fig. 4.22A'-E') in only one single experiment. Dendrites of PNs in other glomeruli were rarely in close proximity to endogenous DRBP label. We also did not see this enrichment in DL-1 glomerulus in wild-type without GAL4 driver. It is an interesting finding that DRBP is in close proximity to postsynaptic PN dendrites in this particular glomerulus. We wanted to confirm this observation by expressing *UAS-bruchpilot-short*^{GFP} using *or10a*-GAL4, which labels the ORNs innervating the glomerulus DL-1. However, *UAS-bruchpilot-short*^{GFP} did not co-localize well with DRBP-rich synapses in this experiment (Fig. 4.22A´´-E´´). So, further experiments will have to be carried out to confirm this finding.

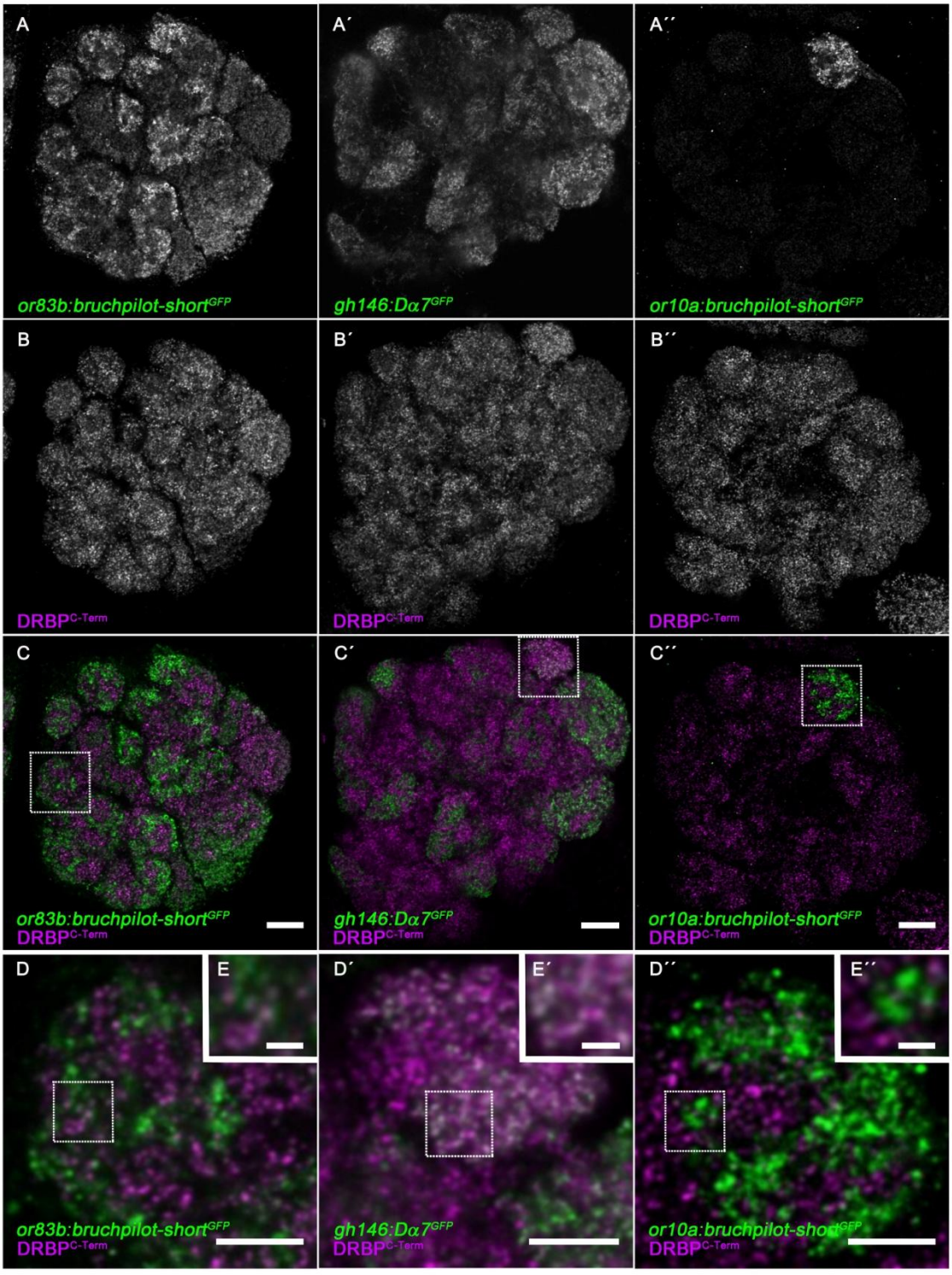
A
A´
A´´
or83b:bruchpilot-short^GFP
gh146:Dα7^GFP
or10a:bruchpilot-short^GFP
B
B´
B´´
DRBP^C-Term
C
C´
C´´
D
E
D´
E´
D´´
E´´

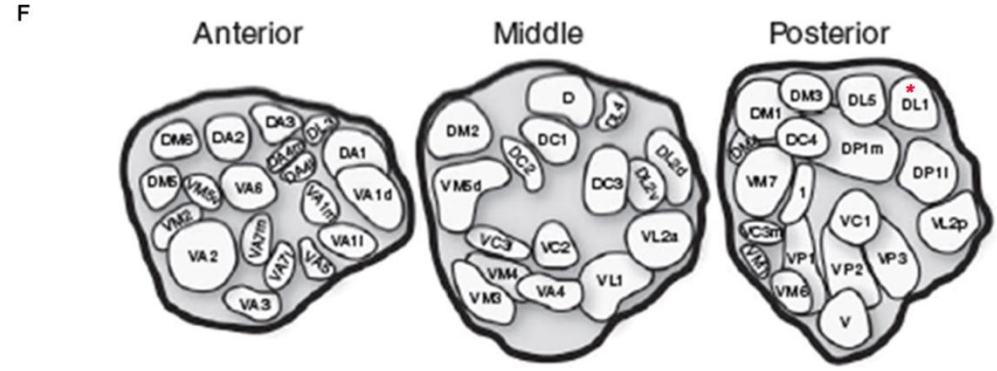
F
Anterior
Middle
Posterior
DM6
DA2
DA3
DA1
VA6
VA1d
VA2
VA3
D
DM2
DC1
DC2
DC3
VM5d
VL2a
VC3
VC2
VM4
VA4
VL1
VM3
DM3
DL5
DL1
DM1
DC4
DP1m
DP1l
VM7
VC1
VL2p
VP1
VP2
VP3
VM6
V

Fig. 4.22 Analysis of synaptic elements in the antennal lobe of adult flies.

Examination of the DRBP-rich synapses by mapping with different GAL4-drivers. (A-E) Projections of a major population of odorant receptor neurons (ORNs) visualized by *UAS-bruchpilot-short*^{GFP} expression with *or83b*-GAL4. *UAS-bruchpilot-short*^{GFP} and endogenous DRBP signals rarely overlapped, indicating that DRBP-positive synapses might not be abundantly present in ORNs. (A´-E´) Visualization of PSDs of PNs by *gh146*-GAL4 x Dα7^{GFP}. In the DL1 glomerulus in the posterior part of the AL, *gh146*-Dα7^{GFP}-positive synapses overlap with the DRBP signal. (A´´-E´´) AZs of ORNs in the glomerulus DL1. No overlap of *UAS-bruchpilot-short*^{GFP} and endogenous DRBP signal.
White dashed boxes in C, C´and C´´ indicate the area of interest shown at higher magnification in D, D´and D´´. The area of the inset shown at higher magnification in E, E´and E´´ is highlighted by white dashed boxes in D, D´and D´´, correspondingly. Scale bars in A-C, A´-C´and A´´-C´´: 10 µm; D, D´and D´´: 5 µm; insets E, E´and E´´: 1 µm.
(F) Antennal lobe (AL) model of 54 glomeruli of the left adult brain hemisphere, outlined in three sections, from anterior to posterior (taken from Chou et al., 2010). The DL1 glomerulus in the posterior part of the AL is highlighted by a red asterisk.

4.13.2 Identifying DRBP-rich synapses in PNs and KCs of adult flies

We wanted to know the localization of DRBP-rich synapses in the microglomeruli of the MB calyx, which contains discrete innervation sites of presynaptic terminals of PNs and claw-like dendrites of postsynaptic KCs. Therefore, we first mapped DRBP-positive synapses to PNs presynaptic termini by driving expression of *UAS-bruchpilot-short*^{GFP} using the *gh146*-GAL4 line (which drives expression in PNs). *UAS-bruchpilot-short*^{GFP} puncta were in very close proximity to the endogenous DRBP label in all the microglomeruli throughout the calyx (Fig. 4.23A-E). PN-AZs located to the inner edge of the microglomeruli, where DRBP can be detected. Thus, presence of DRBP at presynaptic termini of PNs could be validated. Next, we wanted to understand whether DRBP positive AZs are found juxtaposed to the postsynaptic densities of KC dendrites. This was done by co-labeling endogenous DRBP together with anti-GFP against *mb247-GAL4*::*UAS-Dα7*^{GFP} (Kremer et al., 2010; Christiansen et al., 2011). Endogenous DRBP label in the microglomeruli was not present in postsynaptic KCs dendrites (Fig. 4.23A´-E´), further supporting that DRBP is present at the presynaptic side of the PN-KC synapses. Next, we wanted to investigate whether DRBP-rich synapses are present at the presynaptic side of the KC synapses (KCs-AZs, Christiansen et al., 2011; see also Introduction section 2.3.5.1). Therefore we expressed *UAS-bruchpilot-short*^{GFP} by using the driver *mb247*-GAL4. Endogenous DRBP label was observed to overlap with the BRP punctae at the KC termini (Fig. 4.23A´´-E´´). This result confirmed the presence of DRBP signal at the presynaptic termini of KCs in the MB lobes. Similar to BRP, DRBP synapses are present at AZs of PNs and KCs.

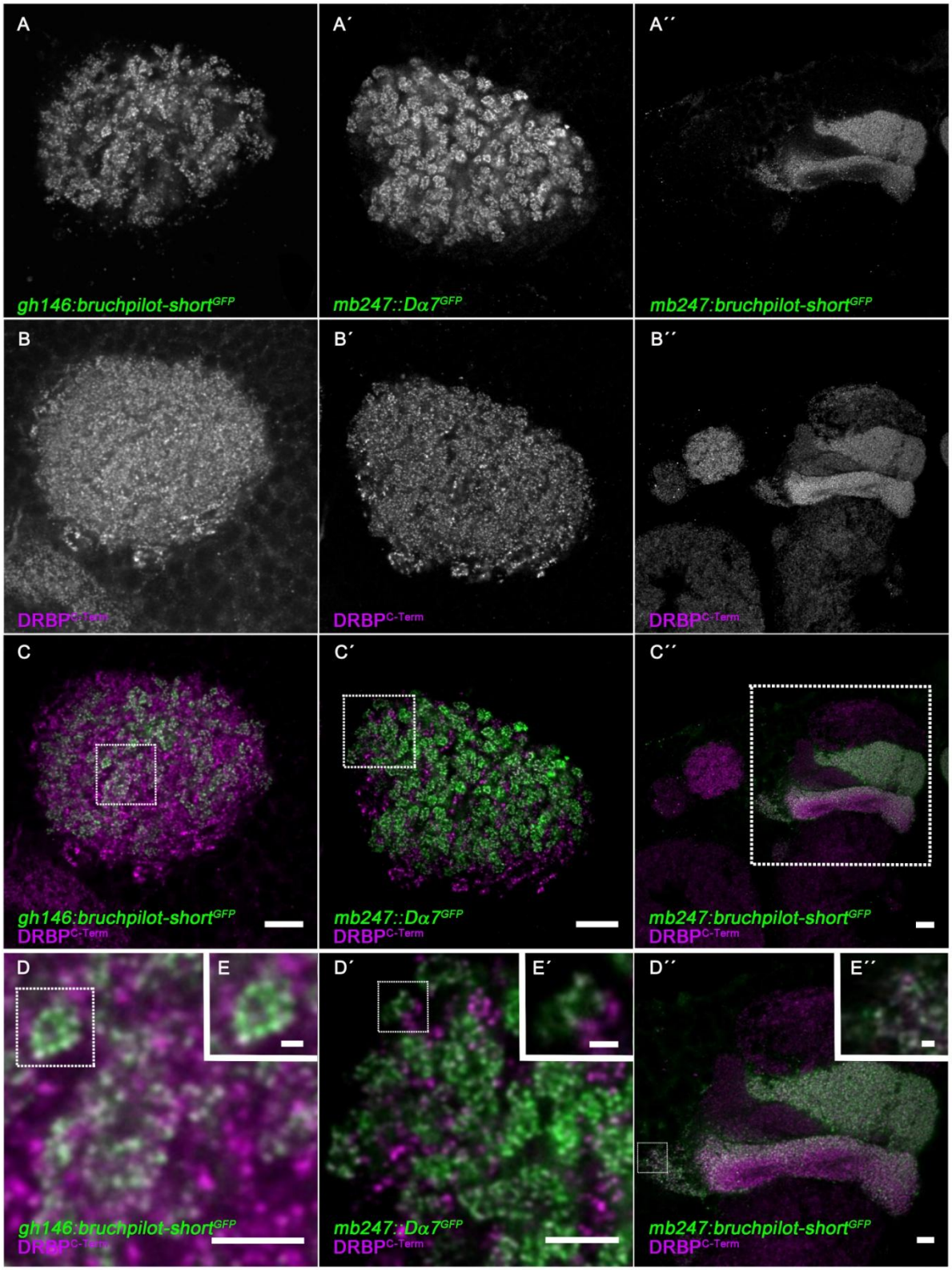

Fig. 4.23 Expression of DRBP at different synaptic elements of adult *Drosophila* calyx.

(A-E) Visualization of PN-AZs (*gh146*-GAL4 driving *UAS-bruchpilot-short*^{GFP}) and (A´-E´) cholinergic PSDs of KCs (*mb247*::dα7^{GFP}). (A-E) *UAS-bruchpilot-short*^{GFP} locates to the inner edge of the microglomeruli, juxtaposed to the DRBP signal (magenta). (A´-E´) Visualization of cholinergic PSDs of PNs (*mb247*::dα7^{GFP}) Endogenous DRBP label in the microglomeruli are not having close proximity to postsynaptic KCs dendrites (A´-E´), hence DRBP is present at the presynaptic side of the PN-KC synapses. (A´´-E´´) KC-expressed *UAS-bruchpilot-short*^{GFP} (*mb247*-GAL4) in MB lobes. The co-staining with the presynaptic AZ protein DRBP

(magenta) shows a clear overlap with the KC-derived Bruchpilot-short^{GFP} signal, suggesting that DRBP is present at AZs of KC-population. The white dashed box indicates the area of interest shown at higher magnification in D, D´ and D´´. The area of the inset shown at higher magnification in E, E´ and E´´ is highlighted by white dashed boxes in D, D´ and D´´, respectively. Scale bars in A-C, A´-C´ and A´´-C´´ equal 10 µm; in D, D´ and D´´ 5 µm; in insets E, E´ and E´´ 1 µm.

4.13.3 DRBP enrichment at the AZs of iLNs but not of eLNs in the AL

Endogenous DRBP is hardly detectable in the ORN axon termini (4.13.1). On the other hand, there is strong DRBP label in AZs found in the cores of AL glomeruli. What might be the neurons these DRBP rich AZs belong to? As interneurons (LNs) contribute strongly to the synapse population of the ALs, we addressed whether this observation might be due to an enrichment of DRBP-rich synapses in the presynaptic termini of LNs. Therefore, presynaptic sites of two major inhibitory LN1 and LN2 interneuron types were examined concerning them to be DRBP rich or not. *UAS-Bruchpilot-short*^{GFP} (labeling AZs) was expressed by using either *np1227*-GAL4 or *np2426*-GAL4. These ALs were then co-labeled with DRBP and Brp^{nc82} antibody (see Fig. 4.24A and A´). Similar to the observations in the report by Ito's group (Oakada et al., 2009), presynaptic sites of LN1s were found mainly in the core region of glomeruli (Fig. 4.24A) and evenly dispersed across glomeruli in the case of LN2s (Fig. 4.24A´). DRBP punctae were also observed to co-localize with the *UAS-bruchpilot-short*^{GFP} signal, when the latter was expressed in either of the two major unilateral iLN populations (LN1 and LN2) (Fig. 4.24B-F and 4.24B´-F´). We conclude that DRBP-rich synapses are found in these two major iLN populations.

To further validate this finding, GAL-4 drivers of five additional subpopulations of iLNs were used (Chou et al., 2010). *UAS-bruchpilot-short*^{GFP} was driven by *np3056*-GAL4, *lcch3*-GAL4 and *hb8-145*-GAL4 (Fig. 4.23), as well as by *hb4-93*-GAL4 and *np6277*-GAL4 (Fig. 4.26B-F and 4.26B´-F´). The number of LNs labeled by individual LN drivers used in this thesis and their corresponding neurotransmitter profiles are summarized in Table 2.1 in the Introduction section (data pooled from Okada et al., 2009; Chou et al., 2010). BRP punctae were in close proximity of the endogenous DRBP label in all the iLN subpopulations examined (Fig. 4.25, 4.26B-F and 4.26B´-F´). From these observations, we conclude that the DRBP signal is probably enriched at iLN synapses.

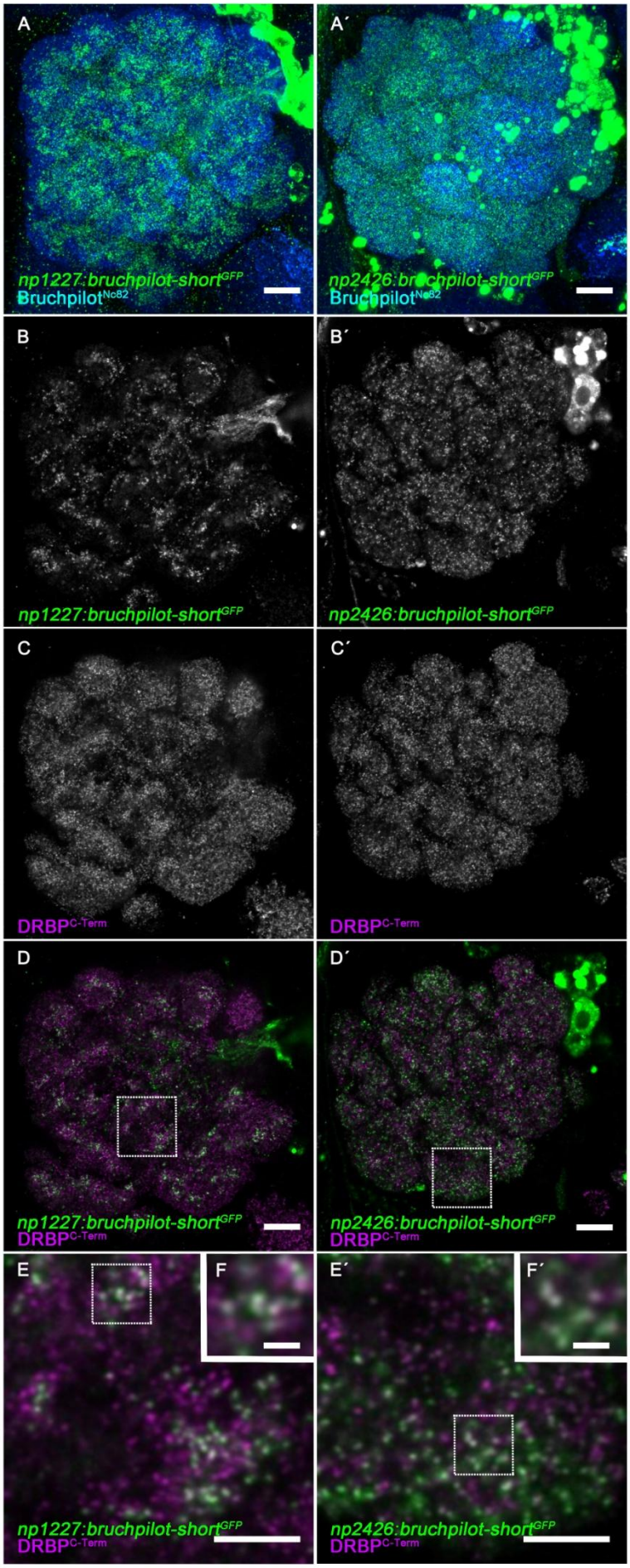
A
np1227:bruchpilot-short^GFP
Bruchpilot^Nc82
A´
np2426:bruchpilot-short^GFP
Bruchpilot^Nc82
B
np1227:bruchpilot-short^GFP
B´
np2426:bruchpilot-short^GFP
C
DRBP^C-Term
C´
DRBP^C-Term
D
np1227:bruchpilot-short^GFP
DRBP^C-Term
D´
np2426:bruchpilot-short^GFP
DRBP^C-Term
E
F
np1227:bruchpilot-short^GFP
DRBP^C-Term
E´
F´
np2426:bruchpilot-short^GFP
DRBP^C-Term

Fig. 4.24 Analysis of DRBP-positive synapses in two major populations of GABAergic (inhibitory) local interneurons (iLNs) in the adult antennal lobe.

(A-F) Visualization of type I iLN AZs (*np1227*-GAL4 driving *UAS-bruchpilot-short*^{GFP}) and (A´-F´) type II iLN AZs (*np2426*-GAL4 driving *UAS-bruchpilot-short*^{GFP}). (A), (A´) Overview of the expression pattern of iLN-derived Bruchpilot-short^{GFP} signal (green), co-stained with bruchpilot^{Nc82} (blue). The co-staining with the presynaptic AZ protein DRBP (magenta) shows a clear overlap with iLN-derived Bruchpilot-short^{GFP} signal (green) in both cases, suggesting the presence of DRBP at a population of iLN AZs. White dashed boxes indicate the area of interest shown at higher magnification in E, E´ and E´´. The area of the inset shown at higher magnification in F, F´ and F´´ is highlighted by white dashed boxes in E, E´ and E´´, respectively. Scale bars in A-D, A´-D´ and A´´-D´´ equal 10 µm; in E, E´ and E´´ 5 µm; in insets F, F´and F´´ 1 µm.

The next question was to address whether DRBP is also enriched at AZs formed by *excitatory* local interneurons (eLNs). For this experiment, we used *krasavietz*-GAL4 to express *UAS-bruchpilot-short*^{GFP}, and co-stained with DRBP$^{C\text{-}Term}$. Shang and colleagues described that about 2/3 of *krasavietz*-positive cells are eLNs and cholinergic in nature (Shang et al., 2007). However, studies conducted by Seki and colleagues (Seki et al., 2010) and Acebes *et al.* (Acebes et al., 2011) estimate a much lower percentage of only 10-20 % of eLNs to be labeled by this line. The proportion of eLNs to iLNs represented by this line therefore remains controversial. Probably the relative expression level of *krasavietz*-GAL4 in different subsets of cells also varies in strength, depending on the exact circumstances of the experiment. As the exact proportion of eLN population to iLNs represented by this line remains disputable, we assume that the *krasavietz*-GAL4 line used in our localization study features a mixed population of eLNs and iLNs (covers at least 10 % eLNs and 30 % iLNs, Seki et al., 2010). From the study, we observed that certain proportion of DRBP punctae co-localized (Fig. 4.26E´´-F´´) with GFP accordingly. Nonetheless, *krasavietz*-GAL4 definitely had, on average, less of an overlap with DRBP punctae than the pure iLN lines (Fig. 4.26B´´-F´´). This fits with the assumption that there is a share of iLNs in this line and is likely that the AZs that are not co-localizing with DRBP in this line represent eLN instructed AZs. Thus, we conclude that DRBP probably is not enriched at eLN AZs but highly enriched in iLN AZs. Taken together, these studies open up opportunities to further uncover the role of DRBP in both olfactory circuit and learning mechanisms.

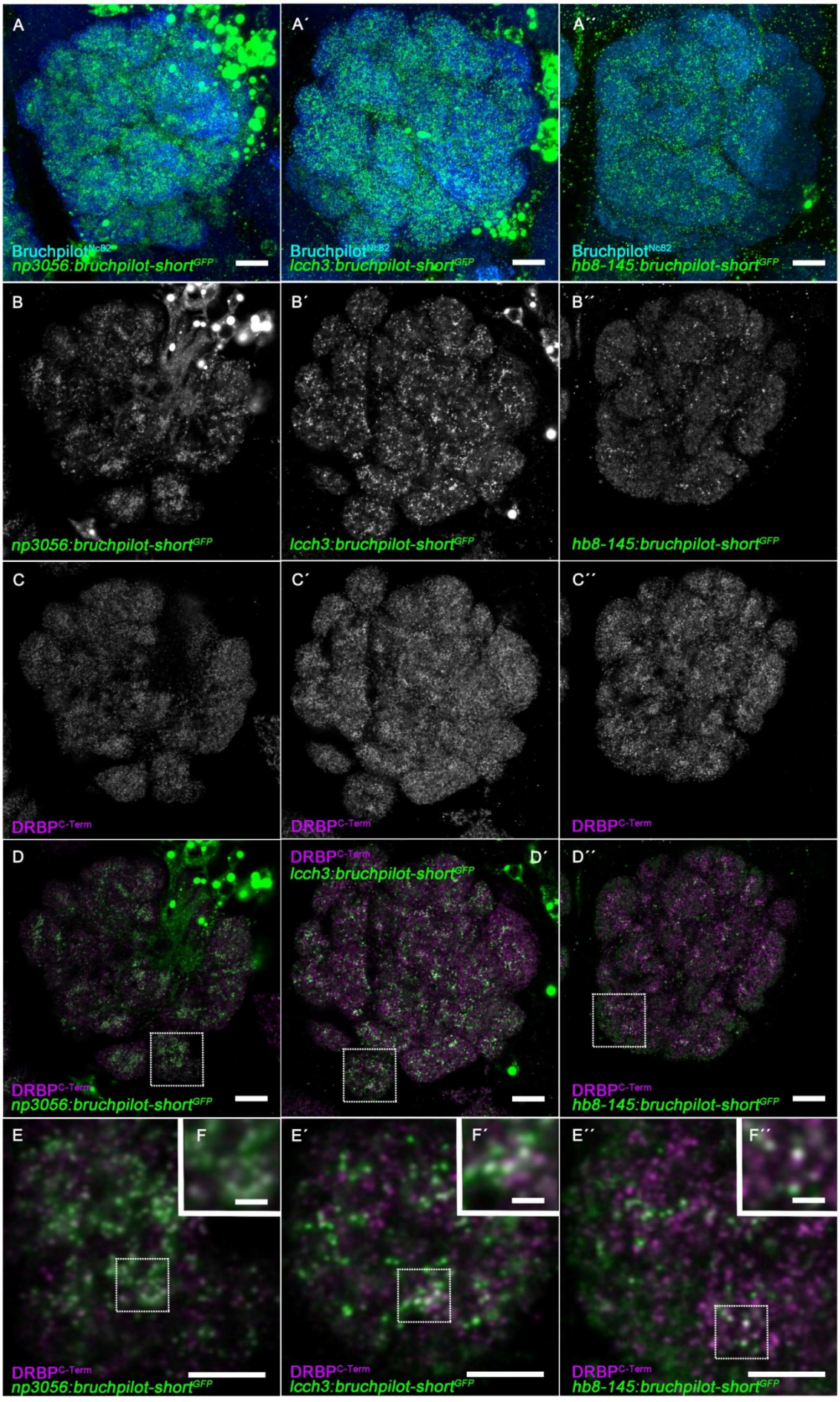
A
Bruchpilot^Nc82
np3056:bruchpilot-short^GFP
A´
Bruchpilot^Nc82
lcch3:bruchpilot-short^GFP
A´´
Bruchpilot^Nc82
hb8-145:bruchpilot-short^GFP
B
np3056:bruchpilot-short^GFP
B´
lcch3:bruchpilot-short^GFP
B´´
hb8-145:bruchpilot-short^GFP
C
DRBP^C-Term
C´
DRBP^C-Term
C´´
DRBP^C-Term
D
DRBP^C-Term
np3056:bruchpilot-short^GFP
DRBP^C-Term
lcch3:bruchpilot-short^GFP
D´
D´´
DRBP^C-Term
hb8-145:bruchpilot-short^GFP
E
F
DRBP^C-Term
np3056:bruchpilot-short^GFP
E´
F´
DRBP^C-Term
lcch3:bruchpilot-short^GFP
E´´
F´´
DRBP^C-Term
hb8-145:bruchpilot-short^GFP

Fig. 4.25 Analysis of DRBP-positive synapses in three subpopulations of GABAergic/inhibitory local interneurons (iLNs) in the adult antennal lobe.

Visualization of AZs in three subpopulations of iLNs. (A-F) *np3056*-GAL4 driving UAS-bruchpilot-short^{GFP}; (A´-F´), *lcch3*-GAL4 driving *UAS-bruchpilot-short^{GFP}*, and (A´´-F´´) *hb8-145*-GAL4 driving *UAS-bruchpilot-short^{GFP}*. iLN driver lines used in this study were kindly provided by Luo's lab (Chou et al., 2010). (A), (A´) and (A´´) Overview of expression patterns of the iLN subpopulation-derived Bruchpilot-short^{GFP} signal (green), co-stained with bruchpilot^{Nc82} (blue). Co-staining with the presynaptic AZ protein DRBP shows a clear overlap with the iLN-derived Bruchpilot-short^{GFP} signal, suggesting the existence of DRBP at AZs of a iLN population. White dashed boxes indicate the area of interest shown at higher magnification in E, E´ and E´´. The area of the inset shown at higher magnification in F, F´ and F´´ is highlighted by white dashed boxes in E, E´ and E´´, respectively. Scale bars in A-D, A´-D´ and A´´-D´´ equal 10 µm; in E, E´ and E´´ 5 µm; in insets F, F´and F´´ 1 µm.

Fig. 4.26 Analysis of DRBP-positive synapses in two other subpopulations of GABAergic iLNs and one mixed eLNs/iLN population in the adult antennal lobe.

Two more iLN subtype drivers, *hb4-93*-GAL4 and *np6277*-GAL4, were kindly provided by Luo's lab; Chou et al., 2010.
(A-F) Visualization of a subpopulation of iLN AZs (*hb4-93*-GAL4 driving *UAS-bruchpilot-short^{GFP}*) and (A´-F´) another group of GABAergic iLN AZs (*np6277*-GAL4 driving *UAS-bruchpilot-short^{GFP}*).
(A), (A´) Overview of the expression pattern of these two iLN subpopulations (Bruchpilot-short^{GFP} signal, green), co-stained with Bruchpilot^{Nc82} (blue). The co-staining with the presynaptic AZ protein DRBP (magenta) shows a clear overlap with these subpopulations, suggesting the presence of DRBP also at these iLN populations.
(A´´-F´´) Krasavietz-GAL4 drives the expression of UAS-bruchpilot-short^{GFP} in a mixed population of excitatory LNs (eLNs) and iLNs. (A´´) Overview of the expression pattern of eLN/iLN-derived Bruchpilot-short^{GFP} signal (green) co-stained with Bruchpilot^{Nc82} (blue). The mixed eLN/iLN derived Bruchpilot-short^{GFP} signal rarely overlaps with DRBP. White dashed boxes indicate the area of interest shown at higher magnification in E, E´ and E´´. The area of the inset shown at higher magnification in F, F´ and F´´ is highlighted by white dashed boxes in E, E´ and E´´, respectively. Scale bars in A-D, A´-D´ and A´´-D´´ equal 10 µm; in E, E´ and E´´ 5 µm; in insets F, F´and F´´ 1 µm.

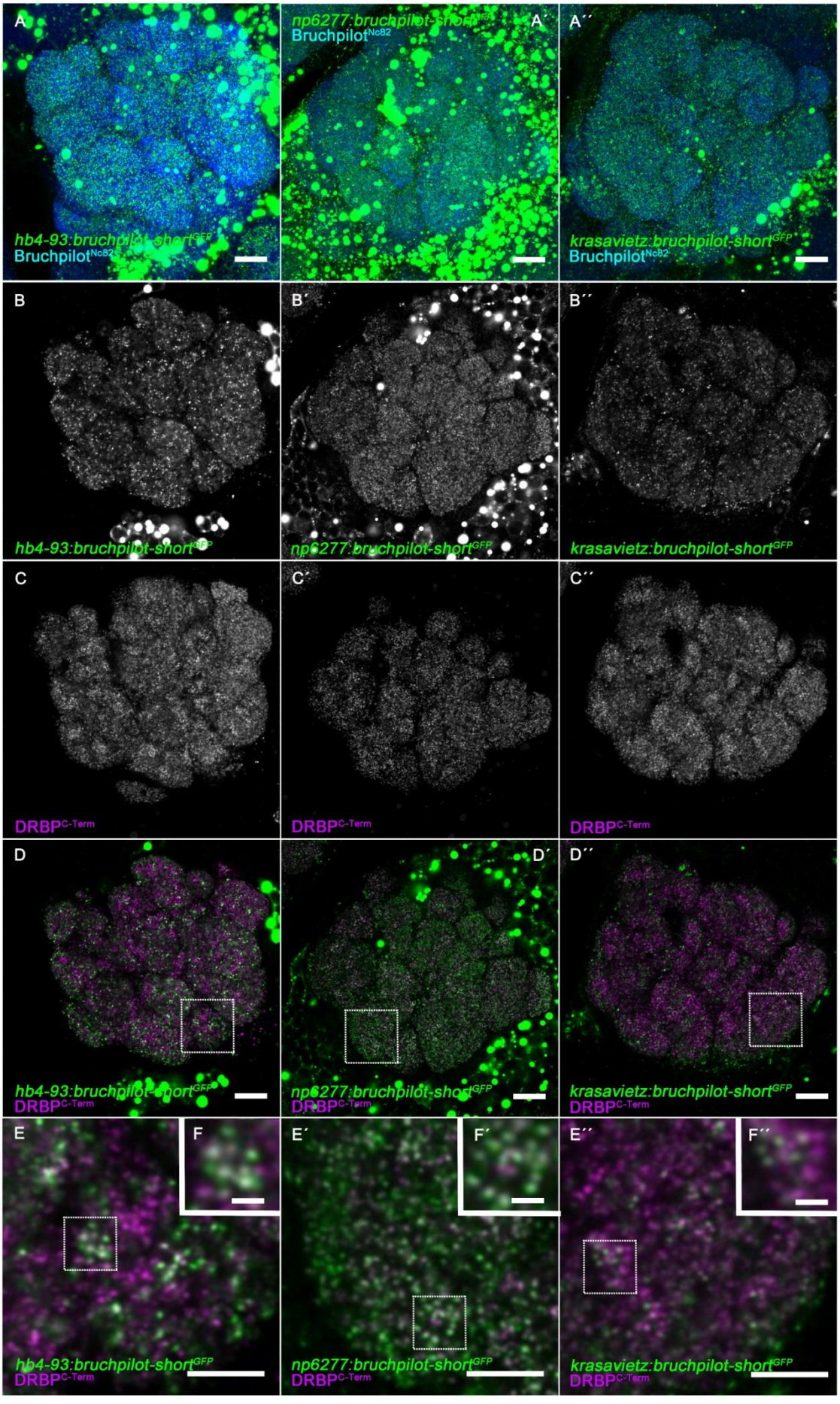
A
hb4-93:bruchpilot-short^GFP
Bruchpilot^Nc82
A´
np6277:bruchpilot-short^GFP
Bruchpilot^Nc82
A´´
krasavietz:bruchpilot-short^GFP
Bruchpilot^Nc82
B
hb4-93:bruchpilot-short^GFP
B´
np6277:bruchpilot-short^GFP
B´´
krasavietz:bruchpilot-short^GFP
C
DRBP^C-Term
C´
DRBP^C-Term
C´´
DRBP^C-Term
D
hb4-93:bruchpilot-short^GFP
DRBP^C-Term
D´
np6277:bruchpilot-short^GFP
DRBP^C-Term
D´´
krasavietz:bruchpilot-short^GFP
DRBP^C-Term
E
F
hb4-93:bruchpilot-short^GFP
DRBP^C-Term
E´
F´
np6277:bruchpilot-short^GFP
DRBP^C-Term
E´´
F´´
krasavietz:bruchpilot-short^GFP
DRBP^C-Term

5. Discussions

5.1 The RIM family of AZ proteins

Mammalian RIMs are one of the most examined presynaptic scaffolding proteins. It has been shown that RIMs are crucial to recruit Ca^{2+}-channels at the presynaptic AZ and facilitate SV docking at the presynaptic release sites (Kaeser et al., 2011; Han et al., 2011). α-RIM protein is the predominant isoform containing two nested domains in its N-terminal sequence suggested to regulate neurotransmitter release; it also includes two α-helices that bind to the GTP-binding vesicle protein Rab3 and a zinc-finger that interacts with the Munc13 C2A domain (Lu et al., 2006; Südhof and Rizo, 2011; Fig. 5.2). Binding of the RIM zinc-finger to the Munc13 C2A domain is of a higher affinity and is competitive with the homodimerization of the C2A domains; the presence of the RIM zinc-finger triggers conversion of the Munc13 C2A domain homodimer into a RIM/Munc13 heterodimer (Lu et al., 2006; Fig. 5.2). Notably, binding of RIM to Ca^{2+} is not mediated via any of the two C2 domains at the C-terminus (Wang et al., 2000). Only the AZ protein α-Liprin (Schoch et al., 2002) binds to the second RIM C2 domain (the C2B domain). A central PDZ domain of mammalian RIM (upstream of the first C2 domain) mediates the binding to ELKS proteins and Ca^{2+}-channels (Wang et al., 2000; Ohtsuka et al., 2002; Kaeser et al., 2011; Fig. 5.2).

Functionally, RIM performs at least two essential roles: (1) it regulates the priming activity of Munc13 (Deng et al., 2011) as RIM deletions produce a severe priming defect (Koushika et al., 2001; Schoch et al., 2002); this function is believed to be mediated through the RIM zinc-finger alone (Deng et al., 2011). (2) RIM proteins cluster Ca^{2+}-channels to the AZ, allowing tight coupling of Ca^{2+} influx to triggering of SVs fusion (Kaeser et al., 2011). The binding of Rab3A on SVs to RIM1α in the AZ would also suggest a SV docking function (Wang et al., 1997, 2000; Wang and Südhof, 2003), but the number of docked vesicles is unaffected in RIM1α (Schoch et al., 2002) and Rab3A knockout mice (Geppert et al., 1997).

5.1.1 Synaptic role of RIM at NMJ

To prepare for a thorough analysis of RIM function at the *Drosophila* NMJ, we subjected the *rim* locus to genetic analysis in *Drosophila*. In our system, "self-made" alleles ($rim^{ex.1.26}$, rim^{del103}) and available intragenic *rim* alleles (rim^{Minos}) showed partially reduced adult vitality and locomotion activity (Table 4.1 and Fig. 4.8). The likely hypomorphic allele $rim^{ex.1.26}$ removes the second C2 domain of RIM that is proposed to interact with another AZ protein,

Liprin-α. Liprin-α is a key component in synapse formation, as described in several model systems (Kaufmann et al., 2002; Dai et al., 2006; Olsen et al., 2005; Patel et al., 2006) and localization of SVs at the AZ via Syd-2/Liprin and unc-10/RIM-dependent interactions in *C. elegans* was recently described (Stigloher et al., 2011). In *Drosophila*, Liprin-α is AZ associated and serves an important function in efficient AZ formation; Liprin-α/DSyd-1 accumulations are important during early stages of AZ assembly (Fouquet et al., 2009; Owald et al., 2010). However, the hypomorphic allele $rim^{ex.1.26}$ showed only a mild phenotype even though the interaction with Liprin-α should be abolished. Our longest intragenic RIM allele, rim^{del103} removes an additional short proline-rich sequence that is predicted to interact with RIM-BPs (RIM-binding proteins; Wang et al., 2000), upstream of the second C2 domain (the C2B domain). This mutant also appeared to be "healthy" even though the binding to RIM-BP should be affected. We propose that residual RIM protein (Rab3 binding, zinc-finger, PDZ domains and the first C2 domain) expressed in the RIM hypomorphs may be already sufficient to localize to AZs, via interactions with Ca^{2+}-channels and ELKS through the PDZ domain; the interactions with Rab3 and Munc-13 via the N-terminal domains (Rab3 binding and zinc-finger domains) are not physically interrupted. Certain functional deficits of the RIM hypomorph rim^{del103} were revealed in collaboration with the group of Graeme Davis and will be discussed in the following sections (Müller et al., in review).

At mammalian synapses it was demonstrated that RIM1/2 isoforms participate in the control of synaptic transmission by electrophysiological analysis (Wang et al., 1997; Castillo et al., 2002; Schoch et al., 2002; Mittelstaedt et al., 2010). *Drosophila* RIM was revealed to have an evolutionarily conserved function in *Drosophila* by participating in establishing normal baseline synaptic transmission (Müller et al., in review). The rim^{del103} hypomorph displayed deficits in presynaptic release probability by having a decreased EPSC amplitude and an increase in facilitation (Müller et al., in review). However, the rim^{del103} hypomorph NMJ were able to restore baseline *evoked junctional current* (EJC) amplitude upon prolonged stimulation (Müller et al., in review). We propose that a normal number of functional AZs is associated with a decreased numbers of presynaptic Ca^{2+}-channels (Müller et al., in review).

Direct interaction of RIM with presynaptic voltage-gated N- and P/Q-type Ca^{2+}-channels is mediated via the PDZ domain in mammals (Wang et al., 2000; Kaeser et al., 2011) and Ca^{2+}-channels recruitment to AZs was shown to be RIM-dependent (Kaeser et al., 2011). Similar to the molecular mechanism observed in mammals, *Drosophila* RIM participates in recruiting

Ca^{2+}-channels to AZs. A decreased number of cac-GFP label (Ca^{2+}-channels clustered) at *rim* mutant NMJs was observed and therefore RIM is required for normal Ca^{2+}-channel density at NMJs (Graf et al., co-submitted manuscript). Presynaptic Ca^{2+} influx was slightly impaired also in rim^{del103} (Müller et al., in review), though this defect has a milder magnitude compared to a double knockout of RIM1 and RIM2 in mice (around 50% reduction) (Han et al., 2011). The rim^{del103} hypomorph displayed a defect downstream of Ca^{2+} influx by having a larger average distance between Ca^{2+}-channels (sites of Ca^{2+} influx) and SVs (Müller et al., in review), consistent with the finding that RIM has also been implicated in vesicle priming/docking in mammalian central synapses (Koushika et al., 2001; Schoch et al., 2002).

RIM as a putative effector of Rab3 GTPase signaling may also be centrally involved in presynaptic AZ architecture and synaptic plasticity (Wang et al., 1997). Rab3 plays a pivotal regulatory role in the AZ assembly and loss of Rab3 dramatically changes the BRP distribution at AZ at the fly NMJ (Giagtzoglou et al., 2009; Graf et al., 2009). Unlike Rab3, the *rim* allele (*piggyBac* insertion, PBac[3HPy+]RimC165) did not alter synaptic growth or appearance at the fly NMJ (Müller et al., in review).

5.1.2 RIM is central to homeostatic plasticity at the NMJ

The rim^{del103} allele was revealed to be a strong hypomorphic allele in maintaining proper homeostatic plasticity at the NMJ (Müller et al., in review). Homeostatic signaling systems are thought to stabilize neural function through the regulation of ion channel density, neurotransmitter receptor abundance and presynaptic neurotransmitter release (Davis, 2006; Dickman and Davis, 2009). Application of sub-blocking concentrations of philanthotoxin (PhTX, 4-20 µM) to the *Drosophila* NMJ induces a homeostatic potentiation of synaptic transmission (Frank et al., 2006). A compensatory increase in action potential-evoked presynaptic vesicle release precisely offsets the postsynaptic perturbation (decrease in mEPSP amplitude) and restores muscle excitation in the continued presence of the perturbation (mEPSP amplitude back to baseline levels) in wild-type animals (Davis, 2006; Dickman and Davis, 2009; Müller et al., 2011). RIM is dispensable for the homeostatic enhancement of presynaptic Ca^{2+} influx without a corresponding homeostatic enhancement of vesicle release (Müller et al., in review). The blockade of homeostatic plasticity in *rim* mutants was not caused by a defect in the homeostatic increase in Ca^{2+} influx. The change in Ca^{2+} influx is one part of the mechanisms that achieves the resultant homeostatic plasticity (Müller et al., in review). They further demonstrated that *rim* is specifically required (Müller et al., in review)

in the downstream modulation of another genetically separable process, the readily-releasable vesicle pool (RRP) (Schneggenburger et al., 1999; Weyhersmüller et al., 2011). There was no significant increase in SV pool size in *rim* mutants upon PhTX application, whereas this led to a significant increase in the number of the RRP at wild type synapses under PhTX treatment (Müller et al., in review; Weyhersmuller et al., 2011). This data was similar to the findings in RIM1/2 double knockout mice (Han et al., 2011).

5.2 DRBP is a novel component of the AZ cytomatrix

Our group is interested in studying novel AZ cytomatrix proteins apart from Ca^{2+}-channels and the BRP matrix. We thus started to address the only *Drosophila* homologue of RIM-BP, (Schoch and Gundelfinger, 2006; Jin and Garner, 2008), while no functional data were available for mammalian species. Mammalian RIM-BPs were only shown to interact with Ca^{2+}-channels and to be enriched at presynaptic terminals (Hibino et al., 2002; Wang et al., 2000; Mittelstaedt and Schoch, 2007). Intragenic *drbp* mutants were produced and subjected to genetic analysis in our model system. An intragenic *drbp* hypomorph ($drbp^{Minos}$/*Df*) exhibited lower adult hatching rate (Table 4.2), markedly reduced larval locomotion (Fig. 4.14) and two thirds reduction in $DRBP^{C\text{-}Term}$ immunoreactivity at NMJ (Fig. 2A in Liu et al., 2011). DRBP EMS STOP alleles (see Fig. 4.12 for detail positions) over *Df* showed severely reduced adult hatching rate (Table 4.2) and mutant larvae barely moved (Fig. 4.14). Immunoreactivity for DRBP N- (Fig. S4 in Liu et al., 2011) or C-Term antibodies (Fig. 2A in Liu et al., 2011) was completely absent at mutant larval NMJs. Bruchpilot spots and postsynaptic glutamate receptors (GluRs) in *drbp* null mutants appeared largely unaltered. Mutant larval NMJ terminals reached normal morphological size and Bruchpilot-positive AZs juxtaposed to postsynaptic glutamate receptor fields (Fig. 2B in Liu et al., 2011). One copy of the genomic transgene encompassing the entire *drbp* locus (Rescue, see Fig. 4.13A) partially restored NMJ staining in $drbp^{STOP1}$ null (Fig. 2A in Liu et al., 2011) and partially rescued $drbp^{Minos}$ and $drbp^{STOP1\text{-}3}$ larval vitality (Fig. 4.14).

5.2.1 Structural organization and synaptic roles of DRBP at the AZ

DRBP was first shown to tightly localize to presynaptic sites. Its close proximity to BRP suggests that both components often cooperate physically to build up a highly dedicated AZ architecture (see model in Fig. 5.1; Fig. 1 in Liu et al., 2011). AZ ultrastructural (STED microscopy) analysis revealed that $DRBP^{C\text{-}Term}$ localizes more towards the AZ center than BRP^{Nc82}. DRBP N- and C-Term labels are similarly distributed and do not display an

elongated conformation as observed for BRP (Fouquet et al., 2009). Ca^{2+}-channels localize beneath the scaffold formed by DRBP in the AZ center since $DRBP^{C\text{-}Term}$ was shown to tightly encircle Ca^{2+}-channels. Ultrastructural analysis by EM emphasized a role for DRBP in proper AZ cytomatrix assembly (Fig. 4.15), as the structural integrity of the cytomatrix was severely disrupted in *drbp* nulls (Fig. 4.15). No regular T bar formed in *drbp* nulls and free-floating electron-dense material was regularly observed, likely being detached from the AZ plasma membrane (Fig. 4.15). Thus, together with BRP (T bar component, Kittel et al., 2006), we found DRBP to be another crucial building block of the AZ central cytomatrix.

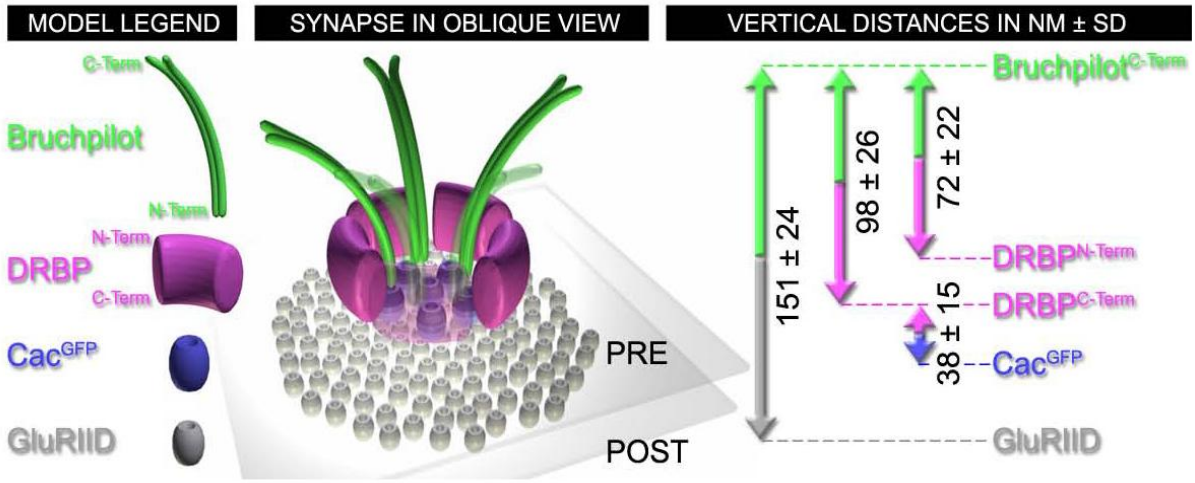

Fig. 5.1 A model of an AZ at *Drosophila* NMJ synapses.

GluR = glutamate receptor, PRE = presynaptic, POST = postsynaptic, SD = standard deviation (taken from Liu et al., 2011).

In functional terms, DRBP is critical in maintaining proper synaptic transmission as nearly a complete abolishment of eEJC in *drbp* null larvae was observed (Fig. 4.16). In fact, quantification of the number of quanta (i.e. SVs) released per individual action potential (quantal content, Fig. 4.16D) showed a severe reduction here. Slightly but significantly reduced numbers of membrane-proximal SVs (up to 5 nm distance) counted over the whole AZ were observed in $drpb^{STOP1}$ animals (EM analysis, Fig. 4.15B). Thus, the release defect of *drbp* null might in parts be explained by a deficit of establishing proper numbers of SVs at the AZ membrane. Moreover, DRBP obviously plays a crucial role in maintaining proper release probability of SVs. In fact, the strong facilitation (more than double the initial eEJCs amplitude) (Fig. 4A in Liu et al., 2011) observed for *drbp* null synapses points towards a severe reduction of presynaptic release probability in this mutant. AZ size or AZ numbers per NMJ terminal appear unchanged at the same time (Fig. 2B in Liu et al., 2011). The core

fusion machinery is still operational in *drbp* mutant NMJs as they have the capacity to release large numbers of SVs during a stimulus train when intracellular calcium is sufficiently elevated (Fig. 4C in Liu et al., 2011).

We hypothesize that a normal number of functional AZs may be associated with a decreased numbers of Ca^{2+}-channels clustered on the presynaptic membrane. This is supported by the slightly reduced AZ Ca^{2+}-channel density (25 %) and intensity (36 %) detected in *drbp* nulls (Fig. 4F in Liu et al., 2011). Presynaptic spatially averaged Ca^{2+} signal was also reduced by 32±4 % in $drbp^{STOP1}$ mutants in response to single action potentials (Fig. 4E in Liu et al., 2011). This dramatic reduction in SV release probability for single action potentials might mainly be due to defects in processes upstream of the SV fusion. The eEJC rise time of *drbp* mutants was slightly but significantly delayed when compared to controls, whereas mEJC rise time was unchanged (Fig. 4D in Liu et al., 2011). Evoked vesicle fusion events in *drbp* mutants appeared de-synchronized with the invasion of the presynaptic terminal by an action potential. The observed synchronization impairment probably also due to the reduction in the abundance of Ca^{2+} channels and the reduced Ca^{2+} influx/ levels in the nerve terminal (Fig. 4E, F in Liu et al., 2011). The spatiotemporal pattern of action potential-triggered Ca^{2+} influx into the nerve terminal is also critical for this synchronization deficit (Neher and Sakaba, 2008).

5.2.2 Possible structural/functional relationship between DRBP, Ca^{2+}-channels and other AZ proteins

Of note, "structural" deficits in AZ cytomatrix organization and Ca^{2+}-channel clustering were more pronounced in *bruchpilot* (Kittel et al., 2006; Fouquet et al., 2009) than *drbp* mutants. Bruchpilot levels were unaffected in *drbp* mutant NMJ (Fig. 2A in Liu et al., 2011), while DRBP levels were clearly reduced in *bruchpilot* mutants (Fig. S6 in Liu et al., 2011). Deficits in *bruchpilot* mutants might thus at least partially be explained by a concomitant loss of AZ-localized DRBP. DRBP probably serves functions beyond the structural and Ca^{2+}-channel clustering roles of Bruchpilot. Both *drbp* (Liu et al., 2011) and *bruchpilot* null phenotypes (Kittel et al., 2006; Fouquet et al., 2009) are functionally similar by demonstrating decreased and asynchronous evoked release with strong atypical short-term facilitation. However, *drbp* nulls show much severer evoked SV release deficits (5 %) at conditions where *bruchpilot* nulls still retain 30 % of evoked release (Kittel et al., 2006; Liu et al., 2011). RIM-BP family proteins might thus be prime organizers in the coupling of SVs, voltage-gated Ca^{2+} channels

and the SV fusion machinery since a partial loss of DRBP is sufficient to cause a significant reduction in SV release.

For biochemical interaction, binding of mammalian RIM-BPs to RIM had been first described in Wang et al., 2000 (based on yeast two-hybrid and GST pull-down assays). Later findings (Hibino et al., 2002; Kaeser et al., 2011) further demonstrated interactions of RIM-BPs with Ca^{2+}-channels (see model in Fig. 5.2). RIM PDZ-domain directly binds to the C-terminus of N- and P/Q-type Ca^{2+}-channels and indirectly binds via the RIM-BP SH3 domain to a PXXP motif in the cytoplasmic tail of the Ca^{2+}-channels (Kaeser et al., 2011; Fig. 5.2). DRBP binds to both the *Drosophila* homologue of AZ protein RIM and the α1 subunit Cacophony (Cac) (Liu et al., 2011). Interactions were specifically mediated by highly homologous PXXP motifs of RIM and Ca^{2+}-channels with the third DRBP SH3 domain (Fig. S7 in Liu et al., 2011).

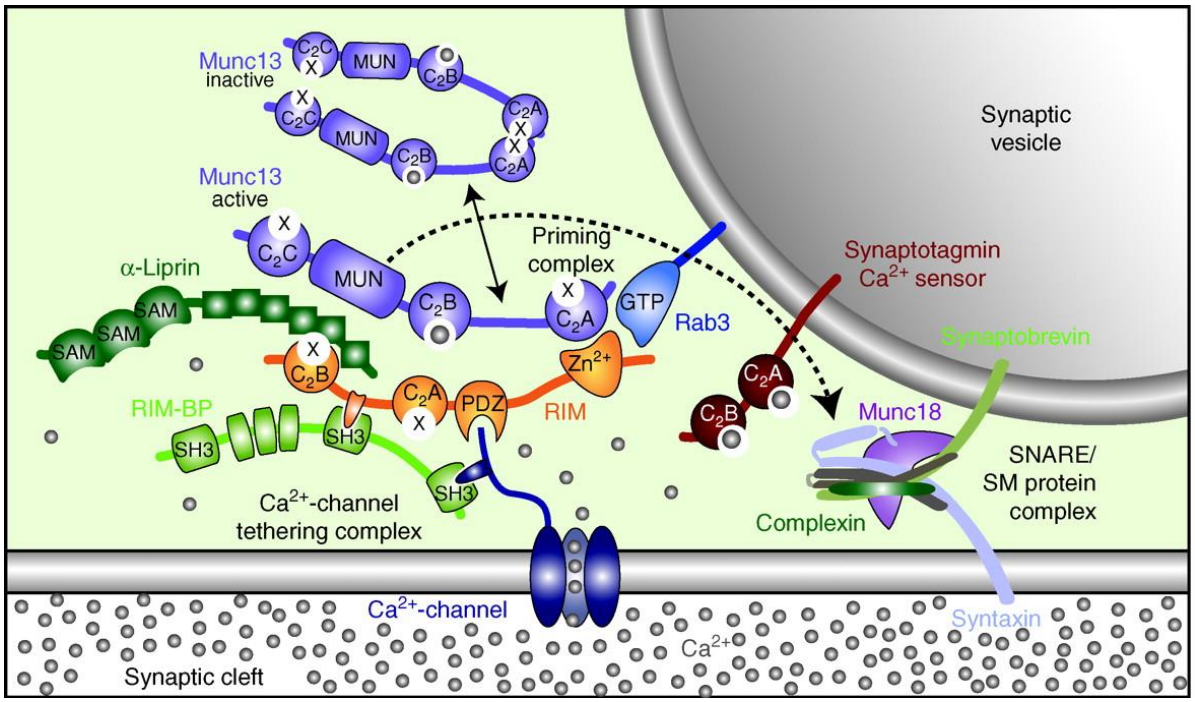

Fig. 5.2 A model of an AZ at mammalian synapses.

Structural organizations of four canonical components of AZs (Munc13, α-liprins, RIMs, and RIM-BPs) with corresponding interactive domains are illustrated (taken from Südhof and Rizo, 2011).

DRBP protein is crucial for synaptic transmission by acting as a building block of the CAZ and subsequent tethering of Ca^{2+}-channels to AZs, connecting the Ca^{2+}-channels to SVs (Liu et al., 2011). These findings add new complexity to the existing knowledge about AZ scaffolding proteins in which DRBP also serves similar functions as mammalian RIM. RIM was traditionally believed to be the central element of AZ since a selective loss of Ca^{2+}-channels from presynaptic specializations and a decrease in action potential induced Ca^{2+}

influx were observed in RIM 1/2 knockout (Kaeser et al., 2011). However, this deficit can already be compensated by introduction of RIM fragments containing only the PDZ-domain and the RIM-BP binding sequence (Kaeser et al., 2011), thus this result implicates these critical processes might be highly RIM-BPs-dependent. Quantitative mass spectrometry was used for comprehensive analysis of the molecular nano-environments of the Cac-homologous voltage-gated Ca^{2+} (Cav) channels in rodent brain (Müller et al., 2010). RIM-BP 2 was found in a stochiometry equal to established subunits ($\alpha 2\delta$, β) of the Cav complexes (Dolphin et al., 2009) but higher notably than observed for RIM (Müller et al., 2010). GST pull-down assays indicated the levels of RIM-BP remain unaffected in brain tissues from both heterozygous and homozygous RIM1 knockout mice (Wang et al., 2000). Both mouse RIM 1/2 double knockouts (Kaeser et al., 2011; Han et al., 2011) as well as the *Drosophila rim* mutant, rim^{del103} (Müller et al., in review), show a moderate reduction of SV release in comparison to the dramatic *drbp* null phenotype. Thus, DRBP might not exclusively organize RIM-dependent functions or act necessarily downstream of RIM. We propose that RIM's function might even be downstream of DRBP and - in an extreme scenario - RIM might only be a part of the DRBP phenotype.

We showed that the interactions with PXXP motifs of both Ca^{2+}-channels and RIM can be mediated via the third DRBP SH3 domain in this study (Liu et al., 2011). As a multi-domain scaffold protein, DRBP might bundle multiple interactions among diverse AZ proteins. Hence, it is of high relevance to identify additional interactive partners for the rest of the functional domains. Deeper understanding of the interplay of DRBP with various AZ proteins (RIM, α-liprins, Munc-13, BRP) also becomes critically interesting. Studying the functional relationship with Munc-13 may shed light on the essential role of DRBP in SV priming/docking.

5.2.3 DRBP in the adult CNS synpases

In the course of this study, we have used synapses in the adult CNS as an additional model system to understand the AZ composition and possible synaptic role of DRBP. A neuropile-specific labeling of $DRBP^{C\text{-}Term}$ antibody at adult CNS synapses was confirmed (Fig. 4.17); $Bruchpilot^{Nc82}$ levels in the $drbp^{Minos}$ hypomorphic allele remained unaltered.

5.2.3.1 AZ composition diversity in the adult fly CNS

We found that the CAZ protein composition is highly diversified regarding the relative amounts of DRBP and BRP (Fig. 4.18 and 4.19). A different degree of CAZ composition diversity was observed between neuropiles such as the AL (Fig. 4.19B) and the MB (Fig. 4.19C). In the AL, DRBP-rich synapses preferentially concentrated in the core areas of AL glomeruli, while Bruchpilot^{Nc82} label appeared to be low at these synapses (Fig. 4.19B). This may be explained by a high enrichment of DRBP at the iLNs-AZs (Fig. 4.24, 4.25, 4.26A-E and 4.26A´-E´) and the much lower endogenous DRBP at ORNs-AZs (Fig. 4.22A-E).

In the MB, the DRBP$^{N\text{-}Term}$ (all MB lobes) and DRBP$^{C\text{-}Term}$ (α/β MB lobes) staining are preferentially enriched in KCs of the wild-type adult brain (Fig. 4.18). This finding might implicate the involvement of DRBP in the processing of olfactory signals in the adult CNS. Several proteins that serve a vital role in olfactory learning and memory are preferentially enriched and expressed in the MB lobes (Crittenden et al., 1998). A recent report also suggested that BRP is required for olfactory memory and that its presence in KCs is relevant for anesthesia-resistant memory (Knapek et al., 2011). DRBP, as an essential building block of the presynaptic CAZ, might, together with BRP, also take part in such olfaction-associated processes. Hence, the DRBP-RNAi construct could be an important tool to understand the role of DRBP within KCs in olfactory processes.

5.2.3.2 Assigning identity to synapse classes

We intended to assign identities of DRBP to particular neuronal populations in the fly olfactory system to further understand the CAZ composition diversity. DRBP was present and co-localized with BRP within AZs in the PN (Fig. 4.23A-E) and KC synapses (Fig. 4.23A´´-E´´). Understanding whether DRBP is also present at the KCACs of KCs would be of particular interest in the future since they are candidate sites for memory trace formation during olfactory learning (Christiansen et al., 2011).

The DRBP signal did not concentrate at eLN synapses (Fig. 4.26A´´-E´´) but is highly enriched at presynaptic terminals of iLNs (Fig. 4.24, 4.25, 4.26A-E and 4.26A´-E´). We also made similar observations in a project that aimed at assigning synaptic identities to diverse neuronal populations based on the relative expression levels (ratios) of different AZ markers (Bruchpilot^{Nc82}, Bruchpilot$^{N\text{-}Term}$, DRBP$^{C\text{-}Term}$ and DSyd-1), together with Till Andlauer and colleagues (Andlauer et al., in preparation). In this study, we found a relative enrichment of

DRBP in synapse populations identified by *np1227*-GAL4-derived *UAS-bruchpilot-short*^{GFP} expression in antennal lobes (n=8, LN1 population). These two independent experiments together strongly suggest that DRBP is highly enriched at iLNs. Future DRBP-RNAi knockdown experiments may give us further confirmation of this observation; we plan to examine whether the relative enrichment of DRBP in iLNs can be reduced by expressing the *drbp* RNAi using the LN1 (*np1227*-GAL4) driver. The relative enrichment of DRBP in *krasavietz*-GAL4 positive neurons, found in the ratio project (Andlauer et al., in preparation), fits well together with the hypothesis that this driver line has a mixed population of iLNs and eLNs: There is a relatively lower enrichment of DRBP at synapse populations positive for *krasavietz*-GAL4 in the AL (n=8, iLNs/eLNs populations) than for *np1227*-GAL4, implicating as well that DRBP is not particularly enriched in eLNs covered by *krasavietz*-GAL4.

In the ratio project also a mutant was used to analyze synaptic diversity of certain AZ markers (Andlauer et al., in preparation), the well-characterized *shakB* (shaking-B, gap junctions) mutant (Yaksi and Wilson, 2010). In this mutant all electrical synaptic transmission between eLNs and PNs is eliminated; synapses between eLNs and iLNs as well as in between PNs are also affected, but synaptic transmission between iLNs is assumed to remain unaffected (Yaksi and Wilson, 2010). Preliminary results indicate that DRBP levels are relatively stable in this mutant (n=5-8 for *shakB*^{2} and controls, respectively). This finding fits to our hypothesis that DRBP is mainly enriched at iLNs, since the *shakB* mutant should not affect presynapses of iLNs. Sample sizes in this study will be increased to further validate these findings. Taken together, all these observations point into the direction that DRBP is highly enriched at iLN synapses and rather not at eLN synapses within the AL.

6. References

Aberle H, Haghighi AP, Fetter RD, McCabe BD, Magalhães TR & Goodman CS (2002) wishful thinking encodes a BMP type II receptor that regulates synaptic growth in *Drosophila*. *Neuron* **33:** 545-558

Acebes A, Martín-Peña A, Chevalier V & Ferrús A (2011) Synapse loss in olfactory local interneurons modifies perception. *Journal of Neuroscience* **31:** 2734-2745

Albin SD & Davis GW (2004) Coordinating structural and functional synapse development: postsynaptic p21-activated kinase independently specifies glutamate receptor abundance and postsynaptic morphology. *Journal of Neuroscience* **24:** 6871-6879

Andlauer TFM, Liu KS, Steckhan N, Zube C & Sigrist SJ. A RATIOnal approach to synapse diversity of the *Drosophila* brain. In preparation

Aso Y, Grübel K, Busch S, Friedrich AB, Siwanowicz I & Tanimoto H (2009) The mushroom body of adult *Drosophila* characterized by GAL4 drivers. *Journal of Neurogenetics* **23:** 156-172

Atwood HL, Govind CK & Wu CF (1993) Differential ultrastructure of synaptic terminals on ventral longitudinal abdominal muscles in *Drosophila* larvae. *Journal of Neurobiology* **24:** 1008-1024

Atwood HL & Karunanithi S (2002) Diversification of synaptic strength: presynaptic elements. *Nature Reviews Neuroscience* **3:** 497-516

Augustin I, Rosenmund C, Südhof TC & Brose N (1999) Munc13-1 is essential for fusion competence of glutamatergic synaptic vesicles. *Nature* **400:** 457-461

Bellen HJ, Vaessin H, Bier E, Kolodkin A, D'Evelyn D, Kooyer S & Jan YN (1992) The *Drosophila* couch potato gene: an essential gene required for normal adult behavior. *Genetics* **131:** 365-375

Bellen HJ, Levis RW, Liao G, He Y, Carlson JW, Tsang G, Evans-Holm M, Hiesinger PR, Schulze KL, Rubin GM, Hoskins RA & Spradling AC (2004) The BDGP gene disruption project: single transposon insertions associated with 40% of *Drosophila* genes. *Genetics* **167:** 761-781

Bellen HJ, Levis RW, He Y, Carlson JW, Evans-Holm M, Bae E, Kim J, Metaxakis A, Savakis C, Schulze KL, Hoskins RA & Spradling AC (2011) The *Drosophila* gene disruption project: progress using transposons with distinctive site specificities. *Genetics* **188:** 731-743

Bennett MR (1999) The early history of the synapse: from Plato to Sherrington. *Brain Research Bulletin* **50:** 95-118

Benton R (2006) On the ORigin of smell: odorant receptors in insects. *Cellular and molecular life sciences CMLS* **63:** 1579-1585

Benton R (2009) Molecular basis of odor detection in insects. *Annals Of The New York Academy Of Sciences* **1170:** 478-481

Berg DE & Howe MM (1989) Mobile DNA. American Society of Microbiology, Washington, D.C.

Berghammer AJ, Klingler M & Wimmer EA (1999) A universal marker for transgenic insects. *Nature* **402:** 370-371

Bhandawat V, Olsen SR, Gouwens NW, Schlief ML & Wilson RI (2007) Sensory processing in the *Drosophila* antennal lobe increases reliability and separability of ensemble odor representations. *Nature Neuroscience* **10:** 1474-1482

Brand AH & Perrimon N (1993) Targeted gene expression as a means of altering cell fates and generating dominant phenotypes. *Development Cambridge England* **118:** 401-415

Broadie KS & Bate M (1993) Development of the embryonic neuromuscular synapse of *Drosophila melanogaster*. *Journal of Neuroscience* **13:** 144-166

Castillo PE, Schoch S, Schmitz F, Südhof TC & Malenka RC (2002) RIM1alpha is required for presynaptic long-term potentiation. *Nature* **415:** 327-330

Chou YH, Spletter ML, Yaksi E, Leong JCS, Wilson RI & Luo L (2010) Diversity and wiring variability of olfactory local interneurons in the *Drosophila* antennal lobe. *Nature neuroscience* **13:** 439-449

Christiansen F, Zube C, Andlauer TFM, Wichmann C, Fouquet W, Owald D, Mertel S, Leiss F, Tavosanis G, Luna AJF, Fiala A & Sigrist SJ (2011) Presynapses in Kenyon cell dendrites in the mushroom body calyx of *Drosophila*. *Journal of Neuroscience* **31:** 9696-9707

Connolly JB, Roberts IJ, Armstrong JD, Kaiser K, Forte M, Tully T & O'Kane CJ (1996) Associative learning disrupted by impaired Gs signaling in *Drosophila* mushroom bodies. *Science* **274:** 2104-2107

Copeland NG, Jenkins N a & Court DL (2001) Recombineering: a powerful new tool for mouse functional genomics. *Nature reviews. Genetics* **2:** 769-779

Couto A, Alenius M & Dickson BJ (2005) Molecular, anatomical, and functional organization of the *Drosophila* olfactory system. *Current Biology* **15:** 1535-1547

Crittenden JR, Skoulakis EMC, Han K-an, Kalderon D & Davis RL (1998) Markers tripartite mushroom body architecture revealed by antigenic markers. *Most* **5:** 38-51

Dai Y, Taru H, Deken SL, Grill B, Ackley B, Nonet ML & Jin Y (2006) SYD-2 Liprin-alpha organizes presynaptic active zone formation through ELKS. *Nature Neuroscience* **9:** 1479-1487

Davis GW (2006) Homeostatic control of neural activity: from phenomenology to molecular design. *Annual Review of Neuroscience* **29:** 307-323

Deguchi-Tawarada M, Inoue E, Takao-Rikitsu E, Inoue M, Ohtsuka T & Takai Y (2004) CAST2: identification and characterization of a protein structurally related to the presynaptic cytomatrix protein CAST. *Genes to cells devoted to molecular cellular mechanisms* **9:** 15-23

Deng L, Kaeser PS, Xu W & Südhof TC (2011) RIM proteins activate vesicle priming by reversing autoinhibitory homodimerization of Munc13. *Neuron* **69:** 317-331

DiAntonio A (2006) Glutamate receptors at the *Drosophila* neuromuscular junction. *International Review of Neurobiology* **75:** 165-179

Dickman DK & Davis GW (2009) The schizophrenia susceptibility gene dysbindin controls synaptic homeostasis. *Science* **326:** 1127-1130

Dietzl G, Chen D, Schnorrer F, Su K-C, Barinova Y, Fellner M, Gasser B, Kinsey K, Oppel S, Scheiblauer S, Couto A, Marra V, Keleman K & Dickson BJ (2007) A genome-wide transgenic RNAi library for conditional gene inactivation in *Drosophila*. *Nature* **448:** 151-156

Dolphin AC (2009) Calcium channel diversity: multiple roles of calcium channel subunits. *Current Opinion in Neurobiology* **19:** 237-244

Duffy JB (2002) GAL4 system in *Drosophila*: a fly geneticist's Swiss army knife. *Genesis New York NY 2000* **34:** 1-15

Engels WR (1983) The *P* family of transposable elements in *Drosophila*. *Annual Review of Genetics* **17:** 315-344

Fenster SD, Chung WJ, Zhai R, Cases-Langhoff C, Voss B, Garner AM, Kaempf U, Kindler S, Gundelfinger ED & Garner CC (2000) Piccolo, a presynaptic zinc finger protein structurally related to bassoon. *Neuron* **25:** 203-214

Fernández-Chacón R & Südhof TC (1999) Genetics of synaptic vesicle function: toward the complete functional anatomy of an organelle. *Annual Review of Physiology* **61:** 753-776

Fiala A (2007) Olfaction and olfactory learning in *Drosophila*: recent progress. *Current Opinion in Neurobiology* **17:** 720-726

Fouquet W, Owald D, Wichmann C, Mertel S, Depner H, Dyba M, Hallermann S, Kittel RJ, Eimer S & Sigrist SJ (2009) Maturation of active zone assembly by *Drosophila* Bruchpilot. *The Journal of Cell Biology* **186:** 129-145

Frank CA, Kennedy MJ, Goold CP, Marek KW & Davis GW (2006) Mechanisms underlying the rapid induction and sustained expression of synaptic homeostasis. *Neuron* **52:** 663-677

Franz G & Savakis C (1991) *Minos*, a new transposable element from *Drosophila hydei*, is a member of the Tc1-like family of transposons. *Nucleic Acids Research* **19:** 6646

Garner CC, Nash J & Huganir RL (2000) PDZ domains in synapse assembly and signalling. *Trends in Cell Biology* **10:** 274-280

Geppert M, Goda Y, Hammer RE, Li C, Rosahl TW, Stevens CF & Südhof TC (1994) Synaptotagmin I: a major Ca^{2+} sensor for transmitter release at a central synapse. *Cell* **79:** 717-727

Geppert M, Goda Y, Stevens CF & Südhof TC (1997) The small GTP-binding protein Rab3A regulates a late step in synaptic vesicle fusion. *Nature* **387:** 810-814

Giagtzoglou N, Mahoney T, Yao C-K & Bellen HJ (2009) Rab3 GTPase lands Bruchpilot. *Neuron* **64:** 595-597

Gloor GB & Engels WR (1992) Single-fly DNA preps for PCR. *Drosoph Inf Serv* **71:** 148-149

Gorczyca M & Budnik V (2006) Appendix: Anatomy of the larval body wall muscles and NMJs in the third instar larval stage. *International Review of Neurobiology* **75:** 367-373

Gouwens NW & Wilson RI (2009) Signal propagation in *Drosophila* central neurons. *Journal of Neuroscience* **29:** 6239-6249

Graf ER, Daniels RW, Burgess RW, Schwarz TL & DiAntonio A (2009) Rab3 dynamically controls protein composition at active zones. *Neuron* **64:** 663-677

Graf ER, Valakh V, Wright CM, Wu CL & DiAntonio A. RIM promotes Ca^{2+} accumulation at active zones of the *Drosophila* neuromuscular junction. Co-submitted manuscript

Gray YH (2000) It takes two transposons to tango: transposable-element-mediated chromosomal rearrangements. *Trends in Genetics* **16:** 461-468

Groth AC, Fish M, Nusse R & Calos MP (2004) Construction of transgenic *Drosophila* by using the site-specific integrase from phage phiC31. *Genetics* **166:** 1775-1782

Gundelfinger ED, Kessels MM & Qualmann B (2003) Temporal and spatial coordination of exocytosis and endocytosis. *Nature Reviews Molecular Cell Biology* **4:** 127-139

Häcker U, Nystedt S, Barmchi MP, Horn C & Wimmer EA (2003) *piggyBac*-based insertional mutagenesis in the presence of stably integrated *P* elements in *Drosophila*. *Proceedings of the National Academy of Sciences of the United States of America* **100:** 7720-7725

Hallermann S, Kittel RJ, Wichmann C, Weyhersmüller A, Fouquet W, Mertel S, Owald D, Eimer S, Depner H, Schwärzel M, Sigrist SJ & Heckmann M (2010) Naked dense bodies provoke depression. *Journal of Neuroscience* **30:** 14340-14345

Han Y, Kaeser PS, Südhof TC & Schneggenburger R (2011) RIM determines Ca^{2}+ channel density and vesicle docking at the presynaptic active zone. *Neuron* **69:** 304-316

Handler AM & Harrell RA (1999) Germline transformation of *Drosophila melanogaster* with the *piggyBac* transposon vector. *Insect Molecular Biology* **8:** 449-457

Hansson BS, Knaden M, Sachse S, Stensmyr MC & Wicher D (2010) Towards plant-odor-related olfactory neuroethology in *Drosophila*. *Chemoecology* **20:** 51-61

Heisenberg M (2003) Mushroom body memoir: from maps to models. *Nature Reviews Neuroscience* **4:** 266-275

Hell SW (2007) Far-Field Optical Nanoscopy. *Science* **316:** 1153-1158

Hibino H, Pironkova R, Onwumere O, Vologodskaia M, Hudspeth a J & Lesage F (2002) RIM binding proteins (RBPs) couple Rab3-interacting molecules (RIMs) to voltage-gated $Ca(^{2+})$ channels. *Neuron* **34:** 411-423

Hormuzdi SG, Filippov MA, Mitropoulou G, Monyer H & Bruzzone R (2004) Electrical synapses: a dynamic signaling system that shapes the activity of neuronal networks. *Biochimica et Biophysica Acta* **1662:** 113-137

Huang J, Zhang W, Qiao W, Hu A & Wang Z (2010) Functional connectivity and selective odor responses of excitatory local interneurons in *Drosophila* antennal lobe. *Neuron* **67:** 1021-1033

Ito K, Suzuki K, Estes P, Ramaswami M, Yamamoto D & Strausfeld NJ (1998) The organization of extrinsic neurons and their implications in the functional roles of the mushroom bodies in *Drosophila melanogaster* Meigen. *Learning & Memory* **5:** 52-77

Jahn R (2004) Principles of Exocytosis and Membrane Fusion. *Annals Of The New York Academy Of Sciences* **1014:** 170-178

Jan LY & Jan YN (1976) Properties of the larval neuromuscular junction in *Drosophila melanogaster*. *The Journal of Physiology* **262:** 189-214

Jin Y & Garner CC (2008) Molecular mechanisms of presynaptic differentiation. *Annual Review of Cell and Developmental Biology* **24:** 237-262

Kaeser PS, Deng L, Wang Y, Dulubova I, Liu X, Rizo J & Südhof TC (2011) RIM proteins tether Ca^{2+} channels to presynaptic active zones via a direct PDZ-domain interaction. *Cell* **144:** 282-295

Kaufmann N, DeProto J, Ranjan R, Wan H & Van Vactor D (2002) *Drosophila* liprin-alpha and the receptor phosphatase Dlar control synapse morphogenesis. *Neuron* **34:** 27-38

Kawasaki F, Felling R & Ordway RW (2000) A temperature-sensitive paralytic mutant defines a primary synaptic calcium channel in *Drosophila*. *Journal of Neuroscience* **20:** 4885-4889

Kawasaki F, Zou B, Xu X & Ordway RW (2004) Active zone localization of presynaptic calcium channels encoded by the cacophony locus of *Drosophila*. *Journal of Neuroscience* **24:** 282-285

Kazama H & Wilson RI (2008) Homeostatic matching and nonlinear amplification at identified central synapses. *Neuron* **58:** 401-413

Kazama H & Wilson RI (2009) Origins of correlated activity in an olfactory circuit. *Nature neuroscience* **12:** 1136-1144

Keene AC & Waddell S (2007) *Drosophila* olfactory memory: single genes to complex neural circuits. *Nature Reviews Neuroscience* **8:** 341-354

Keshishian H & Chiba A (1993) Neuromuscular development in *Drosophila*: insights from single neurons and single genes. *Trends in Neurosciences* **16:** 278-283

Keshishian H, Chiba A, Chang TN, Halfon MS, Harkins EW, Jarecki J, Wang L, Anderson M, Cash S & Halpern ME (1993) Cellular mechanisms governing synaptic development in *Drosophila melanogaster*. *Journal of Neurobiology* **24:** 757-787

Keshishian H, Broadie K, Chiba A & Bate M (1996) The *Drosophila* neuromuscular junction: a model system for studying synaptic development and function. *Annual Review of Neuroscience* **19:** 545-575

Khimich D, Nouvian R, Pujol R, Tom Dieck S, Egner A, Gundelfinger ED & Moser T (2005) Hair cell synaptic ribbons are essential for synchronous auditory signalling. *Nature* **434:** 889-894

Kim E & Sheng M (2004) PDZ domain proteins of synapses. *Nature Reviews Neuroscience* **5:** 771-781

Kittel RJ, Wichmann C, Rasse TM, Fouquet W, Schmidt M, Schmid A, Wagh DA, Pawlu C, Kellner RR, Willig KI, Hell SW, Buchner E, Heckmann M & Sigrist SJ (2006) Bruchpilot promotes active zone assembly, Ca^{2+} channel clustering, and vesicle release. *Science* **312:** 1051-1054

Klinakis AG, Zagoraiou L, Vassilatis DK & Savakis C (2000) Genome-wide insertional mutagenesis in human cells by the *Drosophila* mobile element *Minos*. *EMBO Reports* **1:** 416-421

Knapek S, Sigrist S & Tanimoto H (2011) Bruchpilot, a synaptic active zone protein for anesthesia-resistant memory. *Journal of Neuroscience* **31:** 3453-3458

Ko J, Na M, Kim S, Lee J-R & Kim E (2003) Interaction of the ERC family of RIM-binding proteins with the liprin-alpha family of multidomain proteins. *The Journal of Biological Chemistry* **278:** 42377-42385

Koenig JH & Ikeda K (1996) Synaptic vesicles have two distinct recycling pathways. *The Journal of Cell Biology* **135:** 797-808

Koh TW & Bellen HJ (2003) Synaptotagmin I, a Ca^{2+} sensor for neurotransmitter release. *Trends in Neurosciences* **26:** 413-422

Koh TW, Verstreken P & Bellen HJ (2004) Dap160/intersectin acts as a stabilizing scaffold required for synaptic development and vesicle endocytosis. *Neuron* **43:** 193-205

Koushika SP, Richmond JE, Hadwiger G, Weimer RM, Jorgensen EM & Nonet ML (2001) A post-docking role for active zone protein Rim. *Nature Neuroscience* **4:** 997-1005

Krashes MJ, Keene AC, Leung B, Armstrong JD & Waddell S (2007) Sequential use of mushroom body neuron subsets during *Drosophila* odor memory processing. *Neuron* **53**: 103-115

Kremer MC, Christiansen F, Leiss F, Paehler M, Knapek S, Andlauer TFM, Förstner F, Kloppenburg P, Sigrist SJ & Tavosanis G (2010) Structural long-term changes at mushroom body input synapses. *Current Biology* **20:** 1938-1944

Kuromi H & Kidokoro Y (1998) Two distinct pools of synaptic vesicles in single presynaptic boutons in a temperature-sensitive *Drosophila* mutant, shibire. *Neuron* **20:** 917-925

Larsson MC, Domingos AI, Jones WD, Chiappe ME, Amrein H & Vosshall LB (2004) Or83b encodes a broadly expressed odorant receptor essential for *Drosophila* olfaction. *Neuron* **43:** 703-714

Laski FA, Rio DC & Rubin GM (1986) Tissue specificity of *Drosophila P* element transposition is regulated at the level of mRNA splicing. *Cell* **44:** 7-19

Lee T, Lee A & Luo L (1999) Development of the *Drosophila* mushroom bodies: sequential generation of three distinct types of neurons from a neuroblast. *Development Cambridge England* **126:** 4065-4076

Leiss F, Koper E, Hein I, Fouquet W, Lindner J, Sigrist S & Tavosanis G (2009) Characterization of dendritic spines in the *Drosophila* central nervous system. *Developmental neurobiology* **69:** 221-234

Lin DM & Goodman CS (1994) Ectopic and increased expression of Fasciclin II alters motoneuron growth cone guidance. *Neuron* **13:** 507-523

Liu KS, Siebert M, Mertel S, Knoche E, Wegener S, Wichmann C, Matkovic T, Muhammad K, Depner H, Mettke C, Buckers J, Hell SW, Muller M, Davis GW, Schmitz D & Sigrist SJ (2011) RIM-binding protein, a central part of the active zone, is essential for neurotransmitter release. *Science* **334:** 1565-1569

Loukeris TG, Arcà B, Livadaras I, Dialektaki G & Savakis C (1995a) Introduction of the transposable element *Minos* into the germ line of *Drosophila melanogaster*. *Proceedings of the National Academy of Sciences of the United States of America* **92:** 9485-9489

Loukeris TG, Livadaras I, Arcà B, Zabalou S & Savakis C (1995b) Gene transfer into the medfly, Ceratitis capitata, with a *Drosophila hydei* transposable element. *Science* **270:** 2002-2005

Lu HC, Butts DA, Kaeser PS, She WC, Janz R & Crair MC (2006) Role of efficient neurotransmitter release in barrel map development. *Journal of Neuroscience* **26:** 2692-2703

Masse NY, Turner GC & Jefferis GSXE (2009) Olfactory information processing in *Drosophila*. *Current Biology* **19:** R700-R713

Masugi-Tokita M, Tarusawa E, Watanabe M, Molnár E, Fujimoto K & Shigemoto R (2007) Number and density of AMPA receptors in individual synapses in the rat cerebellum as revealed by SDS-digested freeze-fracture replica labeling. *Journal of Neuroscience* **27:** 2135-2144

McGee AW & Bredt DS (2003) Assembly and plasticity of the glutamatergic postsynaptic specialization. *Current Opinion in Neurobiology* **13:** 111-118

Metaxakis A, Oehler S, Klinakis A & Savakis C (2005) *Minos* as a Genetic and Genomic Tool in *Drosophila melanogaster*. *Genetics* **171:** 571-581

Mittelstaedt T & Schoch S (2007) Structure and evolution of RIM-BP genes: identification of a novel family member. *Gene* **403:** 70-79

Mittelstaedt T, Alvaréz-Baron E & Schoch S (2010) RIM proteins and their role in synapse function. *Biological Chemistry* **391:** 599-606

Müller CS, Haupt A, Bildl W, Schindler J, Knaus H-G, Meissner M, Rammner B, Striessnig J, Flockerzi V, Fakler B & Schulte U (2010) Quantitative proteomics of the Cav2 channel nano-environments in the mammalian brain. *Proceedings of the National Academy of Sciences of the United States of America* **107:** 14950-14957

Müller M, Pym ECG, Tong A & Davis GW (2011) Rab3-GAP controls the progression of synaptic homeostasis at a late stage of vesicle release. *Neuron* **69:** 749-762

Müller M, Liu KS, Sigrist SJ & Davis GW. RIM-dependent modulation of the readily releasable pool controls homeostatic plasticity independent of presynaptic calcium influx. *The Journal of Neuroscience* In review

Neher E (1998) Vesicle pools and Ca^{2+} microdomains: new tools for understanding their roles in neurotransmitter release. *Neuron* **20:** 389-399

Neher E & Sakaba T (2008) Multiple roles of calcium ions in the regulation of neurotransmitter release. *Neuron* **59:** 861-872

Neuhaus EM, Gisselmann G, Zhang W, Dooley R, Störtkuhl K & Hatt H (2005) Odorant receptor heterodimerization in the olfactory system of *Drosophila melanogaster*. *Nature Neuroscience* **8:** 15-17

O'Kane CJ & Gehring WJ (1987) Detection in situ of genomic regulatory elements in *Drosophila*. *Proceedings of the National Academy of Sciences of the United States of America* **84:** 9123-9127

Ohtsuka T, Takao-Rikitsu E, Inoue E, Inoue M, Takeuchi M, Matsubara K, Deguchi-Tawarada M, Satoh K, Morimoto K, Nakanishi H & Takai Y (2002) Cast: a novel protein of the cytomatrix at the active zone of synapses that forms a ternary complex with RIM1 and munc13-1. *The Journal of Cell Biology* **158:** 577-590

Okada R, Awasaki T & Ito K (2009) Gamma-aminobutyric acid (GABA)-mediated neural connections in the *Drosophila* antennal lobe. *Journal of Comparative Neurology* **514:** 74-91

Olsen O, Moore KA, Fukata M, Kazuta T, Trinidad JC, Kauer FW, Streuli M, Misawa H, Burlingame AL, Nicoll RA & Bredt DS (2005) Neurotransmitter release regulated by a MALS-liprin-alpha presynaptic complex. *The Journal of Cell Biology* **170:** 1127-1134

Olsen SR, Bhandawat V & Wilson RI (2007) Excitatory interactions between olfactory processing channels in the *Drosophila* antennal lobe. *Neuron* **54:** 89-103

Olsen SR & Wilson RI (2008a) Lateral presynaptic inhibition mediates gain control in an olfactory circuit. *Nature* **452:** 956-960

Olsen SR & Wilson RI (2008b) Cracking neural circuits in a tiny brain: new approaches for understanding the neural circuitry of *Drosophila*. *Trends in Neurosciences* **31:** 512-520

Owald D, Fouquet W, Schmidt M, Wichmann C, Mertel S, Depner H, Christiansen F, Zube C, Quentin C, Körner J, Urlaub H, Mechtler K & Sigrist SJ (2010) A Syd-1 homologue regulates pre- and postsynaptic maturation in *Drosophila*. *The Journal of cell biology* **188:** 565-579

Owald D & Sigrist SJ (2009) Assembling the presynaptic active zone. *Current Opinion in Neurobiology* **19:** 311-318

Parks AL, Cook KR, Belvin M, Dompe N a, Fawcett R, Huppert K, Tan LR, Winter CG, Bogart KP, Deal JE, Deal-Herr ME, Grant D, Marcinko M, Miyazaki WY, Robertson S, Shaw KJ, Tabios M, Vysotskaia V, Zhao L, Andrade RS, *et al* (2004) Systematic generation of high-resolution deletion coverage of the *Drosophila melanogaster* genome. *Nature genetics* **36:** 288-292

Pascual A & Préat T (2001) Localization of long-term memory within the *Drosophila* mushroom body. *Science* **294:** 1115-1117

Patel MR, Lehrman EK, Poon VY, Crump JG, Zhen M, Bargmann CI & Shen K (2006) Hierarchical assembly of presynaptic components in defined *C. elegans* synapses. *Nature Neuroscience* **9:** 1488-1498

Petersen SA, Fetter RD, Noordermeer JN, Goodman CS & DiAntonio A (1997) Genetic analysis of glutamate receptors in *Drosophila* reveals a retrograde signal regulating presynaptic transmitter release. *Neuron* **19:** 1237-1248

Phillips GR, Huang JK, Wang Y, Tanaka H, Shapiro L, Zhang W, Shan WS, Arndt K, Frank M, Gordon RE, Gawinowicz MA, Zhao Y & Colman DR (2001) The presynaptic particle web: ultrastructure, composition, dissolution, and reconstitution. *Neuron* **32:** 63-77

Prokop A (1999) Integrating bits and pieces: synapse structure and formation in *Drosophila* embryos. *Cell and Tissue Research* **297:** 169-186

Prokop A & Meinertzhagen IA (2006) Development and structure of synaptic contacts in *Drosophila*. *Seminars in cell developmental biology* **17:** 20-30

Qin G, Schwarz T, Kittel RJ, Schmid A, Rasse TM, Kappei D, Ponimaskin E, Heckmann M & Sigrist SJ (2005) Four different subunits are essential for expressing the synaptic glutamate receptor at neuromuscular junctions of *Drosophila*. *Journal of Neuroscience* **25:** 3209-3218

Rasse TM, Fouquet W, Schmid A, Kittel RJ, Mertel S, Sigrist CB, Schmidt M, Guzman A, Merino C, Qin G, Quentin C, Madeo FF, Heckmann M & Sigrist SJ (2005) Glutamate receptor dynamics organizing synapse formation in vivo. *Nature Neuroscience* **8:** 898-905

Renner M, Specht CG & Triller A (2008) Molecular dynamics of postsynaptic receptors and scaffold proteins. *Current Opinion in Neurobiology* **18:** 532-540

Rizzoli SO & Betz WJ (2005) Synaptic vesicle pools. *Nature Reviews Neuroscience* **6:** 57-69

Root CM, Semmelhack JL, Wong AM, Flores J & Wang JW (2007) Propagation of olfactory information in *Drosophila*. *Proceedings of the National Academy of Sciences of the United States of America* **104:** 11826-11831

Rosenmund C (2003) Molecular mechanisms of active zone function. *Current Opinion in Neurobiology* **13:** 509-519

Rostaing P, Weimer RM, Jorgensen EM, Triller A & Bessereau J-L (2004) Preservation of immunoreactivity and fine structure of adult *C. elegans* tissues using high-pressure freezing. *The journal of histochemistry and cytochemistry official journal of the Histochemistry Society* **52:** 1-12

Ruiz-Cañada C & Budnik V (2006) Synaptic cytoskeleton at the neuromuscular junction. *International Review of Neurobiology* **75:** 217-236

Salinas PC (2005) Retrograde signalling at the synapse: a role for Wnt proteins. *Biochemical Society Transactions* **33:** 1295-1298

Schmid A, Qin G, Wichmann C, Kittel RJ, Mertel S, Fouquet W, Schmidt M, Heckmann M & Sigrist SJ (2006) Non-NMDA-type glutamate receptors are essential for maturation but not for initial assembly of synapses at *Drosophila* neuromuscular junctions. *Journal of Neuroscience* **26:** 11267-11277

Schmid A, Hallermann S, Kittel RJ, Khorramshahi O, Frölich AMJ, Quentin C, Rasse TM, Mertel S, Heckmann M & Sigrist SJ (2008) Activity-dependent site-specific changes of glutamate receptor composition in vivo. *Nature Neuroscience* **11:** 659-666

Schneggenburger R, Meyer AC & Neher E (1999) Released fraction and total size of a pool of immediately available transmitter quanta at a calyx synapse. *Neuron* **23:** 399-409

Schoch S, Castillo PE, Jo T, Mukherjee K, Geppert M, Wang Y, Schmitz F, Malenka RC & Südhof TC (2002) RIM1alpha forms a protein scaffold for regulating neurotransmitter release at the active zone. *Nature* **415:** 321-326

Schoch S & Gundelfinger ED (2006) Molecular organization of the presynaptic active zone. *Cell and Tissue Research* **326:** 379-391

Schuster CM, Davis GW, Fetter RD & Goodman CS (1996) Genetic dissection of structural and functional components of synaptic plasticity. I. Fasciclin II controls synaptic stabilization and growth. *Neuron* **17:** 641-654

Serano TL, Cheung HK, Frank LH & Cohen RS (1994) *P* element transformation vectors for studying *Drosophila melanogaster* oogenesis and early embryogenesis. *Gene* **138:** 181-186

Seki Y, Rybak J, Wicher D, Sachse S & Hansson BS (2010) Physiological and morphological characterization of local interneurons in the *Drosophila* antennal lobe. *Journal of neurophysiology* **104:** 1007-1019

Shang Y, Claridge-Chang A, Sjulson L, Pypaert M & Miesenböck G (2007) Excitatory local circuits and their implications for olfactory processing in the fly antennal lobe. *Cell* **128:** 601-612

Sheng M & Hoogenraad CC (2007) The postsynaptic architecture of excitatory synapses: a more quantitative view. *Annual Review of Biochemistry* **76:** 823-847

Sigrist SJ, Thiel PR, Reiff DF, Lachance PE, Lasko P & Schuster CM (2000) Postsynaptic translation affects the efficacy and morphology of neuromuscular junctions. *Nature* **405:** 1062-1065

Sigrist SJ, Reiff DF, Thiel PR, Steinert JR & Schuster CM (2003) Experience-dependent strengthening of *Drosophila* neuromuscular junctions. *Journal of Neuroscience* **23:** 6546-6556

Siksou L, Rostaing P, Lechaire J-P, Boudier T, Ohtsuka T, Fejtová A, Kao H-T, Greengard P, Gundelfinger ED, Triller A & Marty S (2007) Three-dimensional architecture of presynaptic terminal cytomatrix. *Journal of Neuroscience* **27:** 6868-6877

Sone M, Suzuki E, Hoshino M, Hou D, Kuromi H, Fukata M, Kuroda S, Kaibuchi K, Nabeshima Y & Hama C (2000) Synaptic development is controlled in the periactive zones of *Drosophila* synapses. *Development Cambridge England* **127:** 4157-4168

Spradling AC, Stern DM, Kiss I, Roote J, Laverty T & Rubin GM (1995) Gene disruptions using *P* transposable elements: an integral component of the *Drosophila* genome project. *Proceedings of the National Academy of Sciences of the United States of America* **92:** 10824-10830

Stewart BA, Atwood HL, Renger JJ, Wang J & Wu CF (1994) Improved stability of *Drosophila* larval neuromuscular preparations in haemolymph-like physiological solutions. *Journal of comparative physiology A Sensory neural and behavioral physiology* **175:** 179-191

Stigloher C, Zhan H, Zhen M, Richmond J & Bessereau J-L (2011) The presynaptic dense projection of the *Caenorhabditis elegans* cholinergic neuromuscular junction localizes synaptic vesicles at the active zone through SYD-2/liprin and UNC-10/RIM-dependent interactions. *Journal of Neuroscience* **31:** 4388-4396

Stocker RF, Lienhard MC, Borst A & Fischbach KF (1990) Neuronal architecture of the antennal lobe in *Drosophila melanogaster*. *Cell and Tissue Research* **262:** 9-34

Stocker RF (1994) The organization of the chemosensory system in *Drosophila melanogaster*: a review. *Cell and Tissue Research* **275:** 3-26

Strausfeld NJ & Hildebrand JG (1999) Olfactory systems: common design, uncommon origins? *Current Opinion in Neurobiology* **9:** 634-639

Südhof TC (2004) The synaptic vesicle cycle. *Annual Review of Neuroscience* **27:** 509-547

Südhof TC & Rizo J (2011) Synaptic vesicle exocytosis. *Cold Spring Harbor Perspectives in Biology* **98:** 11474-11478

Tanaka NK, Tanimoto H & Ito K (2008) Neuronal assemblies of the *Drosophila* mushroom body. *Journal of Comparative Neurology* **508:** 711-755

Tanaka NK, Ito K & Stopfer M (2009) Odor-evoked neural oscillations in *Drosophila* are mediated by widely branching interneurons. *The Journal of neuroscience* **29:** 8595-8603

Thibault ST, Singer MA, Miyazaki WY, Milash B, Dompe NA, Singh CM, Buchholz R, Demsky M, Fawcett R, Francis-Lang HL, Ryner L, Cheung LM, Chong A, Erickson C, Fisher WW, Greer K, Hartouni SR, Howie E, Jakkula L, Joo D, *et al* (2004) A complementary transposon tool kit for *Drosophila melanogaster* using P and piggyBac. *Nature Genetics* **36:** 283-287

Thomas U, Kim E, Kuhlendahl S, Koh YH, Gundelfinger ED, Sheng M, Garner CC & Budnik V (1997) Synaptic clustering of the cell adhesion molecule fasciclin II by discs-large and its role in the regulation of presynaptic structure. *Neuron* **19:** 787-799

Thummel CS & Pirrotta V (1992) New pCaSpeR P element vectors. *Drosophila Information Newsletter* **71:** 150

Tom Dieck S, Sanmartí-Vila L, Langnaese K, Richter K, Kindler S, Soyke A, Wex H, Smalla KH, Kämpf U, Fränzer JT, Stumm M, Garner CC & Gundelfinger ED (1998) Bassoon, a novel zinc-finger CAG/glutamine-repeat protein selectively localized at the active zone of presynaptic nerve terminals. *The Journal of Cell Biology* **142:** 499-509

Tom Dieck S, Altrock WD, Kessels MM, Qualmann B, Regus H, Brauner D, Fejtová A, Bracko O, Gundelfinger ED & Brandstätter JH (2005) Molecular dissection of the photoreceptor ribbon synapse. *The Journal of Cell Biology* **168:** 825-836

Venken KJT, He Y, Hoskins RA & Bellen HJ (2006) P[acman]: a BAC transgenic platform for targeted insertion of large DNA fragments in *D. melanogaster*. *Science* **314:** 1747-1751

Venken KJT, Carlson JW, Schulze KL, Pan H, He Y, Spokony R, Wan KH, Koriabine M, de Jong PJ, White KP, Bellen HJ & Hoskins RA (2009) Versatile P[acman] BAC libraries for transgenesis studies in *Drosophila melanogaster*. *Nature methods* **6:** 431-434

Verstreken P, Kjaerulff O, Lloyd TE, Atkinson R, Zhou Y, Meinertzhagen IA & Bellen HJ (2002) Endophilin mutations block clathrin-mediated endocytosis but not neurotransmitter release. *Cell* **109:** 101-112

Von Gersdorff H (2001) Synaptic ribbons: versatile signal transducers. *Neuron* **29:** 7-10

Vosshall LB, Amrein H, Morozov PS, Rzhetsky A & Axel R (1999) A spatial map of olfactory receptor expression in the *Drosophila* antenna. *Cell* **96:** 725-736

Vosshall LB, Wong AM & Axel R (2000) An olfactory sensory map in the fly brain. *Cell* **102:** 147-159

Vosshall LB & Stocker RF (2007) Molecular architecture of smell and taste in *Drosophila*. *Annual Review of Neuroscience* **30:** 505-533

Wadel K, Neher E & Sakaba T (2007) The coupling between synaptic vesicles and Ca^{2+} channels determines fast neurotransmitter release. *Neuron* **53:** 563-575

Wagh D a, Rasse TM, Asan E, Hofbauer A, Schwenkert I, Dürrbeck H, Buchner S, Dabauvalle M-C, Schmidt M, Qin G, Wichmann C, Kittel R, Sigrist SJ & Buchner E (2006) Bruchpilot, a protein with homology to ELKS/CAST, is required for structural integrity and function of synaptic active zones in *Drosophila*. *Neuron* **49:** 833-844

Wang Y, Okamoto M, Schmitz F, Hofmann K & Südhof TC (1997) Rim is a putative Rab3 effector in regulating synaptic-vesicle fusion. *Nature* **388:** 593-598

Wang Y, Sugita S & Südhof TC (2000) The RIM/NIM family of neuronal C2 domain proteins. Interactions with Rab3 and a new class of Src homology 3 domain proteins. *The Journal of Biological Chemistry* **275:** 20033-20044

Wang Y, Liu X, Biederer T & Südhof TC (2002) A family of RIM-binding proteins regulated by alternative splicing: Implications for the genesis of synaptic active zones. *Proceedings of the National Academy of Sciences of the United States of America* **99:** 14464-14469

Wang Y & Südhof TC (2003) Genomic definition of RIM proteins: evolutionary amplification of a family of synaptic regulatory proteins. *Genomics* **81:** 126-137

Weyhersmüller A, Hallermann S, Wagner N & Eilers J (2011) Rapid active zone remodeling during synaptic plasticity. *Journal of Neuroscience* **31:** 6041-6052

Wichmann C & Sigrist SJ (2010) The active zone T-bar-a plasticity module? *Journal of Neurogenetics* **24:** 133-145

Wilson RI, Turner GC & Laurent G (2004) Transformation of olfactory representations in the *Drosophila* antennal lobe. *Science* **303:** 366-370

Woehler A & Ponimaskin EG (2009) G protein-mediated signaling: same receptor, multiple effectors. *Current molecular pharmacology* **2:** 237-248

Wu JS & Luo L (2006) A protocol for dissecting *Drosophila melanogaster* brains for live imaging or immunostaining. *Nature Protocols* **1:** 2110-2115

Wucherpfennig T, Wilsch-Bräuninger M & González-Gaitán M (2003) Role of *Drosophila* Rab5 during endosomal trafficking at the synapse and evoked neurotransmitter release. *The Journal of Cell Biology* **161:** 609-624

Yaksi E & Wilson RI (2010) Electrical coupling between olfactory glomeruli. *Neuron* **67:** 1034-1047

Yasuyama K, Meinertzhagen IA & Schürmann FW (2002) Synaptic organization of the mushroom body calyx in *Drosophila melanogaster*. *Journal of Comparative Neurology* **445:** 211-226

Yu D, Akalal D-BG & Davis RL (2006) *Drosophila* alpha/beta mushroom body neurons form a branch-specific, long-term cellular memory trace after spaced olfactory conditioning. *Neuron* **52:** 845-855

Zagoraiou L, Drabek D, Alexaki S, Guy JA, Klinakis AG, Langeveld A, Skavdis G, Mamalaki C, Grosveld F & Savakis C (2001) In vivo transposition of *Minos*, a *Drosophila* mobile element, in mammalian tissues. *Proceedings of the National Academy of Sciences of the United States of America* **98:** 11474-11478

Zhai RG & Bellen HJ (2004) The architecture of the active zone in the presynaptic nerve terminal. *Physiology Bethesda Md* **19:** 262-270

Zhen M & Jin Y (2004) Presynaptic terminal differentiation: transport and assembly. *Current Opinion in Neurobiology* **14:** 280-287

Ziv NE & Garner CC (2004) Cellular and molecular mechanisms of presynaptic assembly. *Nature Reviews Neuroscience* **5:** 385-399

Zucker RS & Regehr WG (2002) Short-term synaptic plasticity. *Annual Review of Physiology* **64:** 355-405

7. Appendix

7.1 Table of Figures

7.2 Abbreviations

aa	amino acid
ABP	AMPA receptor binding protein
ACh	acetylcholine
AL	antennal lobe
AMPA	alpha-amino-3-hydroxy-5-methyl-4-isoxazole-propionic-acid
Ap^R	ampicillin resistant
attB	bacterial attachment
attL	left attachment
attP	phage attachment
attR	right attachment
AZ	active zone
BAC	bacterial artificial chromosome
bp	base pair
BRP	Bruchpilot
C2 domain	Ca^{2+}-dependent phospholipid binding domain
Ca^{2+}	calcium
Cac	Cacophony
C. elegans	*Caenorhabditis elegans*
cAMP	cyclic adenosine monophosphate
CAST	cytomatrix at the active zone-associated structural protein
CAZ	cytomatrix at the active zone
CDS	coding DNA sequence
ChA	choline acetyltransferase
Cm^R	chloramphenicol resistant
CNS	central nervous system
$D\alpha7^{GFP}$	GFP-labeled acetylcholine receptor subunits
Dlg	*Drosophila* PSD-95/SAP90 orthologue Discs-large
Drosophila/ D. melanogaster	*Drosophila melanogaster*

DSyd	*Drosophila* synapse-defective
E. coli	*Escherichia coli*
eEJCs	evoked excitatory junctional current
ELKS	glutamine, leucine, lysine, and serine-rich protein
eLN	excitatory LN
EM	electron microscopy
EMS	ethane methyl sulfonate
ERC	ELKS/Rab6-interacting protein/CAST
exo/endo-cycle	exocytosis/ endocytosis cycle
FasII	Fasciclin II
FNIII	fibronectin type III
GABA	gamma-aminobutyric acid
GAD-1	glutamic acid decarboxylase 1
GluRs	glutamate receptors
GFP	green fluorescent protein
GRIP	glutamate receptor interacting protein
hs	heat shock driven
iLN	inhibitory LN
kb	kilo bases
KC	Kenyon cell
KCACs	KC-derived AZs in the calyx
kDa	kilo Dalton
LA	left homology arm
LH	lateral horn
LN	local interneuron
MAGUKs	guanylate kinases
MB	mushroom body
MCS	multiple cloning site
mEJC	miniature excitatory junctional currents
Munc13	mammalian homologue of *C. elegans* Unc13 protein
Munc18	mammalian homologue of *C. elegans* Unc18 protein
NGS	normal goat serum
NMDA	N-methyl-D-aspartic acid
NMJ	neuromuscular junction
ori	origin of replication
oriV	copy-inducible origin of replication
oriS	low-copy origin of replication
OR	odorant receptor
ORN	odorant receptor neuron
PAK	p21-activated kinase
PBS (PBT)	phosphate buffered saline (+ triton)
PCR	polymerase chain reaction
PDZ	PSD protein 95 kDa/Discs Large/zona occludens-1
PFA	paraformaldehyde
PICK1	protein interacting with C kinase
PN	projection neuron
PSD	postsynaptic density
PSD95	postsynaptic density protein 95
RA	right homology arm

RIM	Rab-3 interacting molecule
RIM-BP	RIM binding protein
RRP	readily releasable pool
RNAi	ribonucleic acid (RNA) interference
SAP47	synapse associated protein 47
SD	standard deviation
SEM	standard error of mean
SH3	SRC Homology 3
SNAP	soluble N-ethylmaleimidesensitive factor attachment protein
SNARE	SNAP receptor
SSR	subsynaptic reticulum
STED	stimulated emission depletion microscopy
SV(s)	synaptic vesicle(s)
Syb	synaptobrevin
Syt	synaptotagmin
TEM	transmission electron microscopy
w	*white*
UAS	upstream activating sequence
Unc13	Uncoordinated protein-13
UTR	untranslated region

7.3 Publications

In preparation	Andlauer TFM*, **Liu KS***, Steckhan N, Zube C, Sigrist SJ. A RATIOnal approach to synapse diversity of the *Drosophila* brain. *equal contributions
Accepted	Müller M, **Liu KS**, Sigrist SJ, Davis GW. RIM Controls homeostatic plasticity through modulation of the readily-releasable vesicle pool. *Journal of Neuroscience*.
2011	**Liu KS***, Siebert M*, Mertel S*, Knoche E*, Wegener S*, Wichmann C, Matkovic T, Muhammad K, Depner H, Mettke C, Bückers J, Hell SW, Müller M, Davis GW, Schmitz D, Sigrist SJ. (2011) RIM-binding protein, a central part of the active zone, is essential for neurotransmitter release. *Science*. 334(6062):1565-1569. *equal contributions